Computer modelling of pure and doped stoichiometric and congruent lithium niobate

Ellis Edwyn Hedges

M.Phil

October 2018

Keele University

Abbreviations

GULP = General Utility Lattice Programme

BFGS = The Broyden-Fletcher-Goldfard-Shanno Algorithm

RFO = The Rational Function Optimiser

cLN = Congruent Lithium Niobate

sLN = Stochiometric Lithium Niobate

EXAFS = Extended X-ray Absorption Fine Structure

T_c = Curie temperature

MD = Molecular Dynamics Simulations

VASP = Vienna Ab initio Simulation Package

PAW = Projected-augmented Wave

MP = Monkhorst-pack

Mt-Ltn = Mott-Littleton Method

Contents

Abstract……4
Chapter 1 - Introduction……5

Chapter 2 – Computer Modelling……7

- 2.1 Background……7
- 2.2 GULP……8
- 2.3 Interatomic Potentials……9
    - 2.3.1 Long Range Potentials……9
    - 2.3.2 Short Range Potentials……10
- 2.4 Lattice Energy Minimisation……11
- 2.5 Mott-Littleton Method……12
- 2.6 Supercell Method……14
- 2.7 Solution Energy Calculations……14
- 2.8 Python Scripts……17
- 2.9 Summary……18

Chapter 3 – $LiNbO_3$……19
- 3.1 Background……19
- 3.2 Mott-Littleton Calculations……22
- 3.3 Stoichiometric Lithium Niobate……27
- 3.4 Congruent Lithium Niobate……34
- 3.5 sLN vs cLN……42
- 3.6 Summary……53

Chapter 4 – $LiNbO_3$: Paraelectric Phase……54
- 4.1 Background……54
- 4.2 Results……55

Chapter 5 - Conclusions……63

References……64

Abstract

This investigation has modelled lithium niobate in its congruent form, stoichiometric form and paraelectric phase to determine whether the preference of doping schemes changes, specifically when the concentration of a dopant is varied. Mott-Littleton calculations and the supercell method were used to model defect structures of lithium niobate and assess the viability of four doping schemes, with a particular emphasis on the dopant Zn^{2+}, however other dopants were used.

The Mott-Littleton calculations involved the doping of multiple divalent and trivalent dopants. The results obtained showed scheme 2 to be the scheme with the lowest solution energy across all the dopants. The supercell method was carried out using a stoichiometric supercell of 48 Li and 48 Nb sites, with another larger stoichiometric supercell being used that contained 162 Li and 162 Nb sites for comparison with the same sized congruent supercell. The congruent supercell, however, contained a Li/Nb ratio of 0.963, in order to make the cell congruent. The dopants used in both supercells were Zn^{2+}, Ce^{3+}, In^{3+} and Eu^{3+}. The supercells showed the effect of dopant concentration on the scheme preference.

The paraelectric phase was only modelled using the Mott-Littleton method. The same dopants used in the stoichiometric Mott-Littleton modelling were employed. The results from the paraelectric phase were then compared to the stoichiometric form's results, which showed no change in the preference of the doping schemes, with scheme 2 having the lowest solution energy across all divalent and trivalent dopants.

Overall, the results showed that the doping scheme preferred is Scheme 2, both for divalent and trivalent dopants, which involved doping at the Li site and Nb site, and that the effect of increasing the concentration of the dopant had little effect.

Chapter 1 - Introduction

This investigation studies different models of Lithium Niobate to ascertain the preferred doping site, the Li site, the Nb site or a mixture of the two. The results are also compared, mainly, to the computational studies of Jackson et al. [1–4], whose doping schemes are used in this study, and the experimental studies of Bridges et al. [5–7] The aims and objectives are:

- To model the Mott-Littleton and supercell structures of congruent, stoichiometric and paraelectric phases of $LiNbO_3$ with different dopants, using four different possible dopant schemes.
- Investigate the effect of increasing dopant concentration on scheme preference using the supercell model.
- Compare the results to other computational and experimental studies of $LiNbO_3$.

This thesis will contain five chapters, as listed in the title page, however here is a summary of the contents of each section. Chapter 2 will describe the different computational methods used, the Mott-Littleton method and the supercell method, in this study and their origin. The background to computer modelling will be addressed in section 2.1, explaining the reasoning behind computer modelling and also its uses. 2.2 will introduce the General Utility Lattice Program (GULP), the chosen program the material in this paper is modelled on. 2.3 and 2.4 will explain interatomic potentials and lattice energy minimisation, respectively, and explain their use in modelling materials. 2.5 will explain Mott-Littleton method and 2.6 will explain the supercell method. Section 2.7 discuses the solution energy calculations and 2.8 the construction of the python scripts involved in running some of the files. 2.9 will finally summarise the chapter.

Chapter 3 will involve the data obtained from the modelling of $LiNbO_3$ in its congruent and stoichiometric forms. It is split into five sections, each covering a different aspect of the data obtained. 3.1 is a background section that explains the uses of $LiNbO_3$ and the various studies of dopants employed. 3.2 lists the data obtained from the Mott-Littleton approach, linked to other studies involving $LiNbO_3$, whilst 3.3 and 3.4 deal with the modelling of the stoichiometric and congruent phase of the material, respectively. 3.5 compares the data obtained from the congruent and stoichiometric phases and relates this to other studies.

Chapter 4 discusses the paraelectric phase, modelled using the Mott-Littleton method. The data gathered is then compared to the results from the previous Mott-Littleton calculation and also with data from Araujo et al. (2007)[3].

Chapter 5 will conclude the findings of this study and suggest ideas worthy of further investigation. Results obtained from $LiNbO_3$ are summarised and then compared with other studies.

Chapter 2 - Computer Modelling

2.1 Background

Computational chemistry methods have become a useful tool in research. It is said that there are three main problems for a "newcomer to the field", deciphering the code, technical problems and quality assessment [8]. "Deciphering the code" relates to the fact that you have to learn a new "language" when practising computational chemistry, as the methods use all sorts of acronyms and these must be learnt [8]. "Technical problems" can be both hardware and software related, as these both change over time, this can be the most difficult problem to accomplish as books can become out of date quickly due to the ever increasing capability of computers [8]. "Quality assessment" refers to the evaluation of the calculation and how accurate the final value is [8]. "Quality assessment" has become the "central theme" in computational chemistry, as computer programs have become easier to use and now often communicate to users through a graphical interface, meaning that it is no longer necessary to have a highly trained theoretician to run sophisticated programs [8]. This means that it has become quite easy to run a lot of calculations and get meaningless results, as the program does not tell you whether the chosen calculation or method is valid for the project you're investigating [8]. Therefore, experience is needed and a basic understanding of the theory is required to calibrate the results, especially if novel procedures are being undertaken [8].

A "lack of quality assessment" has probably played a part in the perception of computational chemistry being seen as an unreliable source of information, as different computational methods on the same problem all could give widely different results, due to this lack of quality assessment [8]. Therefore, the ability to interpret the data received from the method must still be interpreted by a practitioner rather than a computer to understand the behaviour of a large group of molecules [8]. A large portion of time in computational chemistry is spent on "many-body problems" [8]. A "many-body problem" involves two-particle system being solved accurately by mathematical methods, generating solutions in terms of analytical function [8]. Computational methods cannot solve a problem involving more than two particles completely, as systems involving more than one particle cannot be solved by analytical methods, approximations can be made and developed to any desired degree of accuracy [8].

Atomistic simulation became popular as computers became more widespread and as programs were developed and made available [9]. In the UK, a lot of the work was done by the Atomic Energy Authority at Harwell, with a number of computer codes being produced from this work, specifically HADES, MIDAS and PLUTO, which led to the development of other codes including METAPOCS and CASCADE, to be developed elsewhere [9]. Computer modelling has many applications including the prediction of the relative energetics of different polymorphs [10], determination of the mechanical properties of solids and the generation of possible atomic arrangements to assist in the solution of crystal structures from diffraction techniques [11,12]. The modelling of inorganic and organic materials has developed independently in the main, with organic materials making use of interatomic potential calculations to utilise the accepted connectivity of covalent systems in an attempt to advance the molecular mechanics approach, whereas inorganic material calculations, such as oxides and halides, have been founded on a fully ionic description with a shell-model management of ion polarisation [11]. One program that is suitable to use organic and inorganic systems alike is the General Utility Lattice Program (GULP).

2.2 GULP

The General Utility Lattice Program (GULP) was developed by Julian Gale [9] and the first publication reported in 1997 [11]. The main idea behind it was to combine many of the services required for solid state simulation, concentrating on "static lattice/lattice dynamical methods" into a single package and make it easy to use [9]. GULP can be used for the optimisation of structures and the calculation of their properties but also can be used to derive interatomic potentials [11]. One such demonstration of this is the creation of a new interatomic potential for the ferroelectric and paraelectric phases of $LiNbO_3$ by Jackson and Valerio (2005) [4]. In order to do this, GULP was designed to accept numerous structures within each input deck [11]. GULP was originally written in FORTRAN 77, but a FORTRAN 90 version is available, which "makes use of the dynamic energy features" [11] It has been used in a variety of different situations [13–17]. One study used GULP to simulate Cd_2GeO_4 and the formation of oxygen defects [17] with another studying a new reactive force field for calcium carbonate [14].

Gale (2007) [11] states that "the calculation of the energetics of a three-dimensional system theoretically involves the evaluation of interactions between all species, be they cores, shells or united atom units, within the unit cell and their periodic replicating to infinity", therefore, because this is not possible, assumptions must be made and a "finite cut-off" [11] imposed. The components of a lattice energy can be split into two classes: long and short-range potentials [11].

2.3 Interatomic Potentials

2.3.1 Long range Potentials

Long-range potentials are the “dominant term for many inorganic materials” [11] so it is therefore very important to calculate them accurately. In order to calculate the electrostatic energy, which depends on 1/r and is slowly convergent, the Ewald summation is the preferred tool of choice [18]. The expression for the Ewald summation is shown below:

$$E_{recip} = \left(\frac{1}{2}\right)\frac{4\pi}{V}\sum_{G}\frac{\left(-\frac{G^2}{4\eta}\right)}{G^2}\ x\sum_{i}\sum_{j} q_i q_j \exp\left(-iGr_{ij}\right)$$

$$E_{real} = \frac{1}{2}\sum_{i}\sum_{j}\frac{q_i q_j erfc\left(\eta^{1/2} r_{ij}\right)}{r_{ij}}$$

Example Equation 1 – Ewald summation [18].

V equals the volume of the unit cell, G represents when K is 2 π times a reciprocal lattice vector, q_i is the charge of an ion, q_j is the charge of the other ion, r_{ij} is rj - ri and i is ion denoted as “I”. The two equations are for the summation of real space, E_{real} and reciprocal space, E_{recip}. This is because in the summation the “inverse distance is rewritten as its Laplace transform and then split into two rapidly convergent series” [11], which are the two summations for real and reciprocal space. The summation has a scaling of $N^{3/2}$, where N is the no of ions, and is achieved when an optimal value of η is chosen [11].

The equation below is given in the paper by Jackson and Catlow (1988) [19] and shows the optimal way of calculating “η”:

$$\eta_{opt} = \left(\frac{nw\pi^3}{V^2}\right)^{1/3}$$

Example Equation 2 – Equation for calculating “η” [19]

“n” is the number of species in the unit cell, which includes shells, and “V” is the unit cell volume [11]. This optimal value is based on the criterion of “minimising the total number of terms to be evaluated in real and reciprocal space, weighted by the relative computational expense for the operations involved, w” [11] is achieved.

2.3.2 Short Range Potentials

The Buckingham potential is the “predominant short-range potential” for many ionic materials [11]. It is made up of a repulsive exponential and an “attractive dispersion between pairs of species” [11]. The main problem with this potential is that it “turns over” when “r” tends towards zero, with the exponential becoming a constant and “r^{-6}” going toward –infinity [8]. This results in incorrectly estimating the “minimisation energy of a structure that has very short distance between two atoms” [8]. The equation is show below:

$$V = Aexp(-r/\rho) - Cr^{-6}$$

Example Equation 3 – Equation for calculating energy minimisation [8]

Dick-Overhauser Approach

One model used to include dipolar polarizability is *via* the shell model, first introduced by Dick and Overhauser [9]. This shell model is widely used, it involves splitting an ion into a core and a shell [9]. The core is made up of the nucleus and inner electrons of the ion, therefore representing all the mass, and the shell represents the valence electrons [9]. However, this model should not be taken too literally as sometimes the shell can carry a positive charge, depending on the fitting process, such as with metal cations [9]. “The polarizability of the ion *in vacuo* is given by” [9]:

$$\alpha = \frac{q_s^2}{k_{CS}}$$

Example Equation 4 – Equation for the polarizability of the ion in vacuo [9]

The core and shell are Coulombically screened from one another with k_{CS} representing the harmonic spring force constant coupled to it and q_s represents the shell charge [9]. Short-range forces act on the shell, whereas the Coulomb potential acts on both, therefore the shell the short-range forces act to damp the polarizability by essentially increasing the spring constant, this makes the polarizability environment dependent [9].

The problem with this approach is that it is “not naturally extensible to higher order moments” [9], however attempts have been made to fix this, “such as the spherical and elliptical breathing shells” [9].

Three-Body Interactions

Three-body interactions involve the potential representing the repulsion between bond pairs or lone pairs [9]. Therefore the form chosen is generally a harmonic one that penalises deviation from the expected angle for the coordination environment, such 120° for a trigonal planar carbon atom [9]:

$$U_{ijk} = \frac{1}{2} k_b (\theta - \theta_0)^2$$

Example Equation 5 – Equation for the three-body energy [9]

U_{ijk} is the three-body energy, θ is the actual angle, θ_0 is the equilibrium angle and k_b is the bond bending force constant [9].

2.4 Lattice Energy Minimisation

There are multiple methods of lattice energy minimisation. Those that will be discussed here are the steepest descent method [8], the conjugate gradient method and the Newton-Raphson method. The steepest descent method involves performing a series of function evaluations in the negative gradient direction [8]. An approximate minimum can be estimated by "interpolation between the calculated points" [8]. This "interpolated point" is then used to begin the next line search [8]. This approach will always lower the function value and thus "guaranteed to approach a minimum" [8].

Another method of lattice energy minimisation is the conjugate gradient method. This method tries to improve on the steepest descent method by correcting its "undoing" of the previous step [8]. It does this by not performing each line search along the current gradient but rather "along a line that is constructed such that it is 'conjugate' to the previous search direction(s)" [8].

The Newton-Raphson method involves expanding the true function to second order around the current point x_0 [8]. The most efficient minimisation methods are based on Newton-Raphson [11]. The Newton-Raphson method involves the Hessian or some approximation to be used, with the minimisation search direction given by [11]:

$$\Delta x = -H^{-1} g$$

Example Equation 6 – Newton-Raphson Method minimisation search direction [11]

With H being the Hessian matrix and g is the corresponding gradient vector [11]. The minimisation method used in GULP uses the exact second matrix to "initialise the Hessian for the minimisation variables" [11]. The Broyden-Fletcher-Goldfard-Shanno (BFGS) algorithm is then used to update the hessian for the minimisation variables [11]. The process works by recalculating the Hessian when either the energy decreases by a clear criterion in one step or the angle concerning the gradient and search vectors becomes too great, with a line search performed to obtain the optimum step length along the search vector [11]. This leads to quick convergence within a limited amount of cycles [11] for the majority of systems, unless there are particularly soft modes in the Hessian [11]. In these cases, the rational function optimiser (RFO) [20] is used and attempts to get rid of imaginary modes from the hessian [11] which forces it to be positive definite [11]. The advantage of RFO is that it can cause quick convergence in cases where the default minimiser has difficulty to do so [11], however the disadvantage is that it's more expensive per cycle [11]

2.5 Mott-Littleton Method

GULP utilises the Mott-Littleton method [21] . The Mott-Littleton method involves the two region strategy [9]. A point is defined as the defect centre, which "lies at a point centric with the initial defect site"[9] or where there are 2 or more defects the "mid-point of the ensemble of point defects."[9] The surrounding space around this point is then divided into two spherical regions, regions 1 and 2a, with region 2b being designated to atoms outside these spheres and extends to infinity [9]. A model of the Mott-Littleton method is shown in Figure 1:

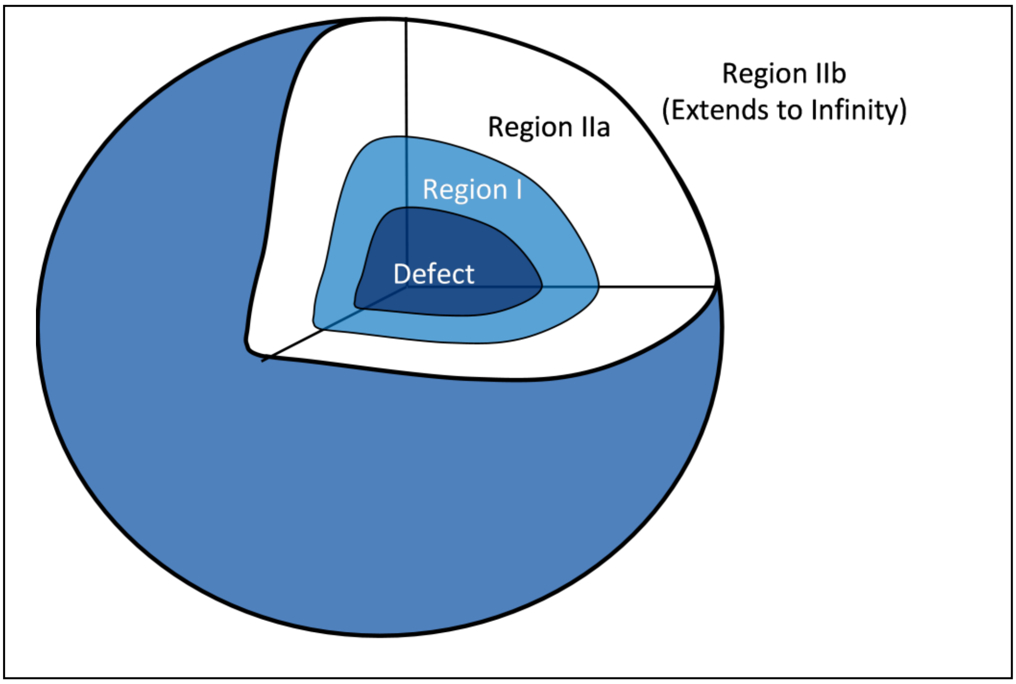

Figure 1 – A diagram of the Mott-Littleton Method (Adapted from Catlow (2006) [70])

The size of the regions are specified by the number of ions contained within them or their radii [9]. Ions in region 1 are “assumed to be strongly perturbed by the defect and therefore are relaxed explicitly with respect to their Cartesian coordinates” [9]. Ions in region 2, however, are expected to be weakly perturbed and therefore their displacements can be approximated in some way, along with the associated energy of relaxation [9]. An important stage of the defect calculation is to confirm that the defect energy is adequately converged with respect to the region radii [9], as with increasing the radii of region 1 the approximation becomes more valid [9]. To achieve convergence, it is advised that the difference between the radius of region 1 and the radius of region 2 “should be greater that the short-range potential cut-off” [9], however this may not be valid for charged defects [9].

The total energy of the two region system can be expressed as the sum of contribution from the energies within the regions and between them [9]:

$$U_{tot}(x, \xi) = U_{11}(x) + U_{12}(x, \xi) + U_{22}(\xi)$$

Example Equation 7 – Equation for the sum of contribution from the two regions [9]

$U_{11}(x)$ represents the energy of region 1 as a function of the Cartesian coordinates, x, $U_{22}(\xi)$ represents the energy of region 2 as a function of the Cartesian displacements, ξ and $U_{12}(x, \xi)$ is the energy of interaction between the two regions [9]. However, this stage does not distinguish between regions 2a and 2b [9]. The energy of region 2, as it is assumed the forces acting on region 2 are small and the atoms response in this region will only be harmonic [9], can be calculated as:

$$U_{22}(\xi) = \frac{1}{2}\xi^T H_{22}\xi$$

Example Equation 8 – Equation for the energy of region 2 [9]

With H_{22} equalling the Hessian matrix for region 2. The next equation applies the condition that the “displacements in region 2 will be the equilibrium values” [9]:

$$\left(\frac{\partial U_{tot}(x, \xi)}{\partial \xi}\right)_x = \left(\frac{\partial U_{12}(x, \xi)}{\partial \xi}\right)_x + H_{22}\xi = 0$$

Example Equation 9 – Equation for the displacements in region 2 [9]

This equation combined with the previous one allows the elimination of the energy of region 2 from the total energy without direct route to the Hessian matrix [9]:

$$U_{tot}(x,\xi) = U_{11}(x) + U_{12}(x,\xi) - \frac{1}{2}\left(\frac{\partial U_{12}(x,\xi)}{\partial \xi}\right)_x \xi$$

Example Equation 10 – Equation for the elimination of the energy of region 2 [9]

Therefore the difficulty of calculating the energy of region 1 in the potential of region 2 has been decreased to evaluation the energy of region 1 and "its interaction with region 2, without having to evaluate the self-energy of region 2" [9]. In turn, to result to partial cancellation of terms, the quantity calculated is the defect energy- "i.e. the difference between the energy of the perfect regions 1 and 2, U_{tot}, and the defective case, U^{d}_{tot}, rather than the individual contributions" [9]:

$$U_{defect}(x,\xi) = U^{d}_{tot}(x,\xi) - U^{p}_{tot}(x,\xi)$$

Example Equation 11 – Equation for the defect energy [9]

2.6 Supercell Method

The supercell method involves using GULP to generate multiple sites and create a large unit cell, so that systems can be modelled in more detail. Dopants can be added to the supercell and the results are more realistic and maybe reliable than normal defect calculations, in that concentration effects and defect-defect interactions are taken into account. Investigations that have previously used the supercell method include a study of maghemite [22], a study of $NaNbO_3$ for visible-light photocatalysis [23] and an investigation into the effects of gallium doping on $Li_7La_3Zr_2O_{12}$ [24]. Most supercells prepared have been 2x2x2 in size [23], however some have increased the size, to 3x3x3 [24] for example, in order to have more sites for doping. Other studies have analysed point defects in $ZnRh_2O_4$ [25], oxygen vacancies in ZnO and $SrTiO_3$ [26] and the role of C substitution on B sites in $AlLiB_{14}$ [27].

2.7 Solution Energy Calculations

The solution energy is the measure of the energetic feasibility of a particular dopant configuration. The calculation when using the Mott-Littleton approach uses the energies of the defects associated with that particular dopant scheme and lattice energy values. Example 1 shows an example of this calculation:

$$MO + 2Li_{Li}^{X} \rightarrow M_{Li}^{\bullet} + V_{Li}' + Li_2O$$

$$E_{sol} = \left(E(M_{Li}^{\bullet} + V_{Li}') + E_{latt}(Li_2O)\right) - E_{latt}(ZnO)$$

$$E_{sol} = \left((-13.54) + 9.69 + (-33.16)\right) - (-39.29)$$

$$E_{sol} = 2.28 \text{ eV}$$

Example 1 – The calculation of the solution energy of Zn Scheme 1 in the Mott-Littleton approach

The lower the solution energy, the more energetically preferable the dopant incorporation and the more likely it is to occur. The calculation of solution energy differs slightly when using a supercell. Only the overall formation energy and lattice energies are used rather than using vacancy values, like in the Mott-Littleton calculations. The perfect cell energy is used as well as the defect formation energy obtained from the defect calculation in GULP and other appropriate lattice energies. An example of this is shown in Example 2:

$$ZnO + 2Li_{Li}^{X} \rightarrow Zn_{Li}^{\bullet} + V_{Li}' + Li_2O$$

$$E_{sol} = \left(E_{def} + E_{latt}(Li_2O)\right) - \left(E_{perfect} + E_{latt}(ZnO)\right)$$

$$E_{sol} = \left((-28{,}683.68) + (-33.16)\right) - ((-28{,}679.42) + (-39.29))$$

$$E_{sol} = 1.87 \text{ eV}$$

Example 2 – The calculation of the solution energy of Zn Scheme 1 in the supercell

Solution energy is calculated per dopant being incorporated; therefore the value needs to be divided by the number of ions being doped into the structure to get the correct value. The different dopant schemes have different equations associated with them. These equations are shown in Equations 1-4 below.

$$MO + 2Li_{Li}^{X} \rightarrow M_{Li}^{\bullet} + V_{Li}' + Li_2O$$

$$E_{sol} = \left(E(M_{Li}^{\bullet} + V_{Li}') + E_{latt}(Li_2O)\right) - E_{latt}(MO)$$

Equation 1 – Scheme 1 equation and its accompanying solution energy equation

$$4MO + 3Li_{Li}^{X} + Nb_{Nb}^{X} \rightarrow 3M_{Li}^{\bullet} + M_{Nb}''' + Li_2O + LiNbO_3$$

$$E_{sol} = \left(E(3M_{Li}^{\bullet} + M_{Nb}''') + E_{latt}(Li_2O) + E_{latt}(LiNbO_3)\right) - 4E_{latt}(MO)$$

Equation 2 – Scheme 2 equation and its accompanying solution energy equation

$$4MO + 4Nb_{Nb}^{X} + 3Li_{Li}^{X} \rightarrow 4M_{Nb}''' + 3Nb_{Li}^{\bullet\bullet\bullet\bullet} + Li_2O + LiNbO_3$$

$$E_{sol} = \left(E(4M_{Nb}''' + 3Nb_{Li}^{\bullet\bullet\bullet\bullet}) + E_{latt}(Li_2O) + E_{latt}(LiNbO_3)\right) - 4E_{latt}(MO)$$

Equation 3 – Scheme 3 equation and its accompanying solution energy equation

$$MO + 2Li_{Li}^{X} + Nb_{Nb}^{X} \rightarrow M_{Nb}''' + V_{Li}' + Nb_{Li}^{\bullet\bullet\bullet\bullet} + Li_2O$$

$$E_{sol} = \left(E(M_{Nb}''' + V_{Li}' + Nb_{Li}^{\bullet\bullet\bullet\bullet}) + E_{latt}(Li_2O)\right) - E_{latt}(MO)$$

Equation 4 – Scheme 4 equation and its accompanying solution energy equation

$$M_2O_3 + 6Li_{Li}^{X} \rightarrow 2M_{Li}^{\bullet\bullet} + 4V_{Li}' + 3Li_2O$$

$$E_{sol} = \left(E(2M_{Li}^{\bullet\bullet} + 4V_{Li}') + 3E_{latt}(Li_2O)\right) - E_{latt}(M_2O_3)$$

Equation 5 – Scheme 1 equation for trivalent dopant and its accompanying solution energy equation

$$M_2O_3 + Li_{Li}^{X} + Nb_{Nb}^{X} \rightarrow M_{Li}^{\bullet\bullet} + M_{Nb}^{\prime\prime} + LiNbO_3$$

$$E_{sol} = \left(E(M_{Li}^{\bullet\bullet} + M_{Nb}^{\prime\prime}) + E_{latt}(LiNbO_3)\right) - E_{latt}(M_2O_3)$$

Equation 6 – Scheme 2 equation for trivalent dopant and its accompanying solution energy equation

$$M_2O_3 + 2Nb_{Nb}^{X} + Li_{Li}^{X} \rightarrow 2M_{Nb}^{\prime\prime} + Nb_{Li}^{\bullet\bullet\bullet\bullet} + LiNbO_3$$

$$E_{sol} = \left(E(2M_{Nb}^{\prime\prime} + Nb_{Li}^{\bullet\bullet\bullet\bullet}) + E_{latt}(LiNbO_3)\right) - E_{latt}(M_2O_3)$$

Equation 7 – Scheme 3 equation for trivalent dopant and its accompanying solution energy equation

$$M_2O_3 + 6Li_{Li}^{X} + 2Nb_{Nb}^{X} \rightarrow 2M_{Nb}^{\prime\prime} + 4V_{Li}^{\prime} + 2Nb_{Li}^{\bullet\bullet\bullet\bullet} + 3Li_2O$$

$$E_{sol} = \left(E(2M_{Nb}^{\prime\prime} + 4V_{Li}^{\prime} + 2Nb_{Li}^{\bullet\bullet\bullet\bullet}) + 3E_{latt}(Li_2O)\right) - E_{latt}(M_2O_3)$$

Equation 8 – Scheme 4 equation for trivalent dopant and its accompanying solution energy equation

These equations are then used to yield the solution energy as shown in the examples above, with the various numbers of each defect changed accordingly for each scheme.

2.8 Python Scripts

Scripts were created using the python programming language to run files on GULP overnight, thus increasing productivity. An example of one of the scripts is shown in Example 3:

```
from subprocess import call
call(['gulp < linbo3_sLN2_SCM1_cIn1.dat > linbo3_sLN2_SCM1_cIn1.out'], close_fds=True, shell=True)
gulp1 = open('linbo3_sLN2_SCM1_cIn1.out', 'r')
for line in gulp1:
    if "Final energy" in line:
        print(line)
        from subprocess import call
        call(['gulp < linbo3_sLN2_SCM1_cIn6.dat > linbo3_sLN2_SCM1_cIn6.out'], close_fds=True, shell=True)

        gulp6 = open('linbo3_sLN2_SCM1_cIn6.out', 'r')
        for line6 in gulp6:
            if "Final energy" in line6:
                print(line6)
                from subprocess import call
                call(['gulp < linbo3_sLN2_SCM1_cIn11.dat > linbo3_sLN2_SCM1_cIn11.out'], close_fds=True, shell=True)
```

Example 3 – A part of one of the python scripts used, gulpSCM1In1.py

Multiple scripts were created to run the different doping schemes for each of the different dopants. Python is one of many programming languages and was used here as the program GULP was run a Linux computer. Further conversion would have to be done in order for the scripts to work on a computer operating Windows or Mac. The creation of these scripts meant that files could be run on GULP automatically when the previous one finishes, thus saving time.

2.9 Summary

This chapter has explained the theory involved in simulating the materials studied in this paper. The background for the program GULP has been described and the two methods, Mott-Littleton and the supercell method, have been defined. Here, the calculations discussed later on in this paper have been explained and examples shown. This chapter has set a base for the rest of this paper. The following chapters will use a lot of terminology defined in this chapter and discuss defects being modelled in a specific material.

Chapter 3 – $LiNbO_3$

3.1 Background

Lithium niobate, $LiNbO_3$, has many applications in the field of optics because of its "good electro-optic, acousto-optic, elasto-optic, piezoelectric and nonlinear properties" [2] so much so it has often been called the "silicon of nonlinear optics"[28]. It is also popular due to its availability and versatility, having had a widespread use[29].

Mainly, dopants are used in $LiNbO_3$ to lower its photorefractive response [6]. The photorefractive response is the time taken for the materials refractive index to alter when a beam of light is incident on it. This is done as doping generally decreases the amount of Nb_{Li} present in the material, which can cause a change in the materials optical properties [30]. When $LiNbO_3$ is illuminated by light, the Nb_{Li} defects could ionize and generate photoelectrons, altering the refractive index of the material [30]. This is needed as high intensity light is used, which causes optical damage to materials with large photorefractive response such as $LiNbO_3$, to obtain second harmonic generation, which is used in industry to generate" green 532 nm lasers from a 1064 nm source" [6]. However, it is important to know the location of the dopant in the structure, as it is needed to model the mechanisms for photorefractive suppression [6]. Congruent, with a Li/Nb ratio of 0.945 [31], is the most common form of the material as when $LiNbO_3$ crystals are grown, it can be difficult to produce a stoichiometric phase [6]. It is important to know which one is being used as the threshold divalent dopant concentration, used to increase optical damage resistance, is lower in stoichiometric $LiNbO_3$ (sLN) and higher in congruent $LiNbO_3$ (cLN) [6].

Other studies used more than one dopant with $LiNbO_3$, including Er^{3+}/Yb^{3+} [32,33], with a paper adding in Pr^{3+} to create a triply doped system [34]. A monodoped Ho^{3+} [35] system was also modelled, with Ho^{3+} being co-doped with Hf^{4+}/ Yb^{3+} [36], Mg^{2+}/Yb^{3+}[37] and In^{3+}[38]. Extended X-ray absorption fine structure (EXAFS) analysis was conducted on $LiNbO_3$ [7]. The paper concluded that Zn was doped at the Li site, which contradicts the site predicted by Araujo et al. (2007)[3]. However, the dopant concentrations in the experimental study were different than those used in the modelling; therefore the modelling of systems with finite dopant concentrations will be done in this paper to garner a better understanding and comparison to the experimental data.

Computer modelling of $LiNbO_3$ has produced a variety of information. One paper deemed antisite niobium compensated by lithium vacancies the most appropriate model, using data from simulations and experimentation[3]. This same study showed that the dopants studied had the lowest solution energy when doped at both the Li and Nb sites[3]. This was supported by another paper which confirmed that 3 of the 4 the dopants it tested preferred incorporation at both these sites, with In^{3+} slightly preferring the Nb site[1].

Another study doped $LiNbO_3$ with various combinations of dopants, Fe^{3+}+Cu^{+}, Ce^{3+}+Cu^{+}, Ce^{4+}+Mn^{2+}, Fe^{3+}+Rh^{3+} and Ru^{4+}+Fe^{3+} [2].

A recent study doped $LiNbO_3$ with Er^{3+} and codoped it with In^{3+}/Er^{3+} in an attempt to increase the photorefractive-damage resistance [39]. The paper demonstrated that both the electro-optic coefficients, which is the parameter that defines how large an effect is observed for a given applied voltage [40], γ_{13} and γ_{33}, showed little dependence on doping concentration of either Er^{3+} or In^{3+} [39].

Eu has been doped into $LiNbO_3$ [41–46]. One investigation studied the defect structure and photorefractive properties of $LiNbO_3$ co-doped with Eu^{3+}, In^{3+} and Fe^{3+} [43]. The study increased the Li/Nb ratio of $LiNbO_3$ whilst keeping the dopant concentrations the same to investigate the effect the dependence of the defect structures on the photorefractive properties of the material [43]. Initially, the increase in the Li/Nb ratio caused Eu_{Li} and Fe_{Li} to be repelled by Li ions to Nb sites to form Eu_{Nb} and Fe_{Nb}, with In ions still occupying the Li sites [43] . A further increase in Li/Nb ratio results in the In_2O_3 concentration to exceed the threshold concentration, with only a small portion of In ions occupying the Li sites, with the rest occupying the Nb sites along with Eu and Fe [43]. Another study investigated a Eu^{3+}:Ti^{4+} doped thick film made using the sol-gel method [45]. Ti^{4+} was added as the Eu^{3+} doped LN film alone could not be used in wave guide devices as its refractive indices were too low [45].

Another dopant commonly used with $LiNbO_3$ is Ce^{3+}/Ce^{4+}[47–53]. In one study, Ce^{3+} had been added to improve the holographic storage properties of $LiNbO_3$, properties such as response time and stability of the holograms [48]. A triply doped system consisting of Zn^{2+}:Ce^{3+}:Cu^{2+}:$LiNbO_3$ was investigated and it was found that the light-induced scattering ability was improved and the recording time shortened, when compared to just the doubly doped system, Ce^{3+}:Cu^{2+}:$LiNbO_3$ [48]. Another study investigate a double doped system of Hf^{4+}:Ce^{4+}:$LiNbO_3$ [50]. This study found that the photorefractive properties of Hf^{4+}:Ce^{4+}:$LiNbO_3$ were enhanced compared to those of Ce^{4+}:$LiNbO_3$ [50].

In^{3+} was also doped [54–58]. It is an important optical damage resistant dopant that “improves the photoconductivity of the crystal and hence the photorefractive sensitivity” [43]. Doping In into $LiNbO_3$ can lead to the photo-damage resistance of the material being two orders of magnitude higher than that of undoped $LiNbO_3$ [54], with photo-damage resistance being important . One study doped In with Mn^{2+} and Fe^{3+}, as Mn:Fe:$LiNbO_3$ had a long recording time and the ratio of signal to noise was low, with the addition of In decreasing the recording time and increasing the signal to noise ratio [56]. Another study investigated the properties of In^{3+}:Nd^{3+}:$LiNbO_3$ [57]. It found that the In(4.0 mol%):Nd:$LiNbO_3$ had a much higher optical damage resistance than In(2.0 mol%):Nd:$LiNbO_3$ and Nd:$LiNbO_3$ [57].

Zn^{2+} has been used as a common dopant in $LiNbO_3$ [59–66]. One study doped it into $LiNbO_3$ with Ru^{4+} and Fe^{3+} as to increase the materials optical damage resistance [59]. The study showed that enhanced non-volatile storage properties were obtained in the crystal using the dual-wavelength, with the blue light being used as the recording light, as opposed to the two-colour method, with the two-colour method being a process in which the "red and blue lasers were used as recording and sensitizing light, respectively". [59]. Another study investigated the properties of Zn:Yb:Er:$LiNbO_3$ with various concentrations of Zn [60]. The Zn^{2+}, Yb^{3+} and Er^{3+} were suggested to be doped preferentially at the antisite Nb defects, with Zn^{2+} forcing Yb^{3+} and Er^{3+} to replace Nb^{4+} sites when Zn^{2+} concentration exceeds the threshold value of under 6.0 mol% [60]. It also found that the crystal doped with 6.0 mol% Zn^{2+} had the highest optical damage resistance with it being "two orders magnitude higher than that of other crystals" investigated [60]. Zn^{2+} being doped into Fe^{3+}:$LiNbO_3$ has also been investigated, as Fe^{3+}:$LiNbO_3$ is regarded as "one of the most important crystals" for use in holographic storage media, however its response time is too long and the ability for photo damage resistance is too low [61]. The addition of Zn^{2+} decreases the response time and the photo damage resistance is, again, two orders magnitude higher than that of Fe^{3+}:$LiNbO_3$, therefore the double-doped Zn^{2+}:Fe^{3+}:$LiNbO_3$ crystal shows itself to be a "very promising holographic storage material" [61]. Zn^{2+} was also found to replace antisite Nb in another study, with Zn^{4+} replacing both Nb^{4+} and Li^{+} when the concentration of Zn exceeds its threshold value, quoted as 7.0 mol% in this paper, in Zn^{2+}:Er^{3+}:$LiNbO_3$, with the Zn(7.0 mol%):Fe^{3+}:$LiNbO_3$ having the highest optical damage resistance [62]. A study investigating Zn^{2+}:Mn^{2+}:Fe^{3+}:$LiNbO_3$ also found the threshold for Zn^{2+} was less than 7.0 mol% and found that Zn(7.0 mol%):Mn:Fe:$LiNbO_3$ had optical damage resistance about three magnitudes higher than that of Mn:Fe:$LiNbO_3$ [65]. Zn^{2+}:Nd^{3+}:$LiNbO_3$ has also been investigated [66]. Again, it found that Zn(7.0 mol%):Nd:$LiNbO_3$ had the highest optical damage resistance [66].

This chapter will now describe the results of the different structures investigated, stoichiometric and congruent. The first simulation was a Mott-Littleton calculation, followed by a stoichiometric supercell and then a congruent supercell. The congruent material could only be modelled in a supercell bigger than the one used for the stoichiometric material. This is because more sites were needed to get the correct ratio of Li to Nb, as well as inputting the intrinsic defects required, i.e. a Nb_{Li} antisite as well as Li vacancies. As mentioned before, there will be focus on the Zn dopant concentration calculations specifically, as this result can be compared to those discussed previously in Bridges et al. (2012) [7].

3.2 Mott-Littleton Calculations

The interatomic potentials used in these calculations are shown below in Table 1. GULP was used to run a perfect cell to see if coordinates changed. Vacancies and Interstitials were then calculated, these are shown in Table 2, with the interstitial coordinates used taken from Araujo et al. (2007)[3]. Also in Table 2 are the vacancy and interstitials calculated by Araujo et al. (2007)[3] for comparison purposes. As shown, the results obtained in this study are very similar to that given in Araujo et al. (2007)[3].

	A (eV)	P (Å)	C (eV Å^6)
Li -O	950.00	0.261	0.0
Nb - O	1425.00	0.365	0.0
O - O	22764.00	0.149	27.88

Table 1 – Potentials used in the calculations

Atom	**Vacancy (eV)**	**Araujo et al. (2007)**[3]	**Interstitial (eV)**	**Araujo et al. (2007)**[3]
Li	9.69	9.81	-7.76	-7.08
Nb	123.93	127.56	-106.60	-104.12
O	20.38	18.98	-12.88	-9.47

Table 2 – Initial data from Mott-Littleton calculations showing the formation energies of basic defects compared to values from Araujo et al. (2007)[3]

Dopants were then introduced to the system at either the Li or Nb site, with the potentials describing the interaction of each dopant with O^{2-} shown in Tables 3-4. The energy for each of the defects was recorded and shown in Tables 5-6.

M	**A (eV)**	**P (Å)**	**C (eV Å^6)**
Zn	515.70	0.3581	0.0
Mg	1310.98	0.2997	0.0
Mn	722.30	0.3464	0.0
Fe	722.20	0.3399	0.0
Co	784.42	0.3301	0.0
Ni	2694.98	0.2670	2.198
Sr	2309.30	0.3220	0.0
Cd	876.60	0.3500	0.0
Ba	1819.70	0.3549	0.0
Pb	998.94	0.3549	0.0

Table 3 – M^{2+} - O^{2-} potentials used in the calculations

M	A (eV)	P (Å)	C (eV Å^6)
Ce	2803.18	0.3289	27.55
Pr	2091.95	0.3399	20.34
Nd	1989.20	0.3430	22.59
Sm	1950.65	0.3414	21.49
Eu	1924.71	0.3403	20.59
Gd	1881.95	0.3399	20.34
Tb	1664.28	0.3457	20.34
Dy	1782.15	0.3399	20.34
Ho	1744.25	0.3399	20.34
Er	1707.41	0.3389	17.55
Tm	1635.85	0.3399	20.34
Yb	1638.25	0.3386	16.57
Lu	1630.35	0.3385	19.27

Table 4 – M^{3+} - O^{2-} potentials used in the calculations

MO	Lattice Energy (eV)
Zn	-39.29
Mg	-41.04
Mn	-38.32
Fe	-39.21
Co	-40.00
Ni	-42.16
Sr	-34.50
Cd	-36.53
Ba	-31.92
Pb	-40.35

Table 5 – Lattice energies for the divalent dopant oxides

M_2O_3	Lattice Energy (eV)
Ce	-129.32
Pr	-130.04
Nd	-128.89
Sm	-131.79
Eu	-132.59
Gd	-133.32
Tb	-133.53
Dy	-134.38
Ho	-135.23
Er	-136.01
Tm	-136.91
Yb	-137.16
Lu	-137.62

Table 6 – Lattice energies for the trivalent dopant oxides

The dopant energy was then used to calculate solution energies for each of the possible dopant schemes. The solution energies for each scheme and dopant are shown in Tables 7.1, 7.2, 8.1 and 8.2. These solution energies are again similar to that of Araujo et al. (2007)[3]. The results here seem to confirm that the preferred scheme for doping is Scheme 2 for both divalent and trivalent dopants, suggesting that there is doping at both the Li site and Nb site.

2+						
Dopant	**Scheme 1 (eV)**	**Ref Scheme 1 (eV)**	**%**	**Scheme 2 (eV)**	**Ref Scheme 2 (eV)**	**%**
Zn	2.28	2.41	-5.39	1.69	1.40	20.89
Mg	2.38	2.33	2.15	1.77	1.38	28.26
Mn	2.36	2.53	-6.72	1.77	1.46	21.23
Fe	2.30	2.43	-5.35	1.71	1.41	21.28
Co	2.20	2.36	-6.78	1.63	1.37	19.16
Ni	2.51	2.31	8.66	1.87	1.39	34.71
Sr	3.82	4.01	-4.74	3.17	2.71	16.97
Cd	2.72	2.96	-8.11	2.21	1.79	23.32
Ba	6.29	5.64	11.52	5.42	4.56	18.86
Pb	1.52	1.50	1.33	0.91	0.57	60.53

Table 7.1 – Solution energies for divalent dopants for schemes 1,2 with values from Araujo et al. (2007)[3] for comparison.

2+						
Dopant	**Scheme 3 (eV)**	**Ref Scheme 3 (eV)**	**%**	**Scheme 4 (eV)**	**Ref Scheme 4 (eV)**	**%**
Zn	11.54	10.35	11.50	15.41	14.34	6.94
Mg	11.55	10.51	9.90	15.42	14.50	5.97
Mn	11.61	10.22	13.60	15.48	14.21	8.20
Fe	11.55	10.30	12.14	15.42	14.29	7.33
Co	11.54	10.38	11.18	15.41	14.37	6.75
Ni	11.57	10.61	9.05	15.44	14.60	5.44
Sr	12.83	10.78	19.02	16.70	14.77	11.56
Cd	12.28	10.25	19.80	16.15	14.24	11.83
Ba	14.42	13.28	8.58	18.29	17.27	5.58
Pb	10.71	9.73	10.07	14.58	13.72	5.90

Table 7.2 – Solution energies for divalent dopants for schemes 3,4 with values from Araujo et al. (2007)[3] for comparison.

3+						
Dopant	**Scheme 1 (eV)**	**Ref Scheme 1 (eV)**	**%**	**Scheme 2 (eV)**	**Ref Scheme 2 (eV)**	**%**
Ce	5.83	6.25	-6.72	3.10	2.31	33.98
Pr	5.75	6.29	-8.59	2.97	2.28	30.26
Nd	5.29	6.36	-16.90	2.49	2.33	6.65
Sm	5.98	5.86	1.96	3.21	2.19	46.35
Eu	5.88	6.48	-9.34	3.12	2.47	26.32
Gd	5.79	6.40	-9.53	3.05	2.41	26.56
Tb	5.82	6.43	-9.56	3.05	2.42	25.83
Dy	5.51	6.14	-10.26	2.78	2.17	28.11
Ho	5.61	6.26	-10.30	2.89	2.28	26.75
Er	5.55	6.19	-10.26	2.83	2.23	26.91
Tm	5.51	6.13	-10.20	2.79	2.19	27.17
Yb	5.49	6.11	-10.15	2.78	2.18	27.29
Lu	5.46	5.96	-8.39	2.75	2.04	34.56

Table 8.1 – Solution energies for trivalent dopants for schemes 1,2 with values from Araujo et al. (2007)[3] *for comparison.*

3+						
Dopant	**Scheme 3 (eV)**	**Ref Scheme 3 (eV)**	**%**	**Scheme 4 (eV)**	**Ref Scheme 4 (eV)**	**%**
Ce	8.10	6.35	27.56	15.84	14.33	10.54
Pr	7.93	6.25	26.88	15.67	14.23	10.12
Nd	7.43	6.29	18.04	15.17	14.27	6.27
Sm	8.18	6.52	25.38	15.92	14.50	9.76
Eu	8.11	6.46	25.46	15.85	14.44	9.73
Gd	8.05	6.40	25.78	15.79	14.38	9.81
Tb	8.02	6.39	25.43	15.76	14.37	9.64
Dy	7.79	6.17	26.26	15.53	14.15	9.75
Ho	7.91	6.29	25.68	15.65	14.27	9.64
Er	7.85	6.26	25.32	15.59	14.24	9.45
Tm	7.80	6.22	25.48	15.55	14.21	9.39
Yb	7.80	6.22	25.40	15.54	14.20	9.44
Lu	7.77	6.10	27.38	15.51	14.08	10.16

Table 8.2 – Solution energies for trivalent dopants for schemes 3,4 with values from Araujo et al. (2007)[3] *for comparison.*

Graphs 1 and 2 show the solution energy of each dopant scheme plotted against the dopant equivalent ionic radii. The order of preference for the schemes stays the same throughout the different dopants, 2, 1, 3 and finally 4, which agrees with Araujo et al. (2007)[3]. Table 9 shows the atomic radii of the dopants taken from Shannon (1976)[67].

2+		**3+**	
Dopant	**Ionic Radii (pm)**	**Dopant**	**Ionic Radii (pm)**
Zn	0.74	**Ce**	1.01
Mg	0.72	**Pr**	0.99
Mn	0.67	**Nd**	0.98
Fe	0.61	**Sm**	0.96
Co	0.65	**Eu**	0.95
Ni	0.69	**Gd**	0.94
Sr	1.18	**Tb**	0.92
Cd	0.95	**Dy**	0.91
Ba	1.35	**Ho**	0.90
Pb	1.19	**Er**	0.89
		Tm	0.88
		Yb	0.87
		Lu	0.86

Table 9 – The different dopants and their ionic radii (Shannon [1976][67])

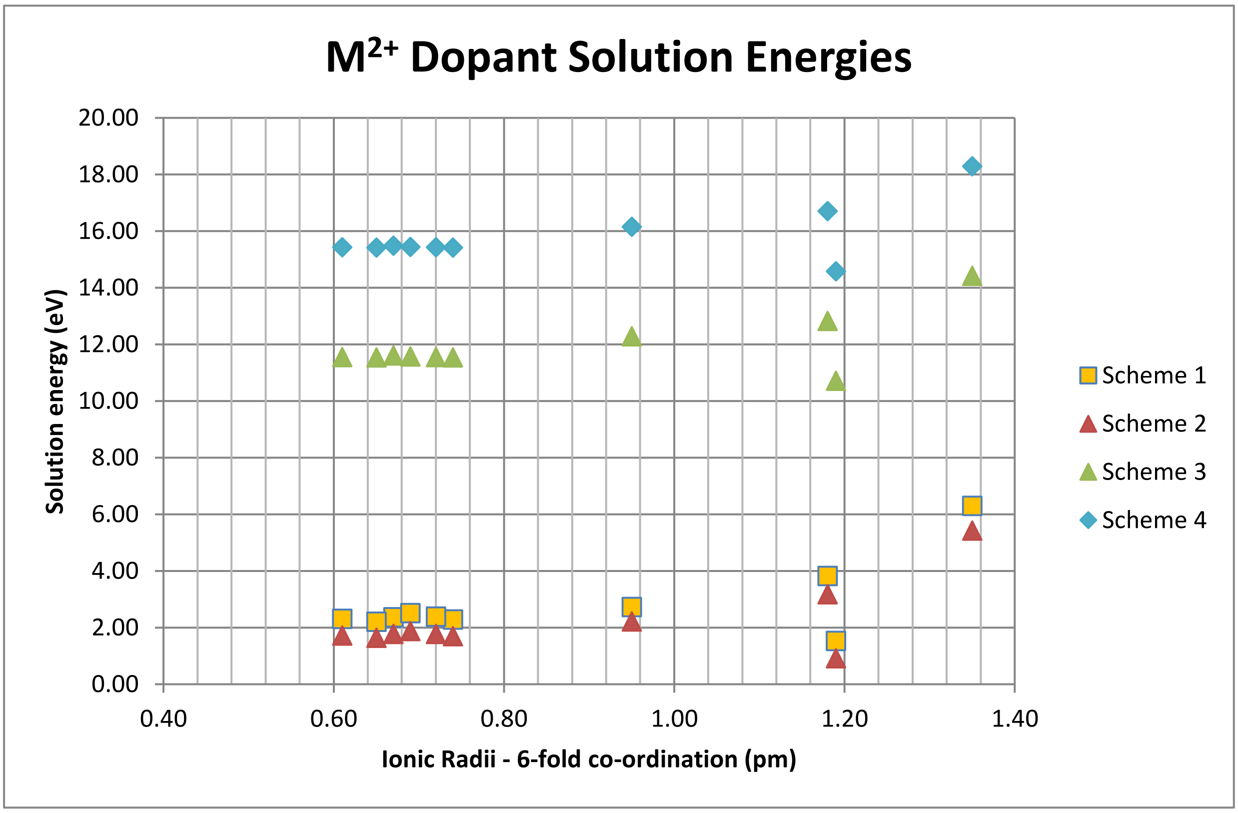

Graph 1 – Solution energy vs ionic radii for divalent dopants

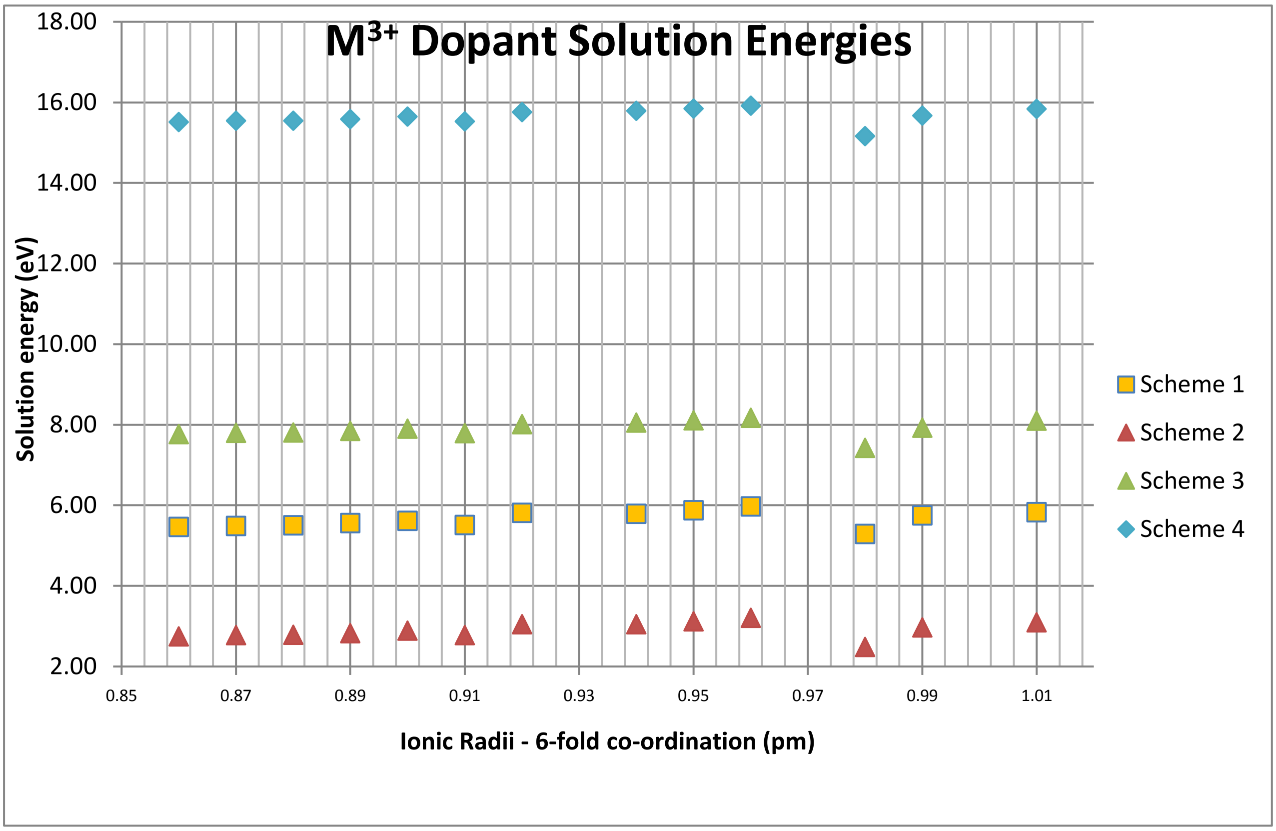

Graph 2 – Solution energy vs ionic radii for trivalent dopants

3.3 Stoichiometric Lithium Niobate

The first step was to calculate the minimum energy structure of the supercell. The lattice energy of this perfect cell was -8,478.53 eV. This energy was then noted, as it will be used in calculations later on. Multiple vacancy formation energies were then obtained for each ion. Tables 10-11 showing the values compared to those obtained previously with the Mott-Littleton approach and those obtained by Araujo et al. (2007)[3]. As shown in the tables, the values obtained are similar these previous results.

Atom	Average Vacancy (eV)	MT-LTN	Diff %
Li	9.48	9.69	-2.17
Nb	121.51	123.93	-1.95
O	19.59	20.38	-3.88

Table 10 – The initial results from the stoichiometric supercell compared to the Mott-Littleton (MT-LTN) values

The values are similar to those of Araujo et al. (2007)[3] and the values from the Mott-Littleton approach, shown in Table 10.

Atom	Average Vacancy (eV)	Araujo et al. (2007)[3]	Diff %
Li	9.48	9.81	-3.36
Nb	121.51	127.56	-4.74
O	19.59	18.98	3.21

Table 11 – The initial results from the stoichiometric supercell compared to Araujo et al. (2007)[3]

Defect calculations were then run using four different dopants, Zn, Ce, In and Eu, by implementing the different schemes mentioned before from Araujo et al. (2007)[3]. First the positions of the defects associated with that particular scheme are positioned to achieve the lowest possible solution energy. This lowest configuration was then used as a basis to start concentration calculations. The ranges for the initial configuration files for each scheme are shown below. Table 12 shows the ranges for each of the dopants schemes, with Graphs 3-6 showing the solution energy against concentration %.

M	Scheme	Min. Sol. Energy (eV)	Max. Sol. Energy (eV)
Zn	1	1.88	2.14
	2	1.06	1.54
	3	3.02	7.23
	4	5.37	10.43
Ce	1	4.76	5.22
	2	1.90	2.63
	3	3.76	4.98
	4	6.68	9.98
In	1	4.40	4.80
	2	1.69	2.24
	3	3.49	4.66
	4	6.80	9.78
Eu	1	4.90	5.32
	2	2.08	2.73
	3	3.88	5.07
	4	7.01	10.33

Table 12 – The solution energy range from the different variations of defects in each dopant scheme in the stoichiometric supercell

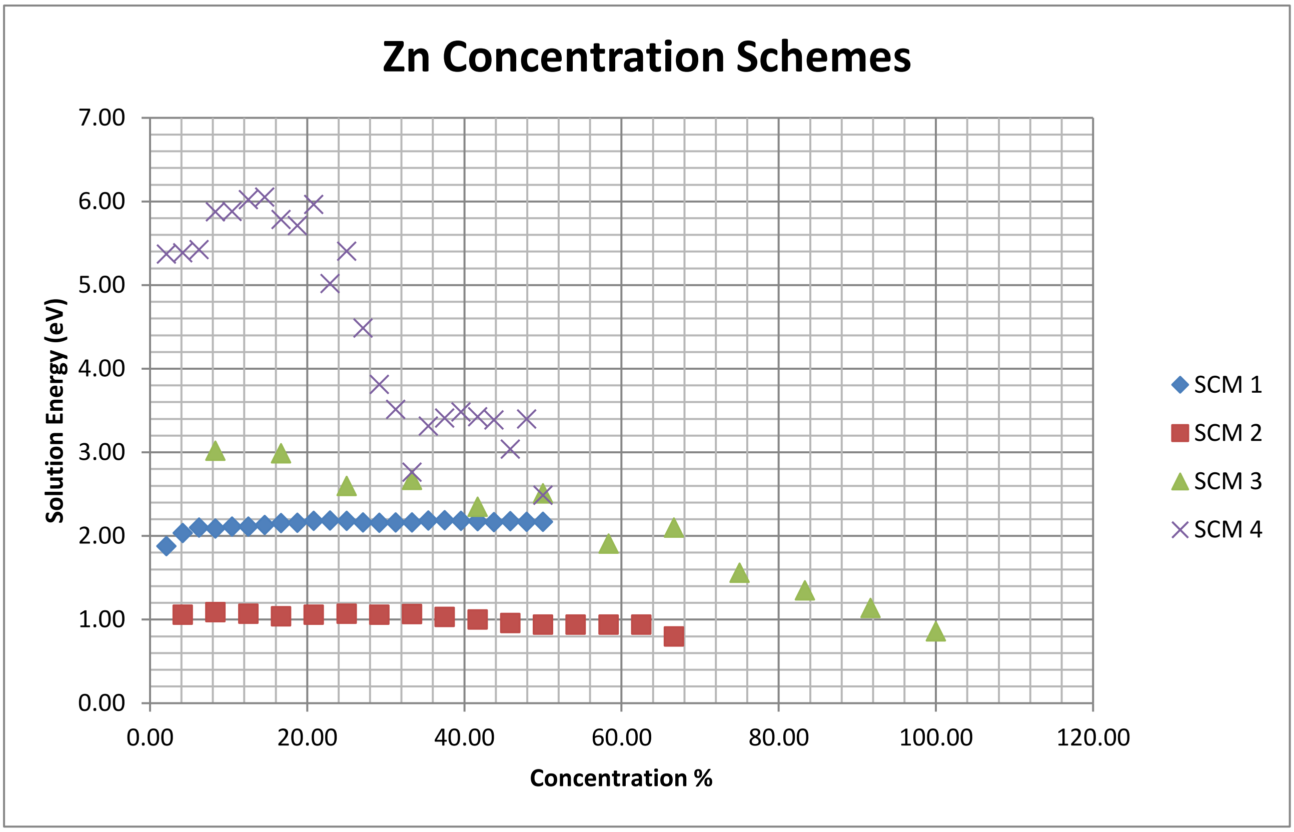

Graph 3 – The solution energies vs concentration for the concentration calculations from each Zn scheme

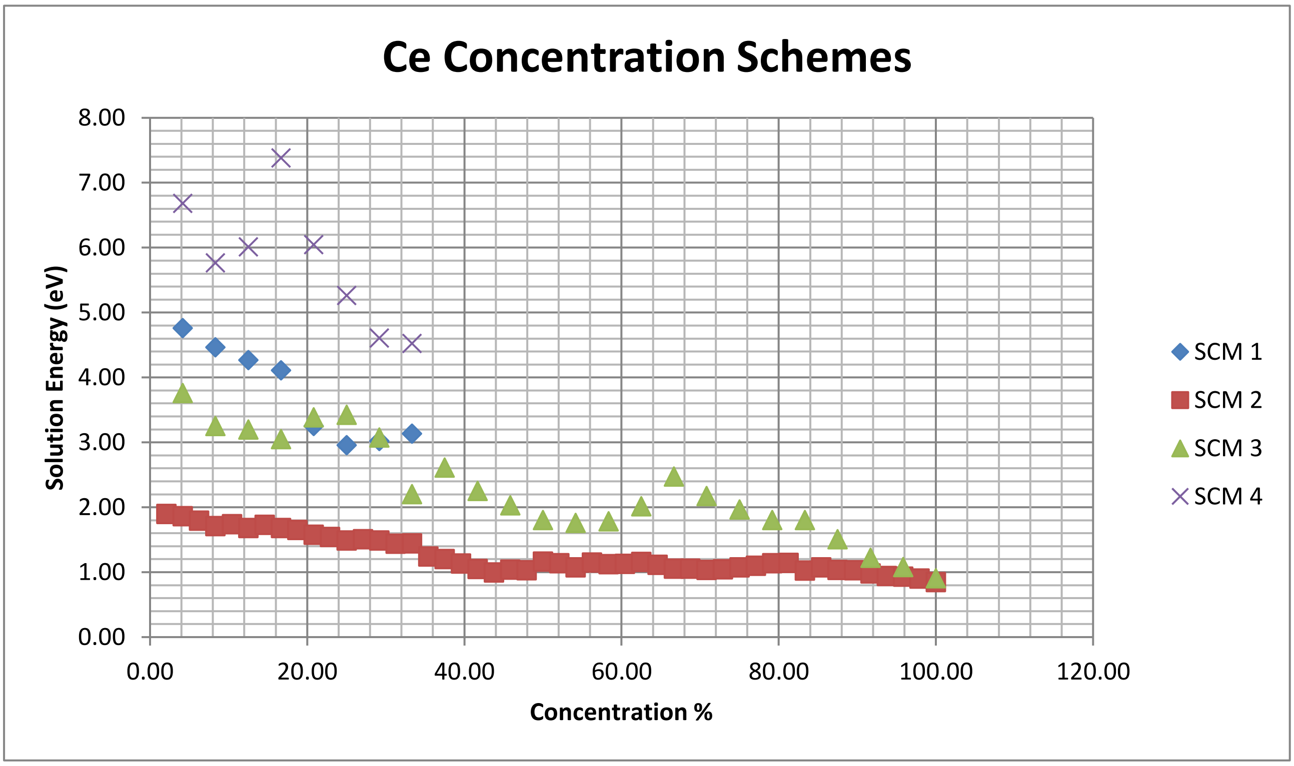

Graph 4 – The solution energies vs concentration for the concentration calculations from each Ce scheme

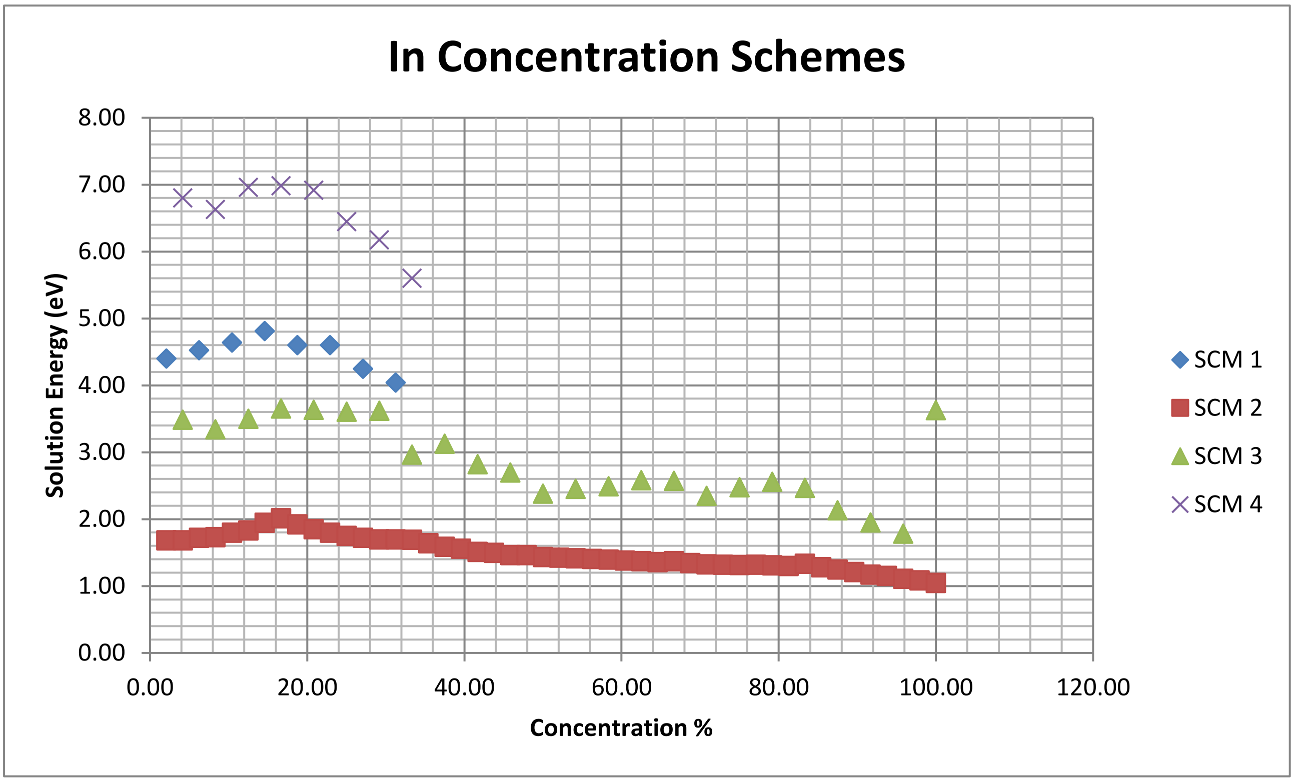

Graph 5 – The solution energies vs concentration for the concentration calculations from each In scheme

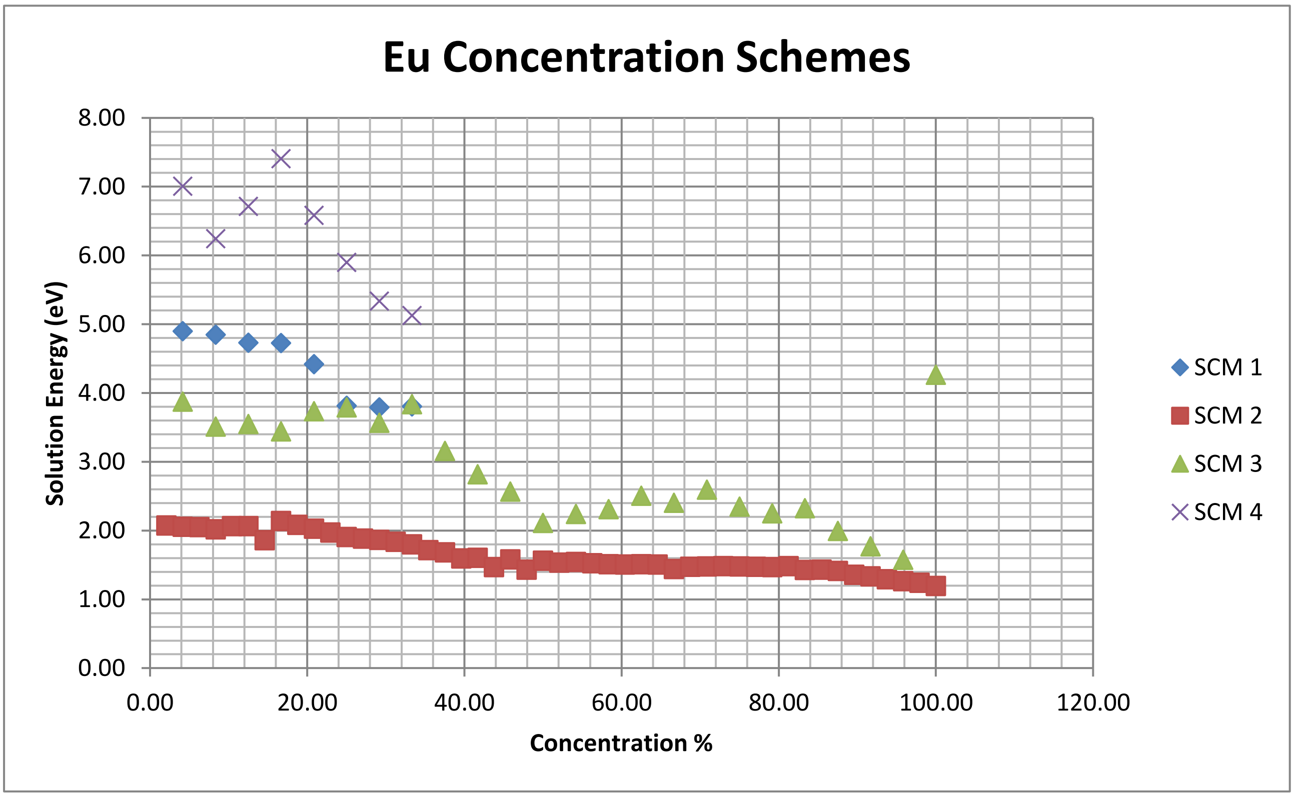

Graph 6 – The solution energies vs concentration for the concentration calculations from each Eu scheme

All the schemes match the findings from Araujo et al. (2007)[3], with Scheme 2 having the lowest solution energy across all dopants and concentrations, which was predicted as the Mott-Littleton data showed the same results. Scheme 3 has the next lowest solution energy, followed by 1 and finally 4, across all dopants. 100 % dopant concentration only has low solution energies in Zn Scheme 1, Ce Scheme 2 and Ce scheme 3. The other schemes with 100 % concentration of a dopant, Schemes 3 for In and Eu, have a high solution energy, 3.63 eV and 4.26 eV respectively, compared to the values mentioned previously for 100 % dopant concentration.

Graphs 7-10 below show the trivalent dopant schemes all together. As predicted by Araujo et al. (2007)[3] the lowest solution energy scheme is Scheme 2.

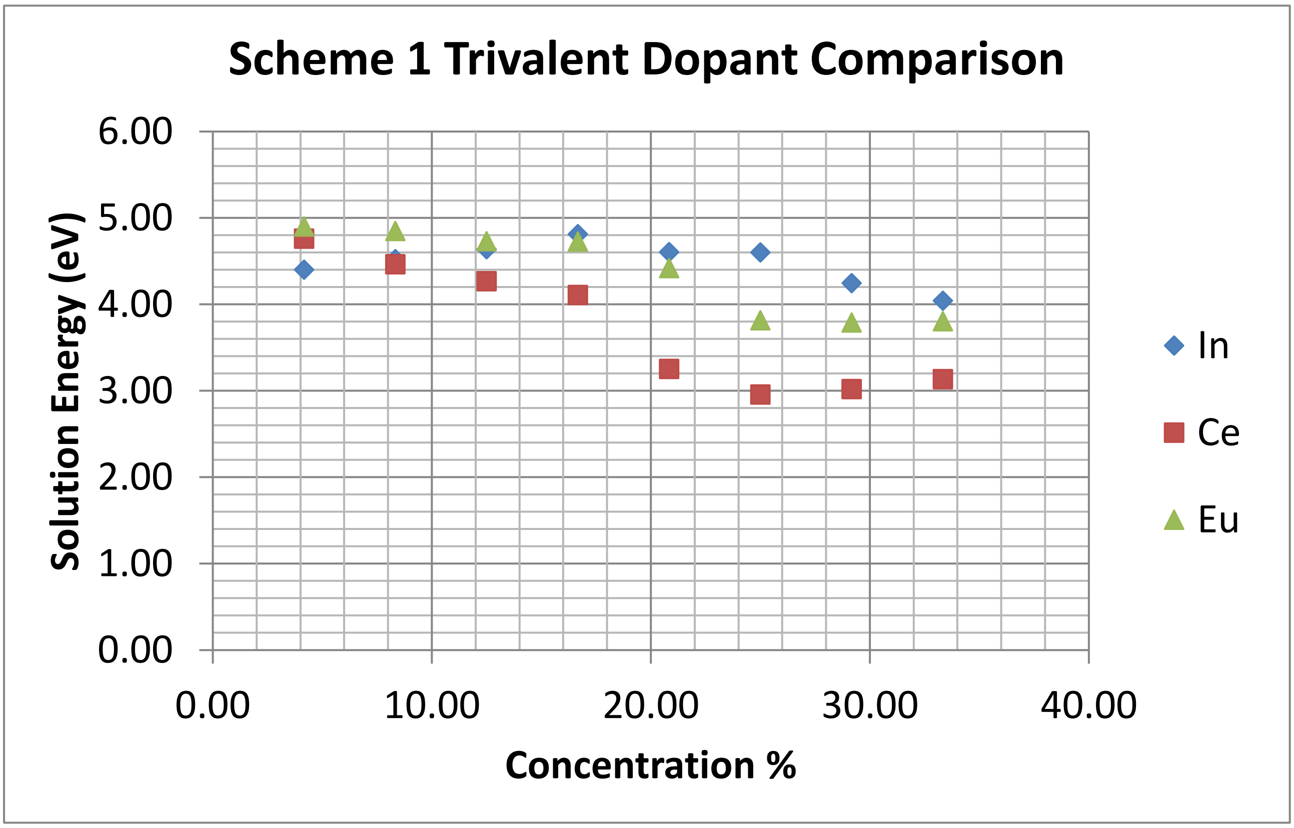

Graph 7 – The solution energies vs concentration from each scheme 1 for the trivalent dopants

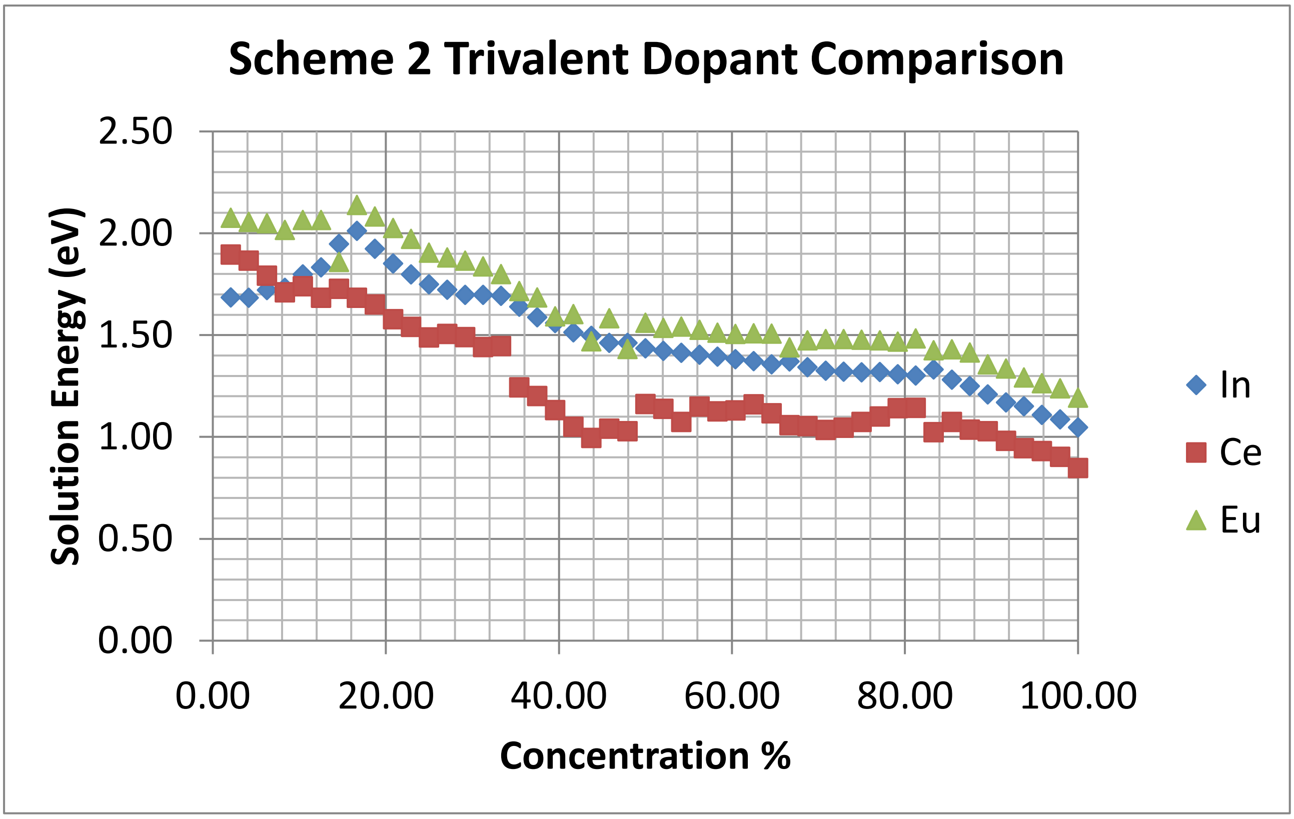

Graph 8 – The solution energies vs concentration from each scheme 2 for the trivalent dopants

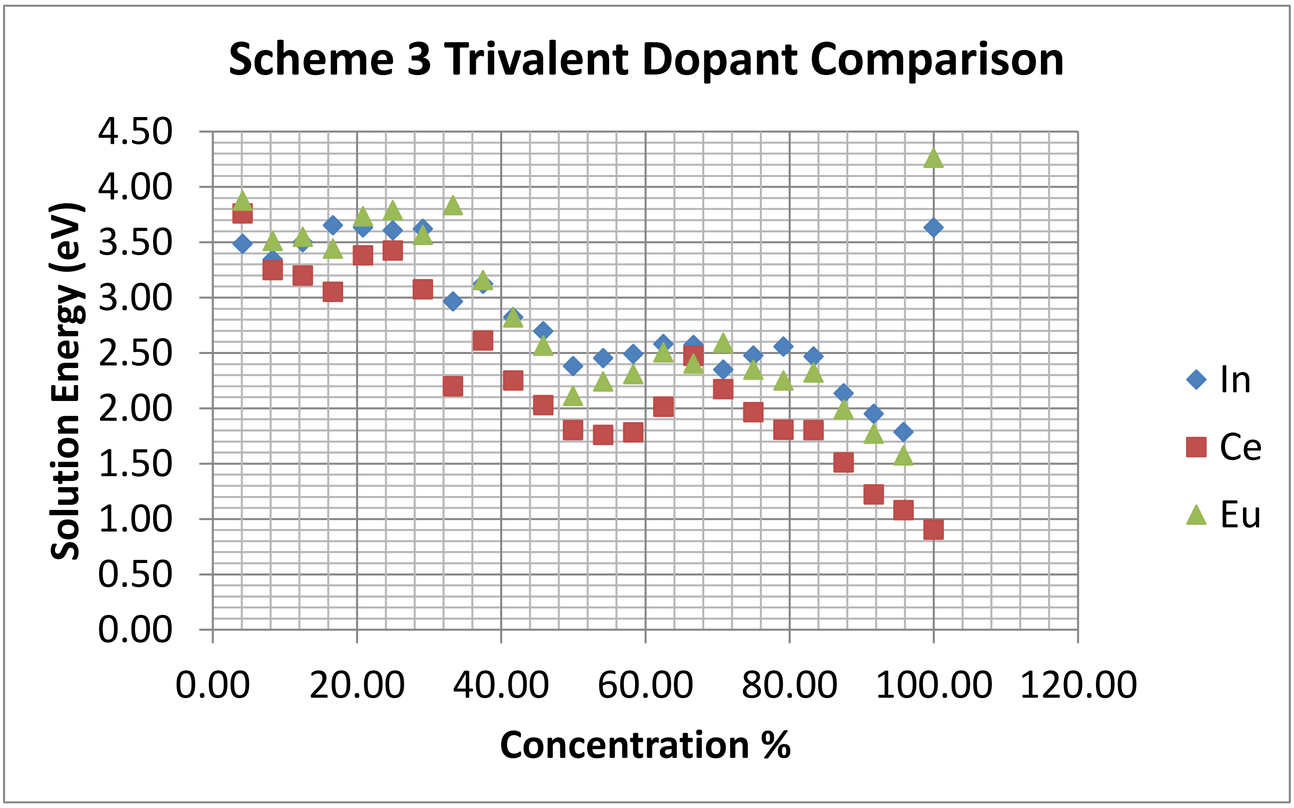

Graph 9 – The solution energies vs concentration from each scheme 3 for the trivalent dopants

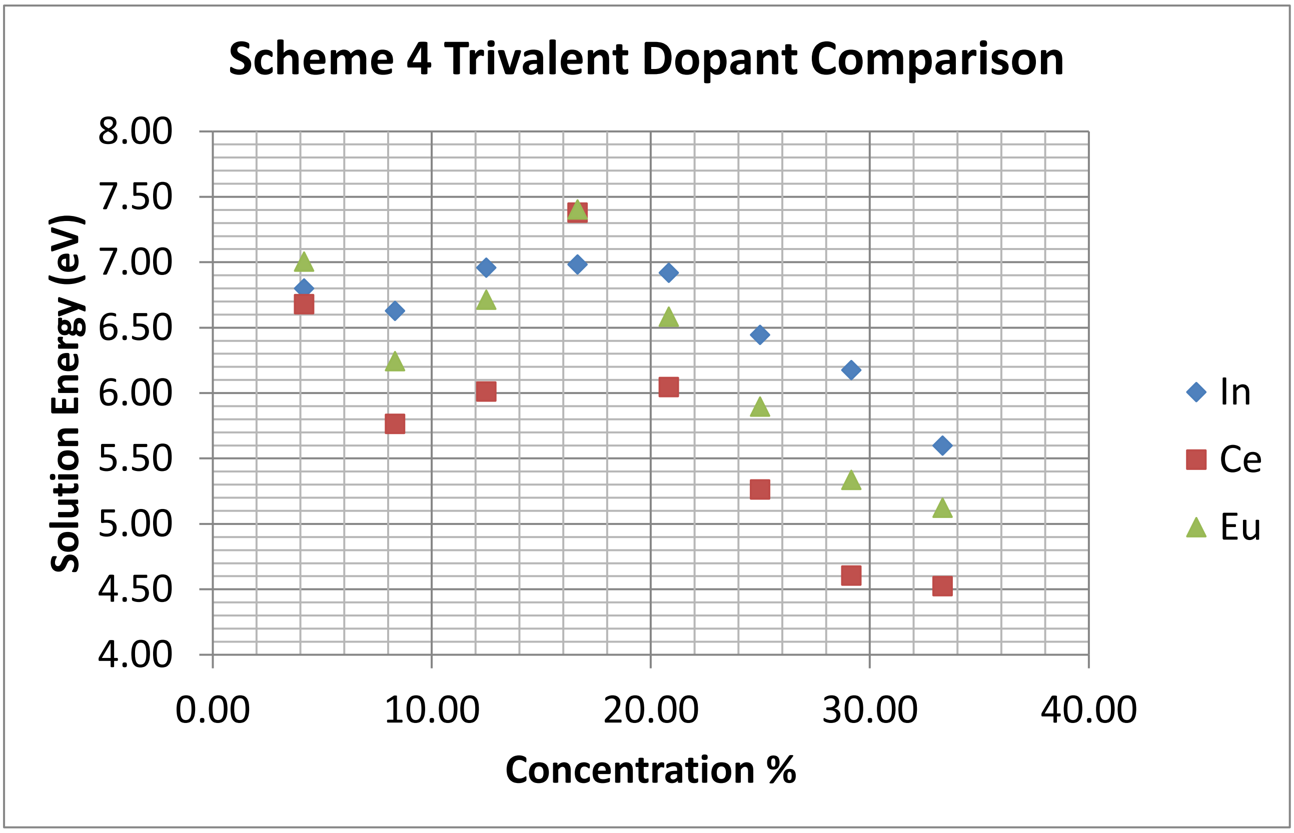

Graph 10 – The solution energies vs concentration from each scheme 4 for the trivalent dopants

In Graph 7, Scheme 1's order stays relatively the same. Ce starts off in between In and Eu with a solution energy value of 4.76 eV. Ce's value then becomes lower than that of In and Eu at every other concentration. In, however, starts off with the lowest solution energy of the three dopants and becomes the highest by around concentration 16.67% and stays that way till the maximum possible concentration of 33.33%. Eu starts off having the highest solution energy at the first concentration value and drops to in-between In and Ce at the maximum concentration of 33.33%.

Graph 8 shows Scheme 2 is generally similar to the order in the other schemes, with Ce generally having the lowest solution energy. Ce does, however, again not have the lowest solution energy at the first concentration value.

Scheme 3, shown in Graph 9, is a scheme that is of interest. In and Eu both have high solution for 100% concentration whereas Ce has a low solution energy of 0.90. The 100 % values for In and Eu are both higher than the previous concentration values before them suggesting these are maybe anomalies.

Finally, Graph 10 shows Scheme 4, which is again the lowest of the others and of relatively little interest. The values for Ce and Eu at 16.67 % seem to differ to the pattern predicted by the other values, as they are much higher, 7.38 and 7.41 respectively.

3.4 Congruent Lithium Niobate

Initial Data

Firstly, multiple files were created with the ‘cLN’ intrinsic defects, the Nb_{Li} antisite and five Li vacancies, in various positions and ran through GULP to see the effect the defects have on the energy of the supercell. The range did not vary greatly, -28,679.42 eV to -28,680.06 eV. The perfect cell energy of the supercell before the congruent defects were added was -28,615.04 eV

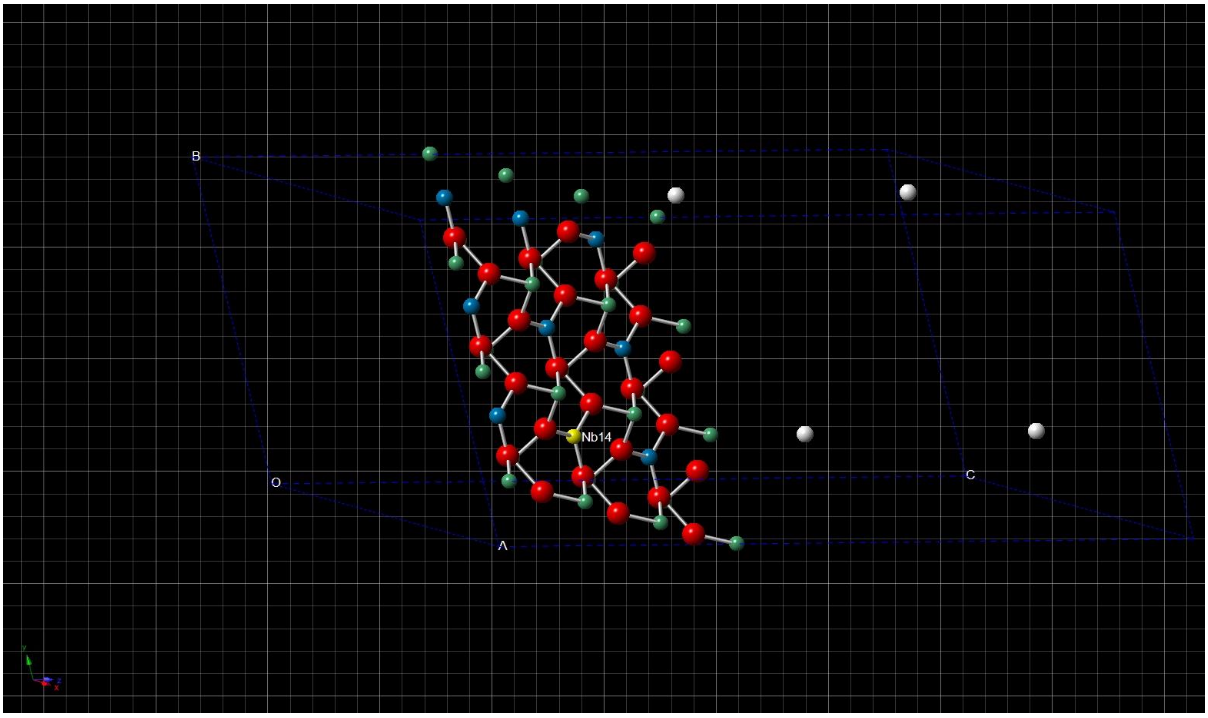

Image 1 – Cropped image showing the location of the cLN defects, the location of the Li vacancies are shown in white and the Nb at a Li site is shown in yellow. O atoms are shown in red, Li atoms in blue and Nb atoms are in green.

The cell, which provided the lowest energy, was then used, -28679.42 eV. This was then treated as the perfect cell for the following defect calculations. This value was chosen as there was not much difference between the different cells and also because the highest value might obtain a lower solution energy. Multiple vacancies at different sites were calculated for each Li, Nb and O by removing one to 18 atoms. Table 13 below shows the average vacancy for each atom calculated from removing various amounts of each atom from the supercell.

Atom	Average Vacancy formation energy (eV)	Araujo et al. (2007)[3]	Diff %
Li	9.48	9.81	-3.36
Nb	121.55	127.56	-4.71
O	20.11	18.98	5.95

Table 13 – The initial results from the congruent supercell compared to Araujo et al. (2007)[3]

As shown in the table, the values are similar to that obtained by Araujo et al. (2007)[3]. Table 14 shows the average vacancy formation energies compared to those obtained using the Mott-Littleton approach.

Atom	Average Vacancy (eV)	MT-LTN	Diff %
Li	9.48	9.69	-2.17
Nb	121.55	123.93	-1.92
O	20.11	20.38	-1.32

Table 14 – The initial results from the congruent supercell compared to Mott-Littleton values

The values again are similar, with the vacancy formation energies being lower than the Mott-Littleton values. Table 15 shows the vacancy values compared to the previous supercell of stoichiometric lithium niobate.

Atom	Average Vacancy (eV)	sLN Average Vacancy	Diff %
Li	9.48	9.48	0.00
Nb	121.55	121.51	0.03
O	20.11	19.59	2.65

Table 15 – The initial results from the congruent super cell compared to the same values from stoichiometric super cell

These values show that having internal defects already within the supercell structure has limited effect on the value of the vacancy formation energies.

Dopants were then added to the supercell, Zn, Ce, In and Eu, using the schemes mentioned previously. Table 16 show the ranges for each dopant. There are some overlaps between 3 and 4, however lowest energies are obtained for Scheme 2 throughout.

M	Scheme	Min. Sol. Energy (eV)	Max. Sol. Energy (eV)
Zn	1	1.87	2.49
	2	0.42	1.69
	3	4.05	7.55
	4	5.85	11.75
Ce	1	5.12	5.55
	2	1.83	3.26
	3	4.16	5.60
	4	7.85	11.23
In	1	4.50	5.02
	2	1.27	2.86
	3	3.75	5.27
	4	7.48	10.86
Eu	1	5.22	5.64
	2	1.89	3.32
	3	4.24	5.67
	4	7.84	11.32

Table 16 – The solution energy range from the different variations of defects in each dopant scheme in the congruent super cell

The concentrations of the various defects were then calculated for each of the dopants. Graphs 11-14 show each dopant, with solution energy vs concentration %.

Graph 11 shows all the concentrations of Zn schemes on one plot. Scheme 2 is still the preferred scheme for Zn, which is doping at both the Li and Nb sites. It also shows that the solution energy for Scheme 3 with around 98 % doped Zn at the Nb site, is higher than that of the 65.20 % value from Scheme 2, which is doping at both the Li and Nb site, 1.16 compared to 0.67. The solution energy for 48.15 % concentration for Scheme 4, 10.89, is an outlier, as the file could not be optimised. Scheme 3 looks to leapfrog scheme 1 as the second preferred scheme at around the 50 % concentration.

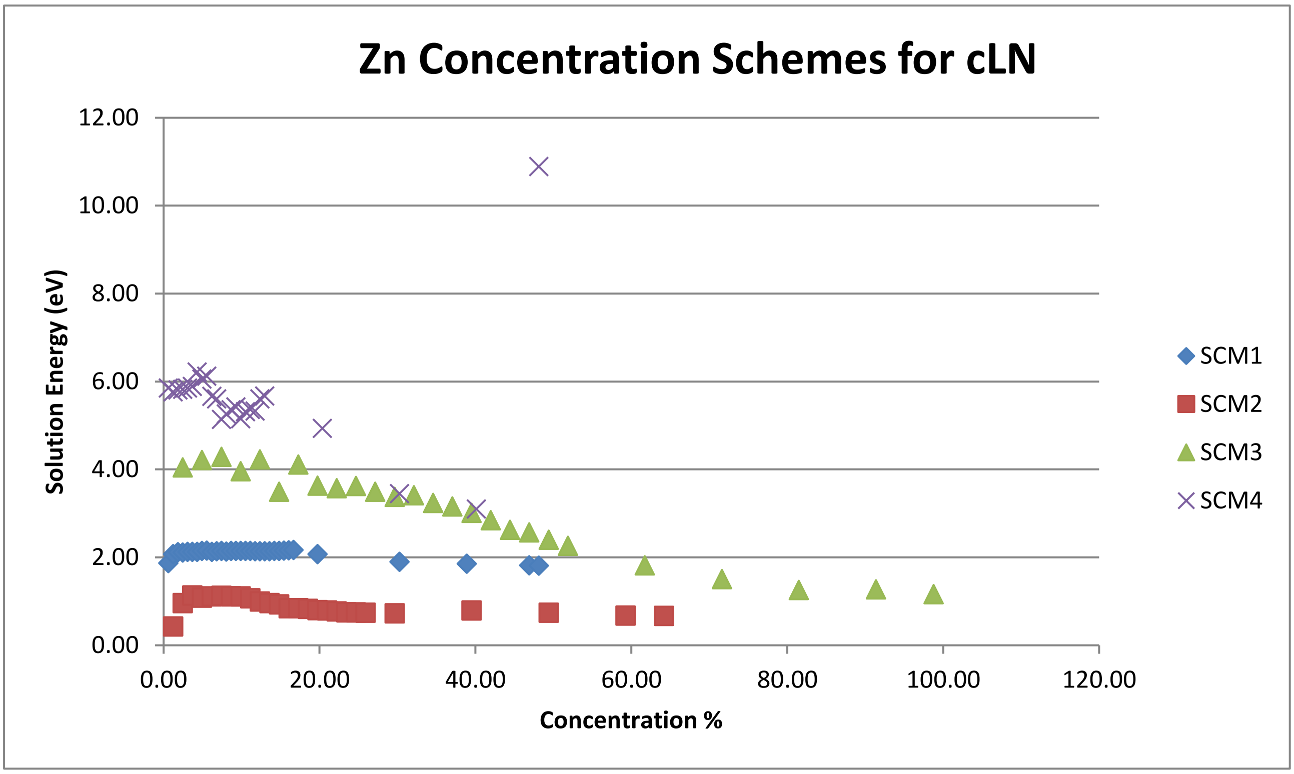

Graph 11 – The solution energies vs concentration for the concentration calculations from each Zn scheme in the congruent super cell

The concentrations for Ce doping are shown in Graph 12. The order is as predicted with Scheme 2 having the lowest solution energy throughout the concentrations. However, there is some cross over between Scheme 1 and 3 around the 17% concentration value. Scheme 1 goes from third preference to second preference, as has lower solution energy than scheme 3 from 17.28-32.10 % concentration. Scheme 2 has again a low solution energy value of 1.83 for 0.62%, much lower than the other values.

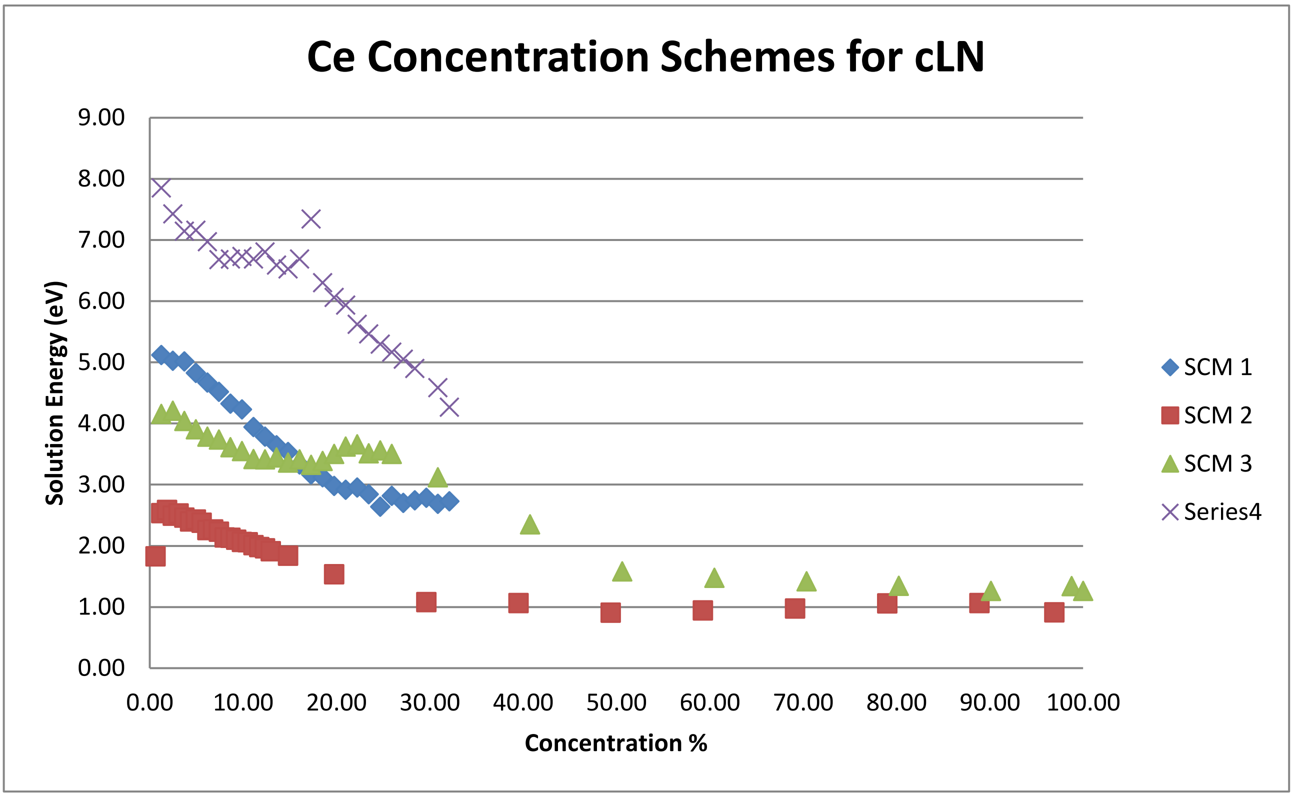

Graph 12 – The solution energies vs concentration for the concentration calculations from each Ce scheme in the congruent super cell

The concentrations for in doping are shown in Graph 13. The order is as predicted, with Scheme 2 having the lowest solution energy, and there is no crossing over of any of the schemes. Again, Scheme 2 has a low concentration value at 0.62%, similar to that of Ce and Zn, before, again, increasing as the concentration values of In increase.

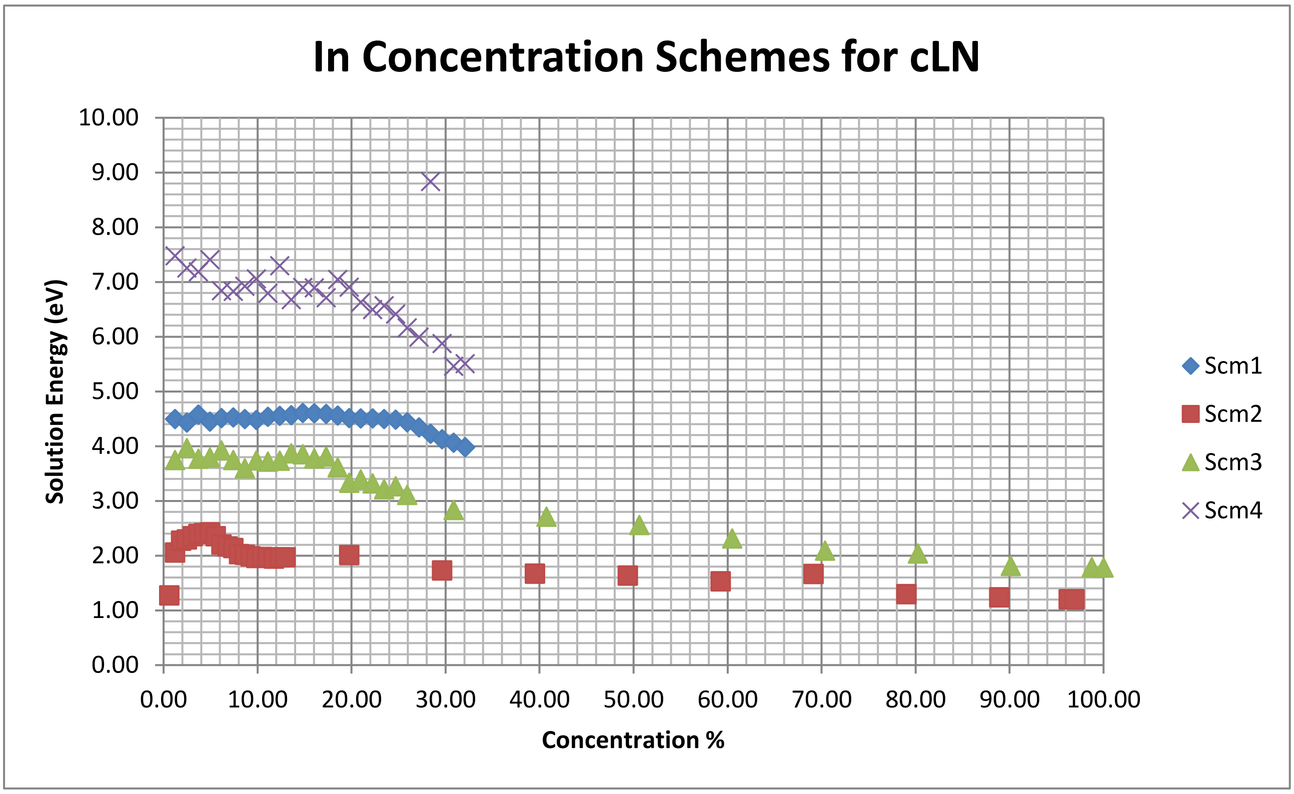

Graph 13 – The solution energies vs concentration for the concentration calculations from each In scheme in the congruent super cell

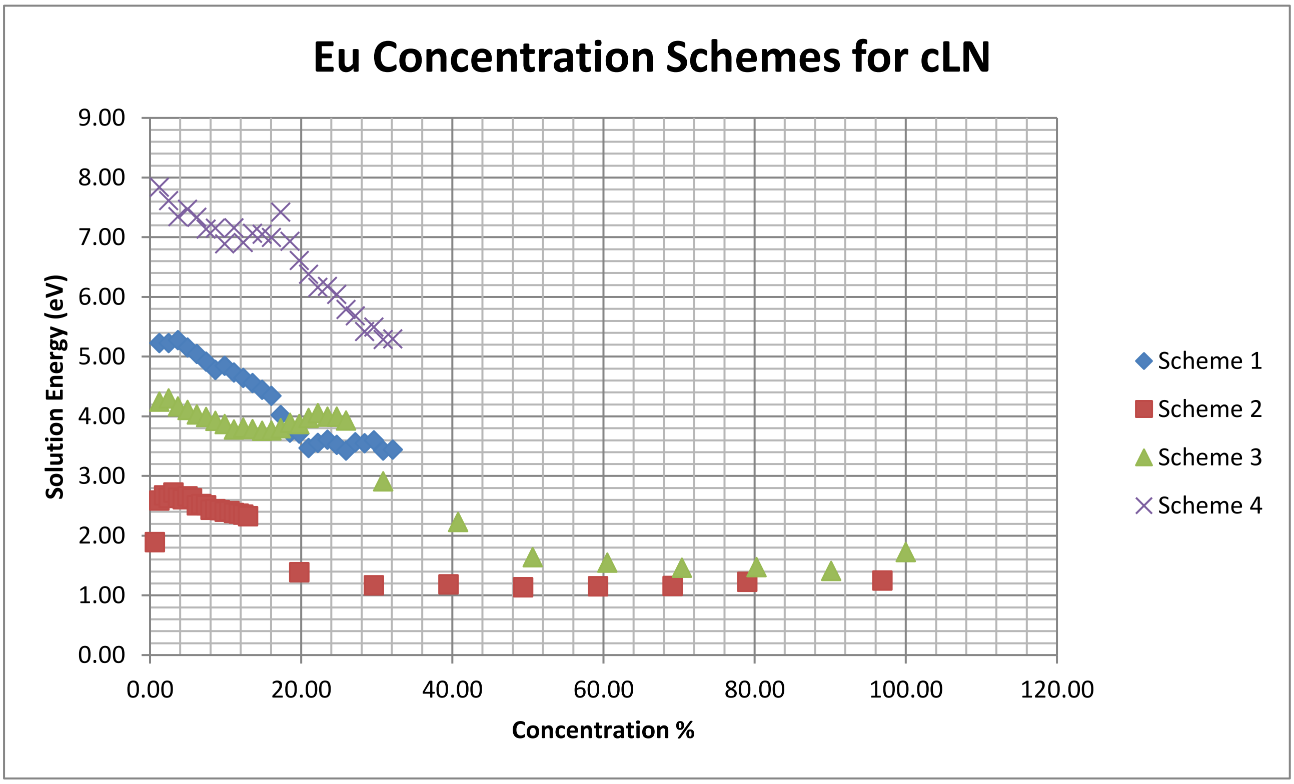

Graph 14 – The solution energies vs concentration for the concentration calculations from each Eu scheme in the congruent super cell

Graphs 15-18 overlap the different schemes of the trivalent dopants. Generally, the dopant with the lowest solution energy seems to be Ce, followed by Eu and then In. However, in every Scheme, In starts off having the lowest solution energy and gradually, by the last concentration value, has the highest.

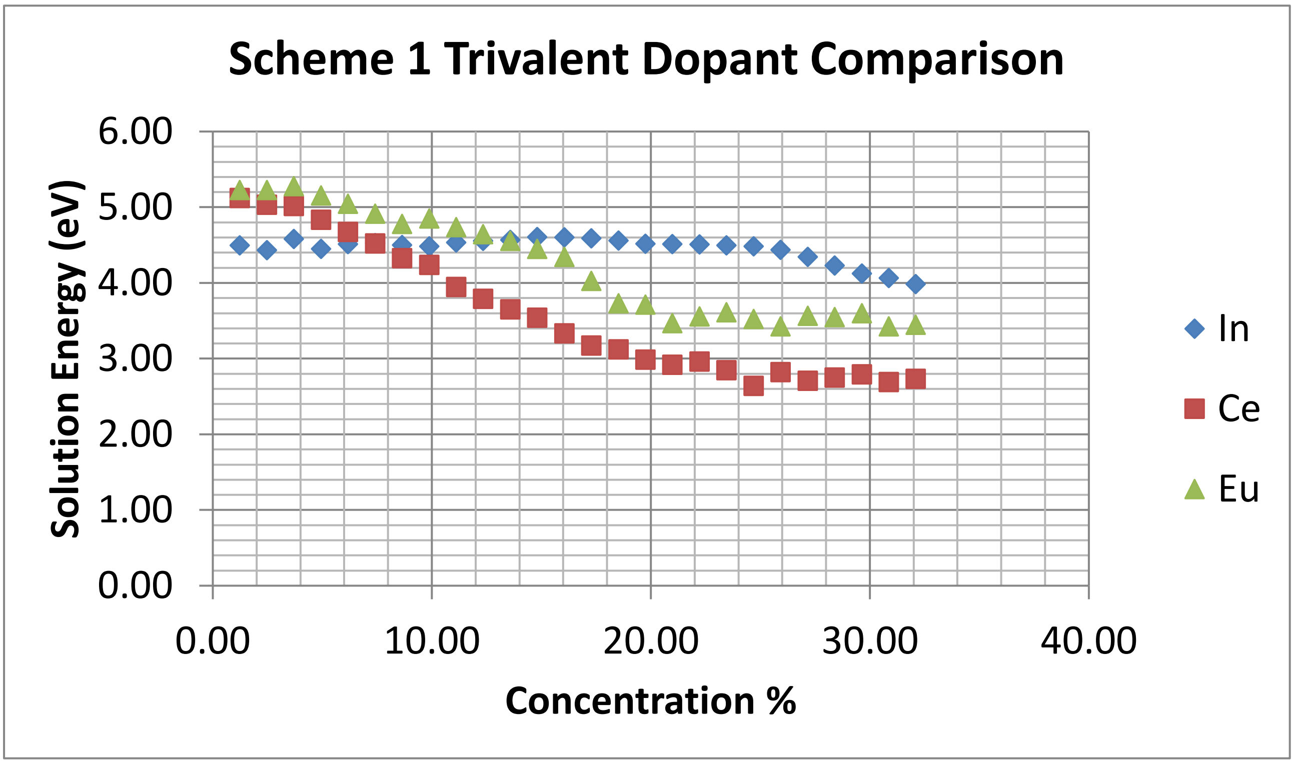

Graph 15– The solution energies vs concentration for the concentration calculations from each Scheme 1 of the three trivalent dopants, In, Ce and Eu

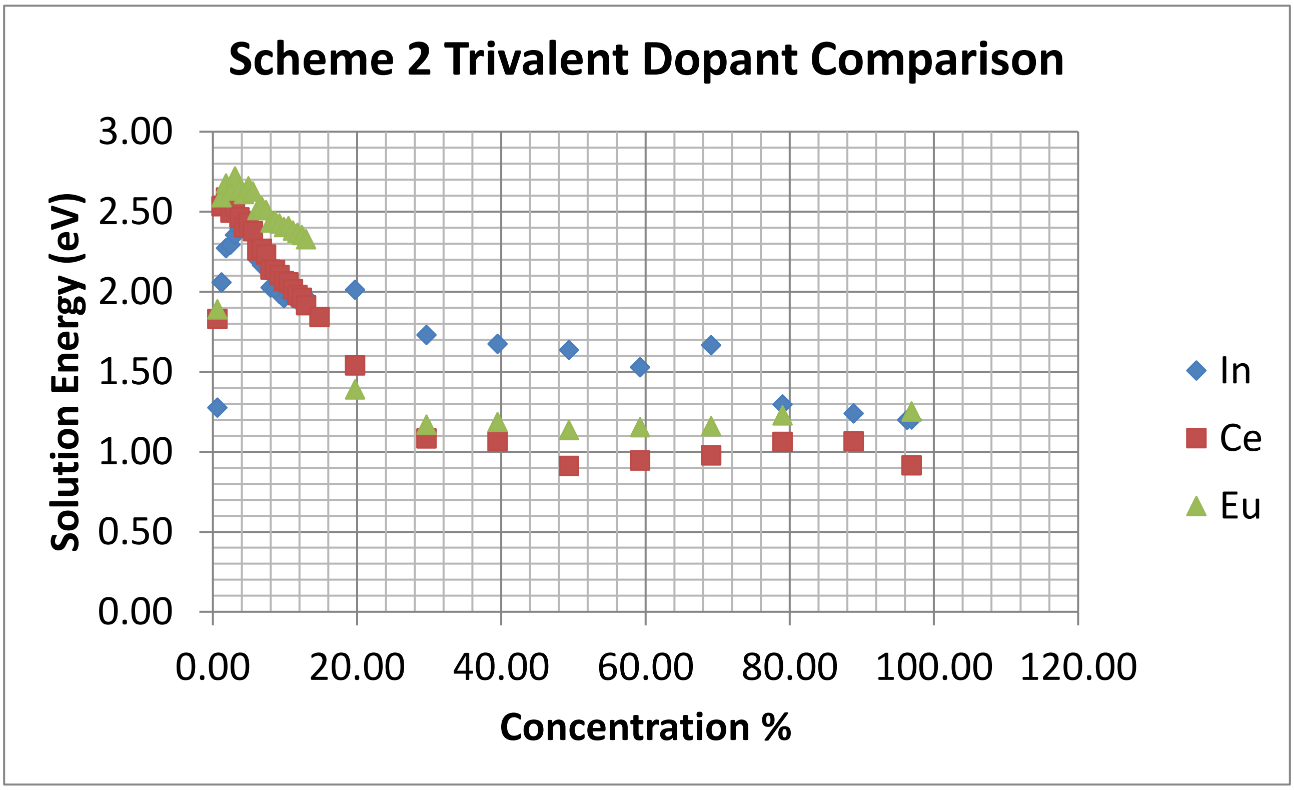

Graph 16– The solution energies vs concentration for the concentration calculations from each Scheme 2 of the three trivalent dopants, In, Ce and Eu

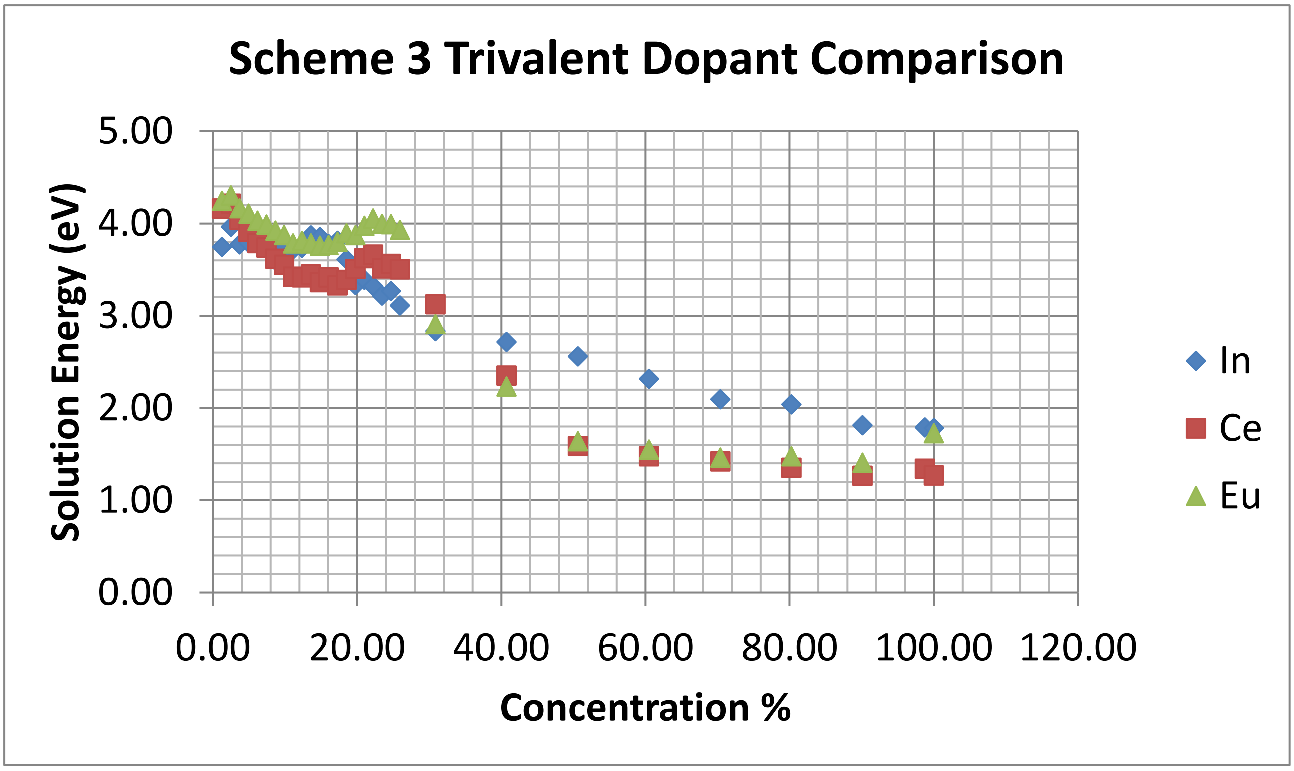

Graph 17– The solution energies vs concentration for the concentration calculations from each Scheme 3 of the three trivalent dopants, In, Ce and Eu

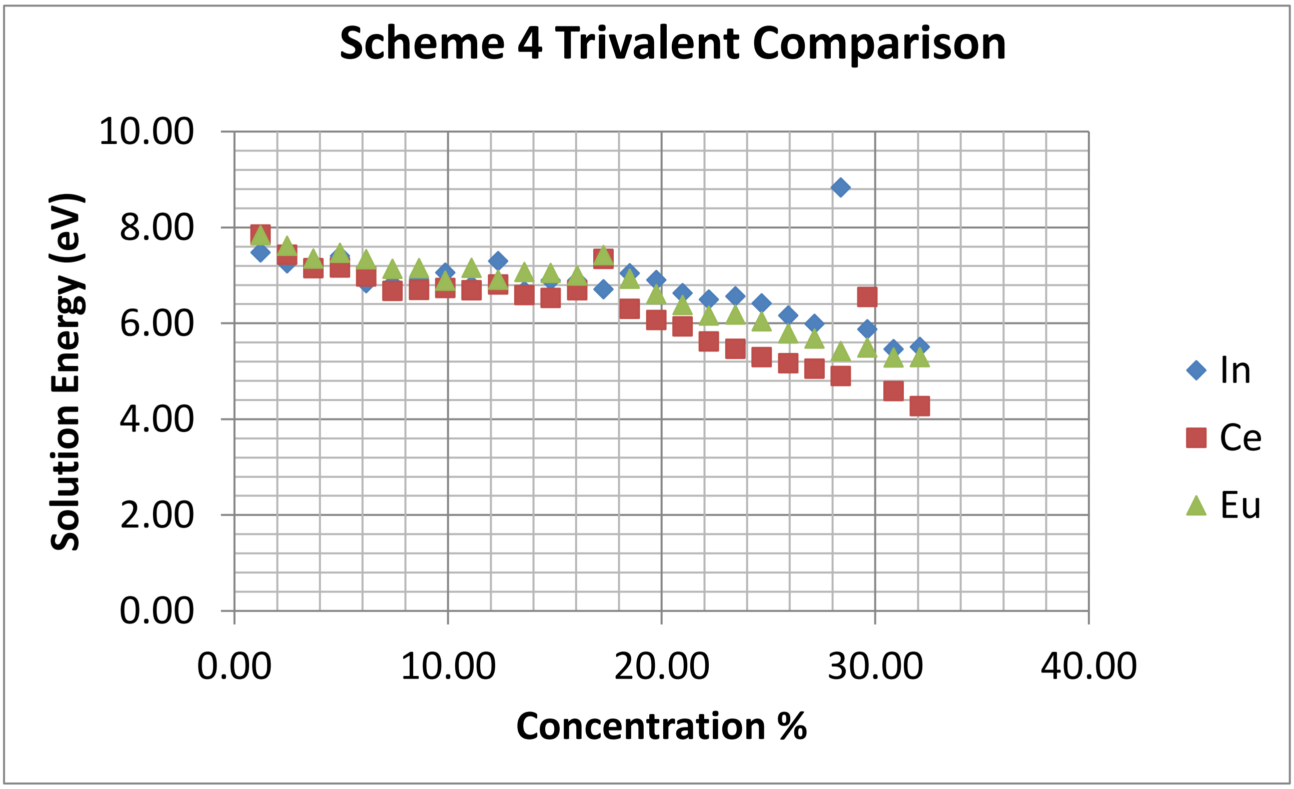

Graph 18– The solution energies vs concentration for the concentration calculations from each Scheme 4 of the three trivalent dopants, In, Ce and Eu

Scheme 2, shown in Graph 16, has the lowest solution energy across all the concentrations, with Ce having the lowest solution energy of the trivalent dopants, followed by Eu and finally In. This again confirms the findings in Araujo et al. (2007)[3], that doping does indeed occur at the Nb site as well as the Li site. The pattern of having a low solution energy at 0.62% then rising is apparent when looking at Graph 16.

Overall, the dopants behaved as expected, with Scheme 2 remaining the preferred doping scheme, meaning that there is doping at the Nb site as well as the Li site. The comparison chapter later on will compare the results here to stoichiometric LN and see if there are any differences in the schemes.

3.5 sLN vs cLN

Zn Schemes

The following section contains graphs comparing the solution energies of the concentration of dopants both in cLN and sLN, both using a supercell containing 162 Li sites and 162 Nb sites. The Zn schemes are shown below in Graphs 19-22. Scheme 2 has the lowest solution energy across all concentrations in both the stoichiometric and congruent phases. The congruent phase starts off with a significantly lower solution energy compared to the stoichiometric phase. In Scheme 2, at 1.23% Zn concentration, the solution energy for cLN is 0.43 whereas the solution energy at in stoichiometric Zn with the same concentration is 1.32. This could indicate that the presence of the defects already present in the perfect cell of cLN makes it easier to dope. This difference in the initial solution energy only occurs in schemes 1 and 2 and at low concentrations, at 0.62% Zn in Scheme 1 and 1.23% in Scheme 2. After these values, the solution energies are the same through to max concentration, around 50% in Scheme 1 and 65% in Scheme 2. Schemes 1 and 2 both have doping at the Li site, which is where the congruent defects are located, which could be a reason for the difference.

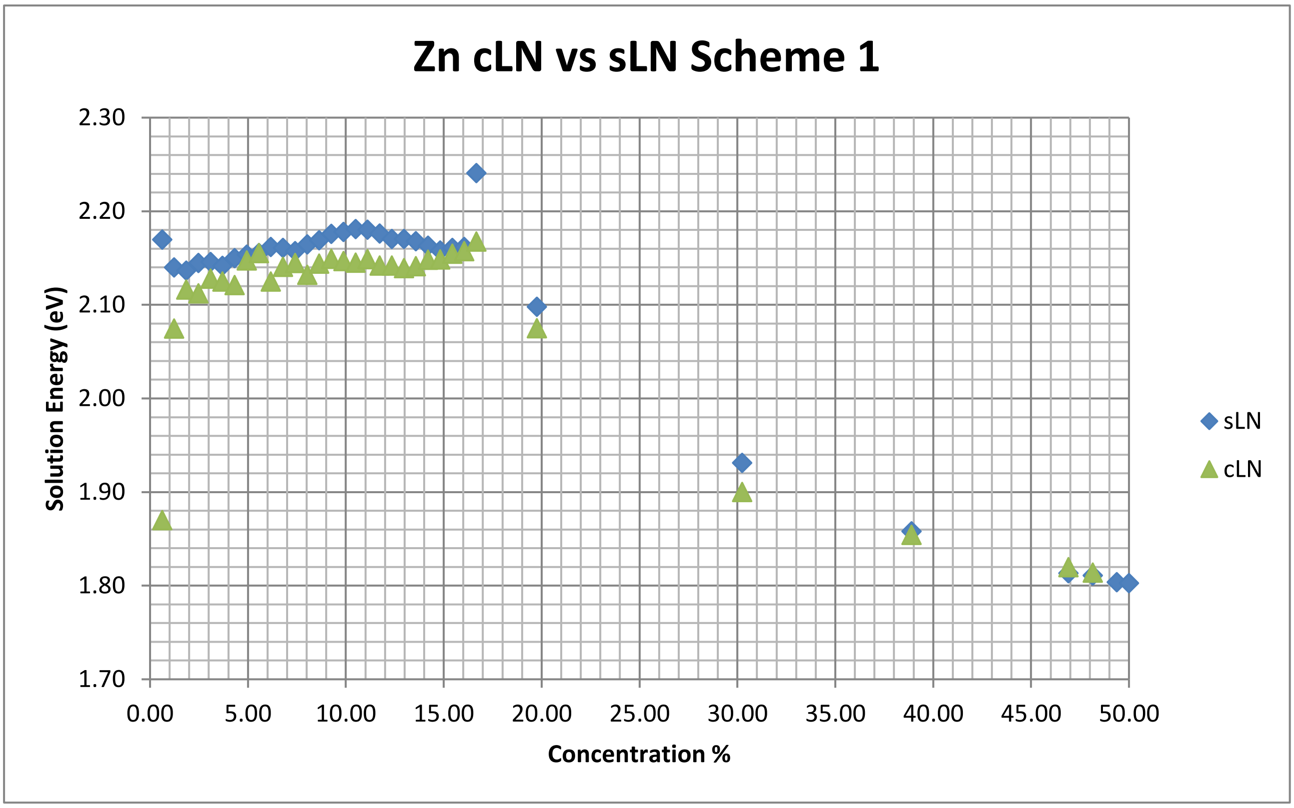

Graph 19 – The solution energies for scheme 1 Zn concentrations from cLN and sLN

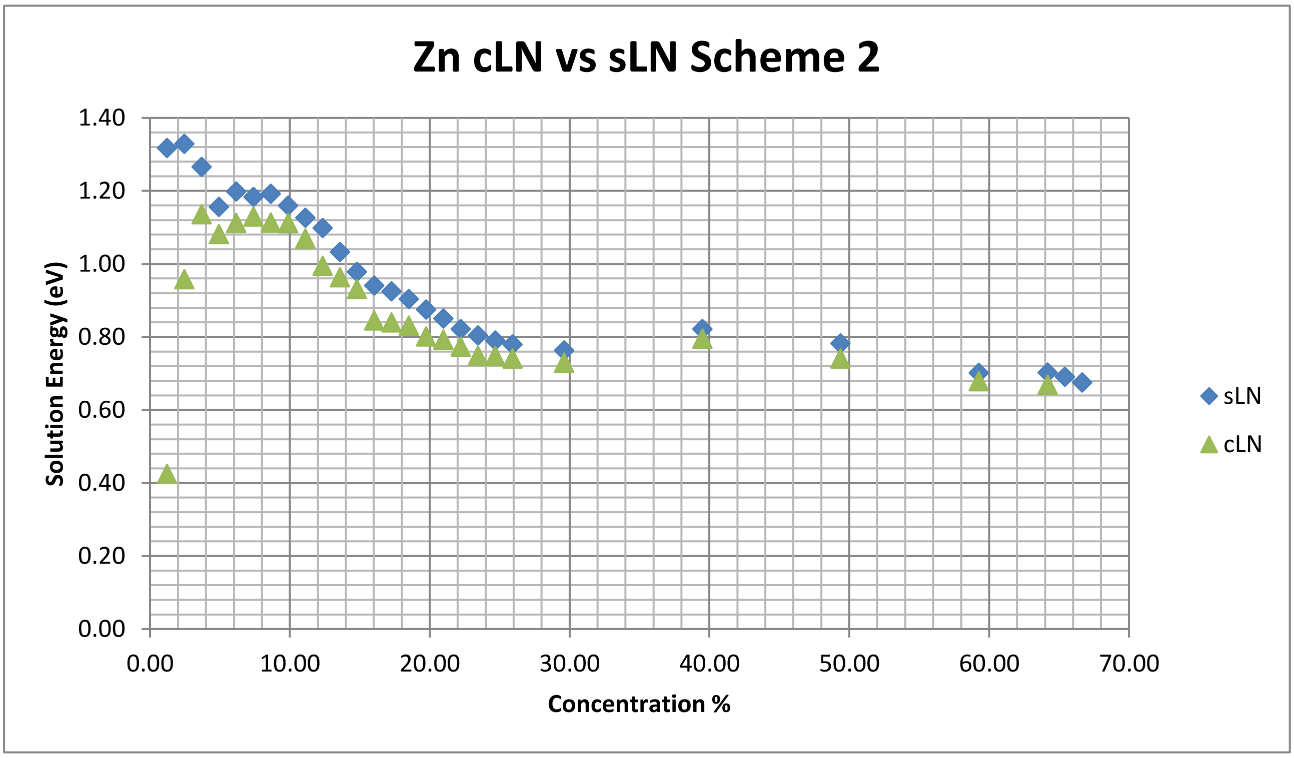

Graph 20 – The solution energies for scheme 2 Zn concentrations from cLN and sLN

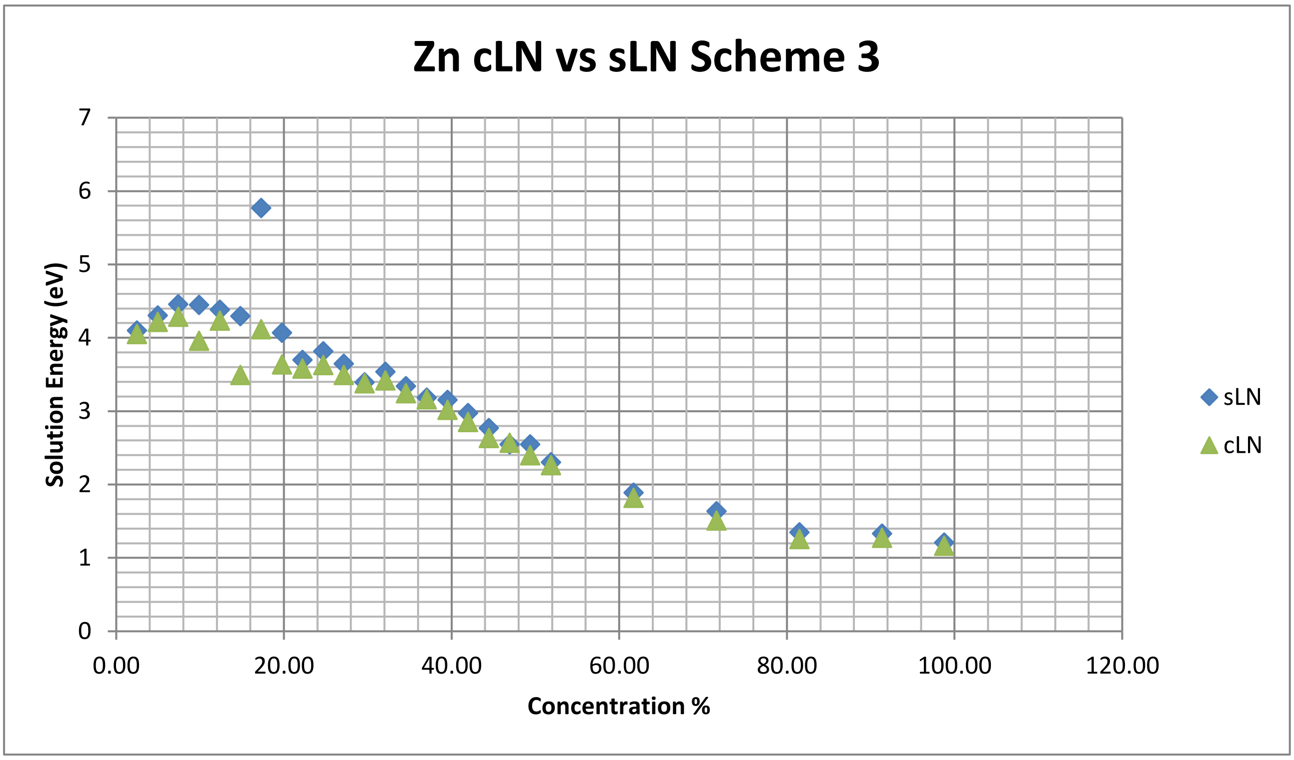

Graph 21 – The solution energies for scheme 3 Zn concentrations from cLN and sLN

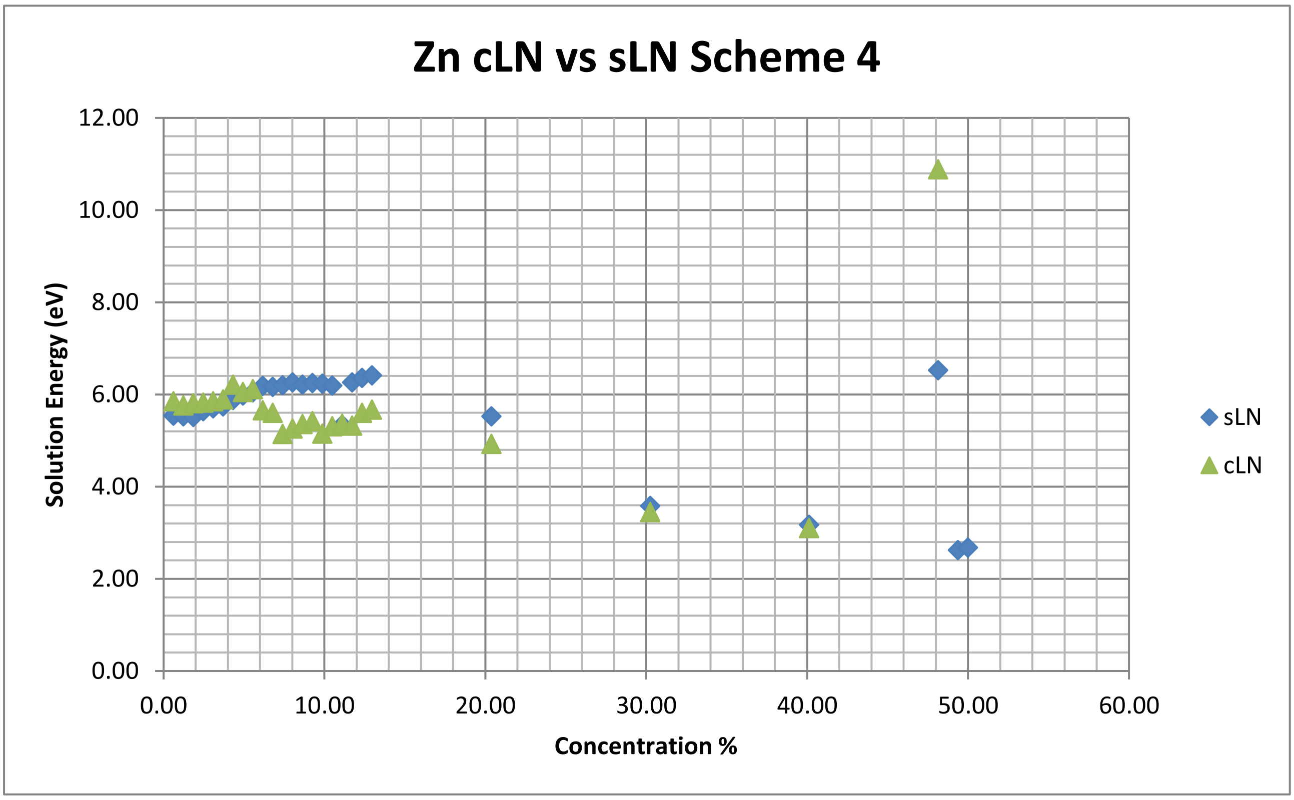

Graph 22 – The solution energies vs concentration for the concentration calculations from each Zn scheme in the congruent super cell

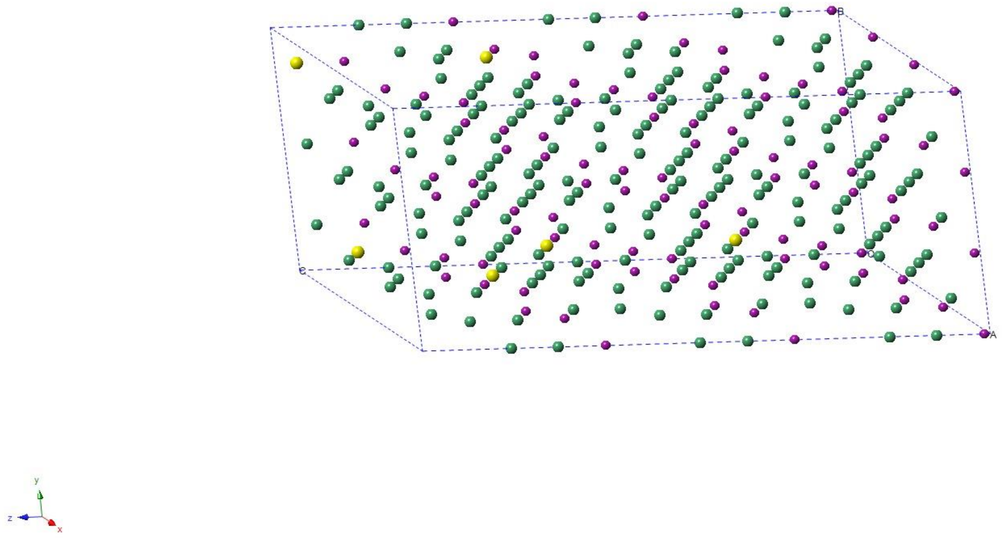

Image 2 – sLN Scheme 4 Zn 48.15% concentration. Li = Yellow, Nb = Green and Zn = Purple, O atoms have been

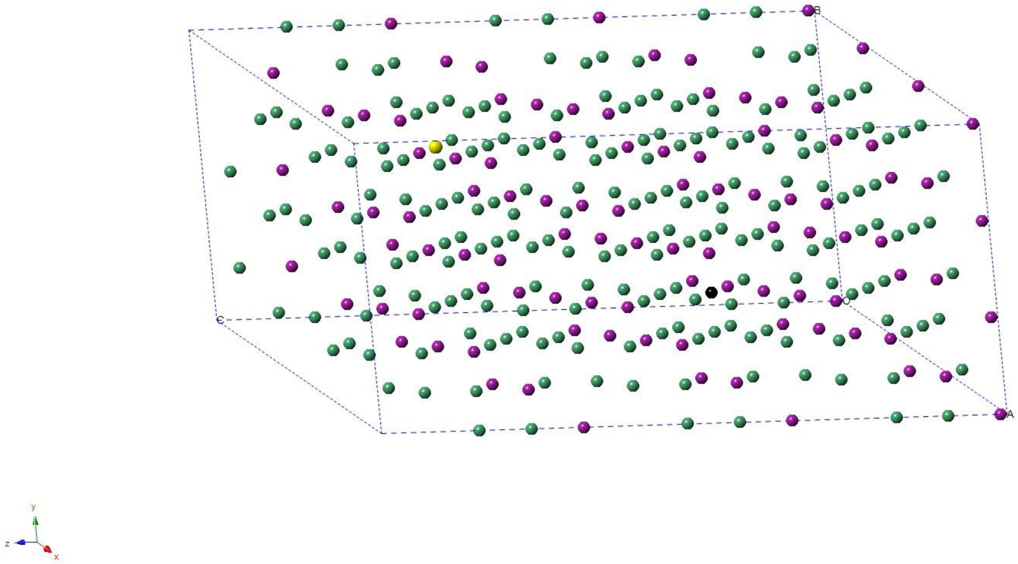

Image 3 – cLN Scheme 4 Zn 48.15% concentration. Li = Yellow, Nb = Green and Zn = Purple, O atoms have been

All the other cLN and sLN schemes for Zn doping mostly match each other. There are some concentrations that could only be done in sLN, as more sites were available after the removal of the intrinsic cLN defects.

Ce Schemes

Below are the schemes for Ce doping in cLN and sLN, Graphs 23-26. Again, agreeing with Araujo et al. (2007)[3], Scheme 2 has the lowest solution energy across all the concentrations with the first solution energy value for cLN in Scheme 2 being lower than that of sLN, 1.83 compared to 2.73 at 0.62% concentration. The solution energy for cLN at 1.23%, however, is not that much lower than the sLN value, different from Scheme 1 for Zn doping where there was a difference in the solution energies initially.

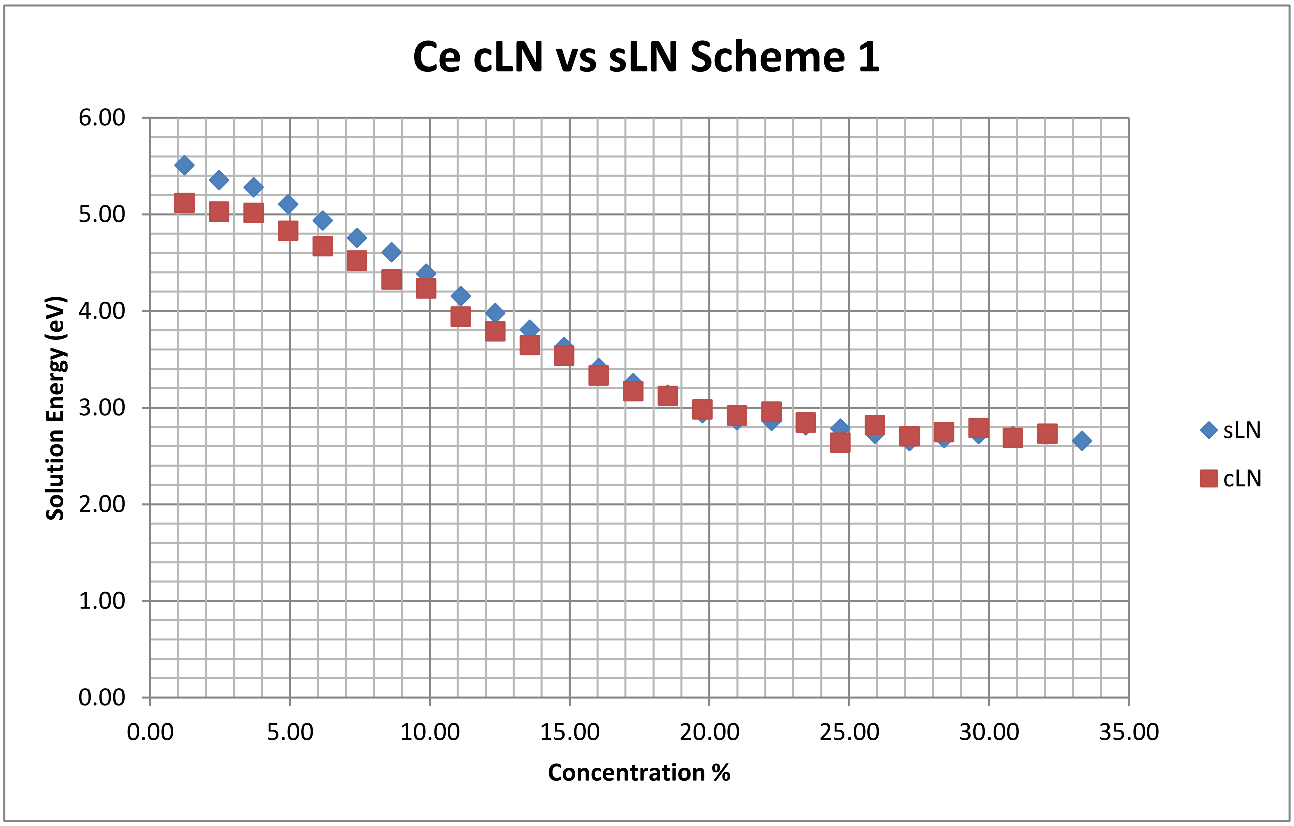

Graph 23 – The solution energies vs concentration for the concentration calculations from scheme 1 in the doping of Ce in the congruent super cell and stoichiometric super cell

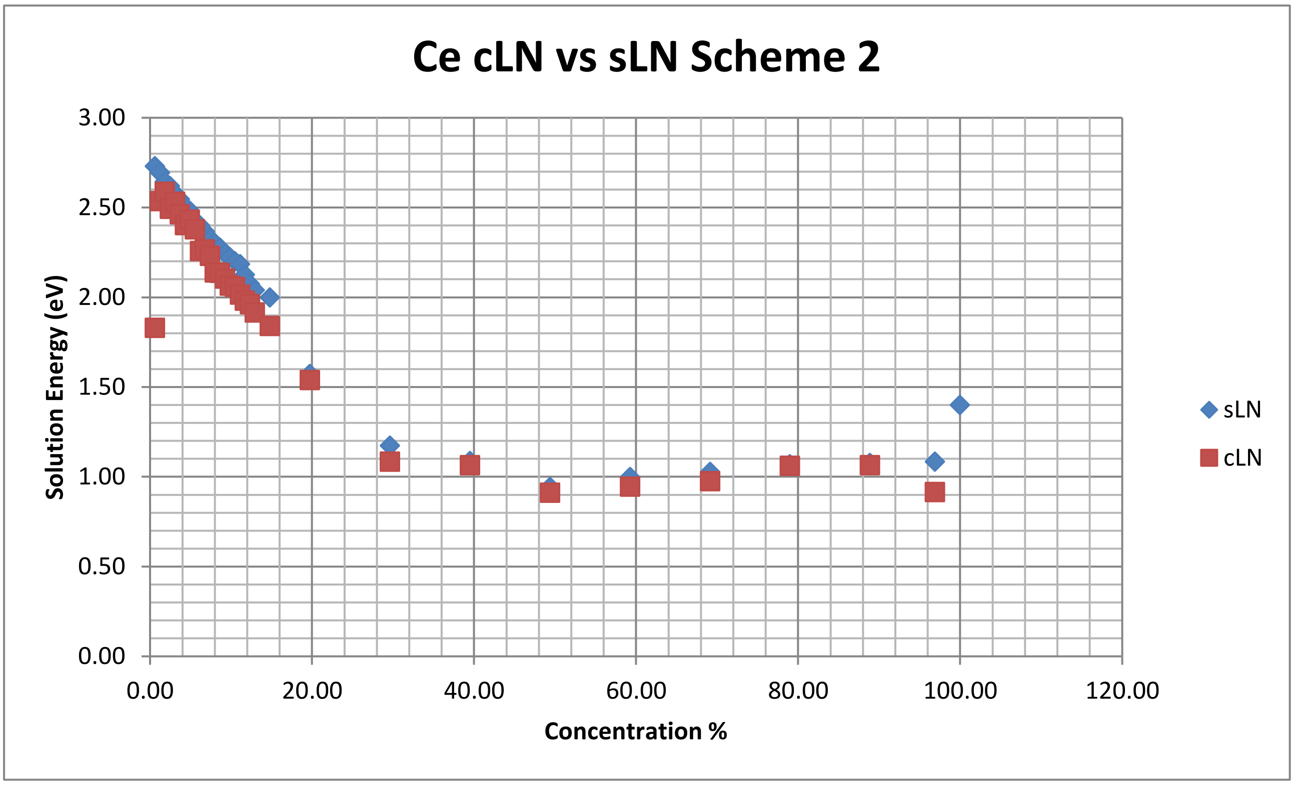

Graph 24– The solution energies vs concentration for the concentration calculations from scheme 2 in the doping of Ce in the congruent super cell and stoichiometric super cell

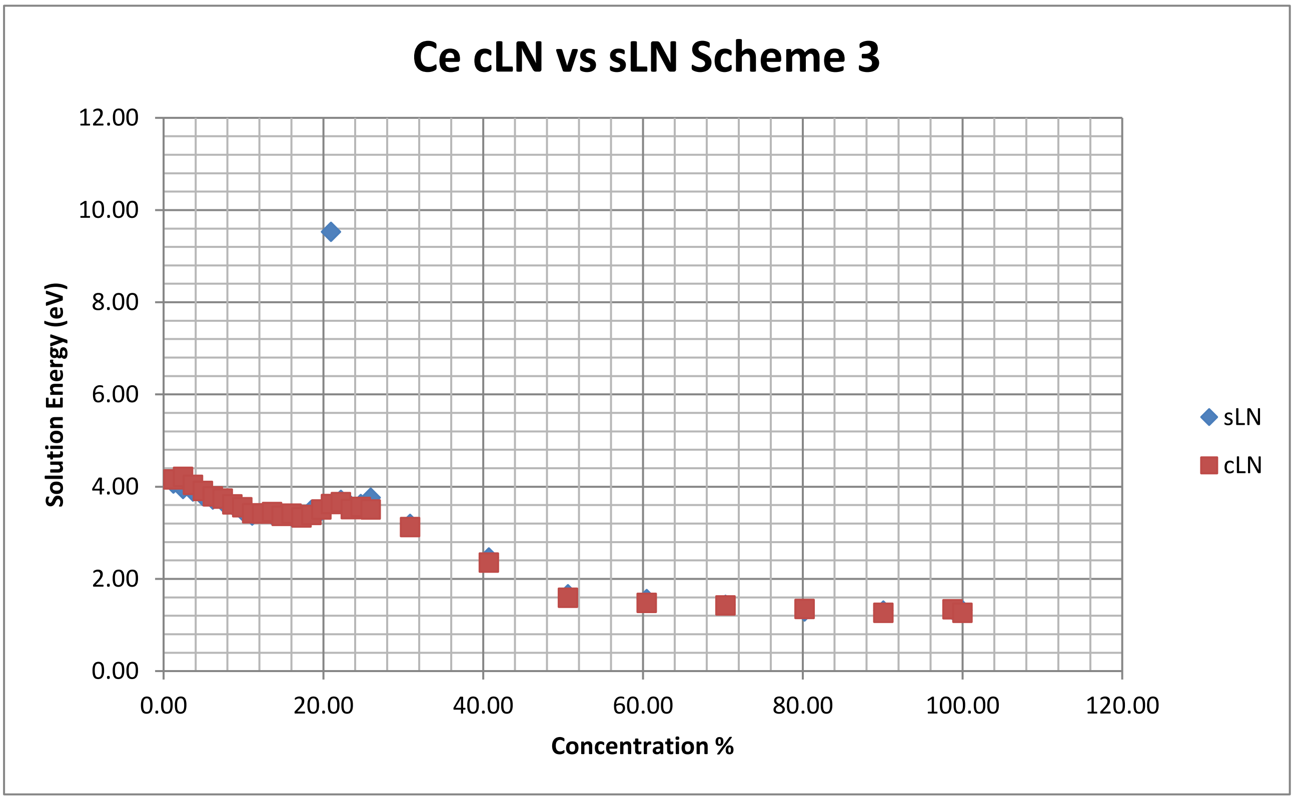

Graph 25 – The solution energies vs concentration for the concentration calculations from scheme 3 in the doping of Ce in the congruent super cell and stoichiometric super cell

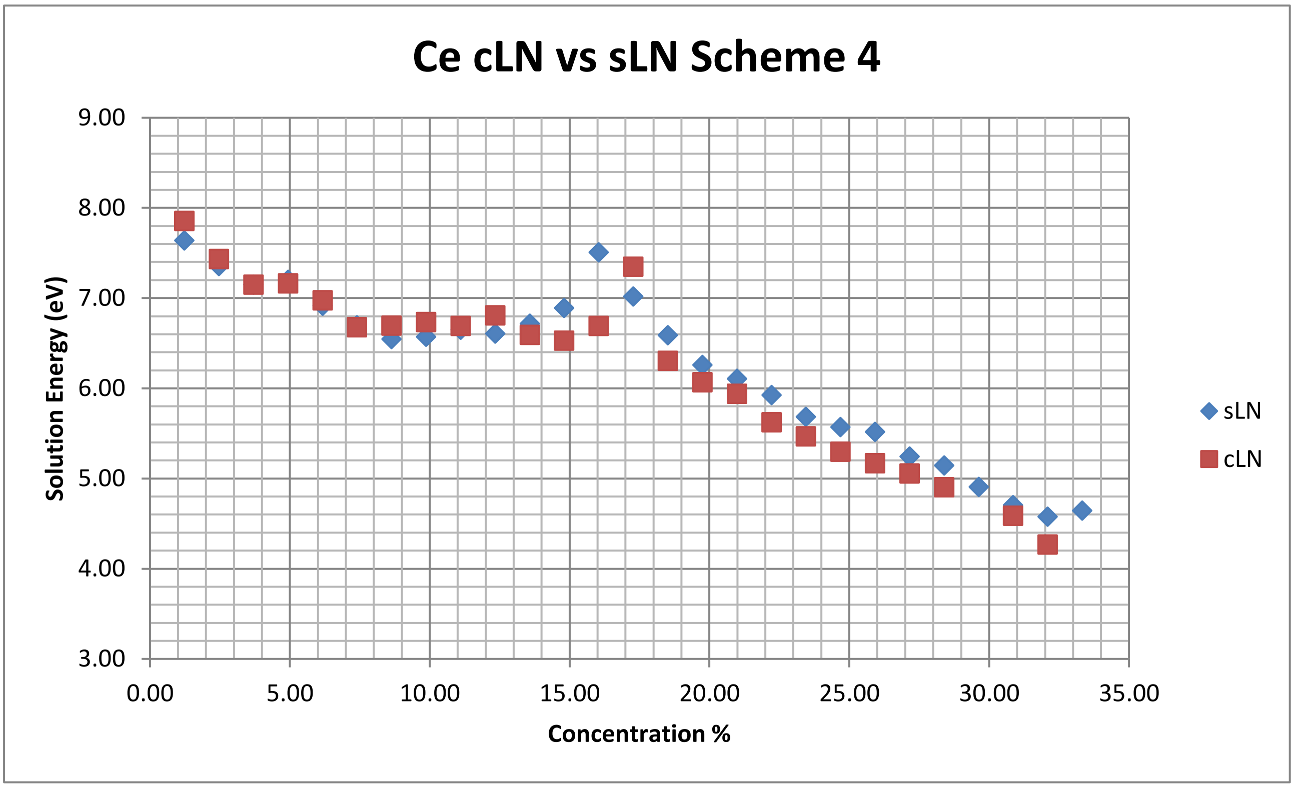

Graph 26 – The solution energies vs concentration for the concentration calculations from scheme 4 in the doping of Ce in the congruent super cell and stoichiometric super cell

The solution energies in the rest of the schemes appear to match each across all the concentrations, apart from the odd anomaly, such as 9.53 at 20.99% in Scheme 3, Graph 25.

In Schemes

The In doping schemes are shown in Graphs 27-30. Scheme 2 has the lowest solution energy across all concentrations. Scheme 2 follows the same pattern as Ce, where the solution energy in Scheme 2 for cLN initially starts below that of sLN and rises to match it from about 1.85% onwards. Scheme 1 also shows a gap between cLN and sLN solution energy values at early concentrations, 4.50 for cLN compared to 4.82 for sLN at 1.23% concentration. However, unlike in previous Scheme 1's the values for cLN stay slightly below throughout the concentrations rather than match those for cLN. Schemes 3 and 4 cLN and sLN results are similar to each other, showing that the intrinsic defects in cLN have little to no effect. They both have high solution energies across all concentrations and are too high to affect the order of doping preference.

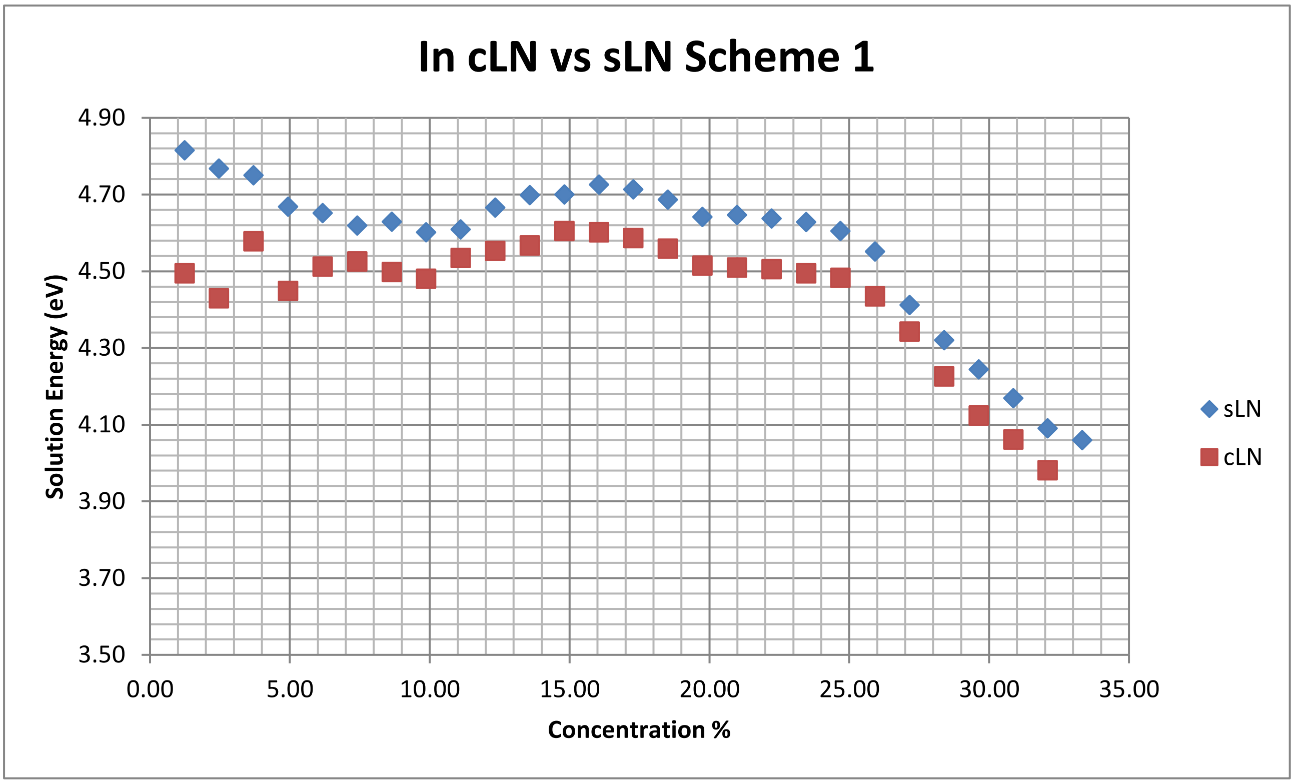

Graph 27 – The solution energies vs concentration for the concentration calculations from scheme 1 in the doping of In in the congruent super cell and stoichiometric super cell

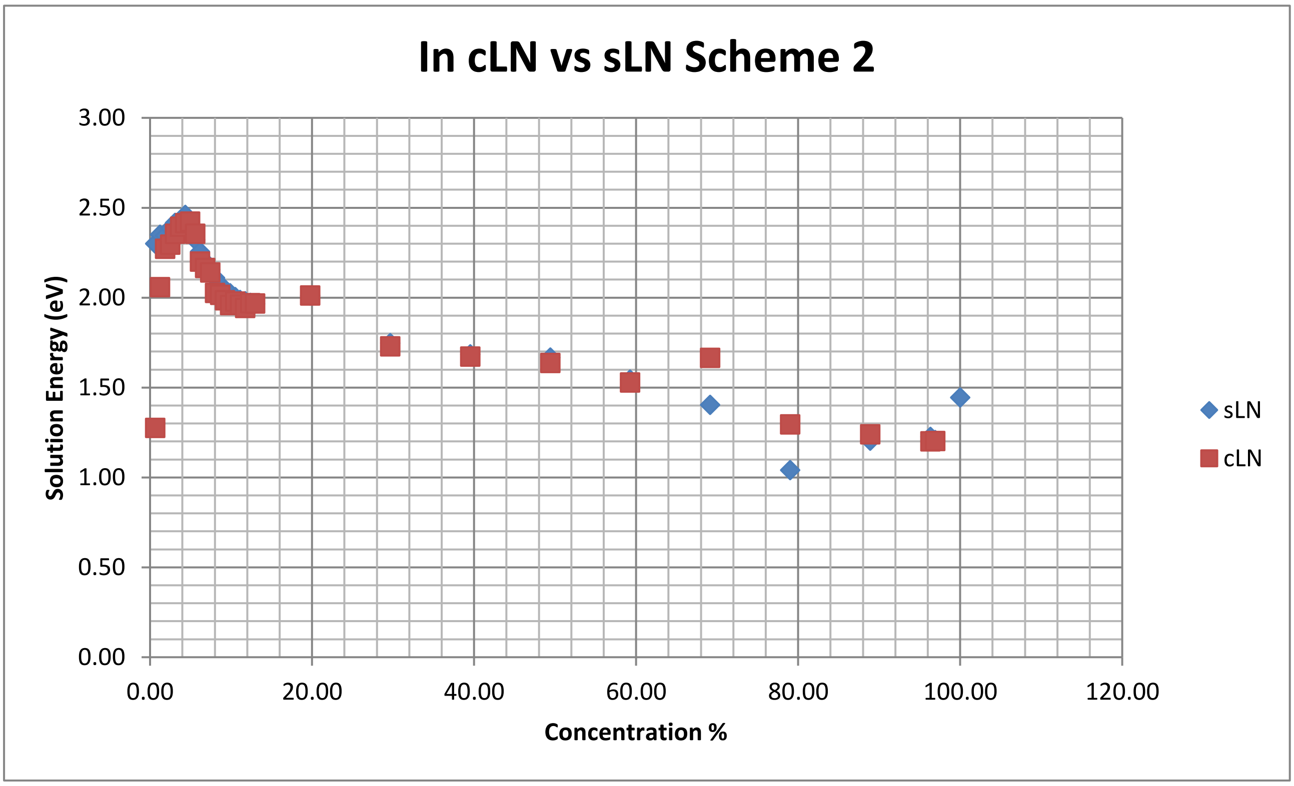

Graph 28 – The solution energies vs concentration for the concentration calculations from scheme 2 in the doping of In in the congruent super cell and stoichiometric super cell

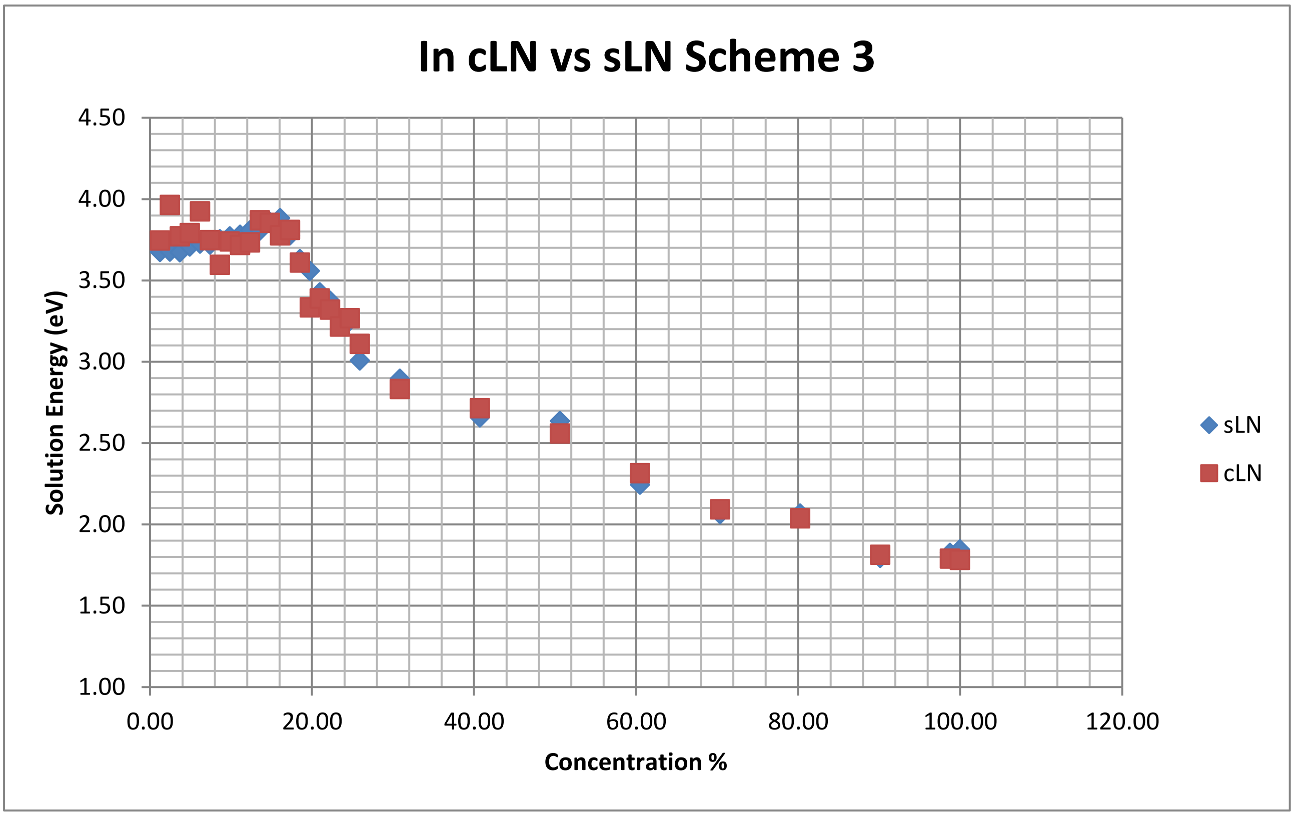

Graph 29 – The solution energies vs concentration for the concentration calculations from scheme 3 in the doping of In in the congruent super cell and stoichiometric super cell

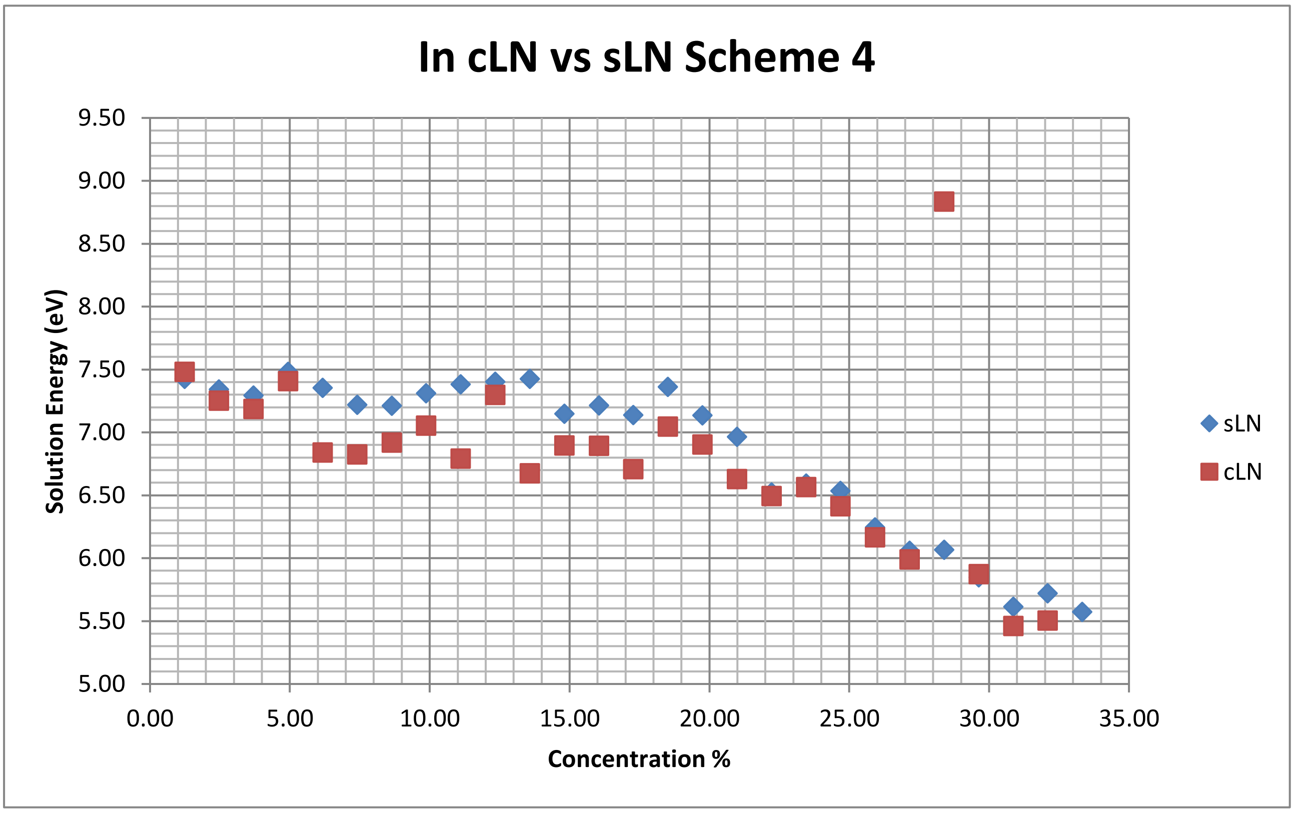

Graph 30 – The solution energies vs concentration for the concentration calculations from scheme 4 in the doping of In in the congruent super cell and stoichiometric super cell

Eu Doping

Eu doping schemes are shown in Graphs 31-34. Again, like with the other trivalent dopants and Zn, Scheme 2 has the lowest solution energies across all the concentrations for both cLN and sLN. Similarly in Scheme 2, cLN has a lower solution energy at its initial value, 0.62% concentration, than that of sLN and rises to match it between 3-13%, where cLN then has a slightly lower solution energy for the rest of the concentrations.

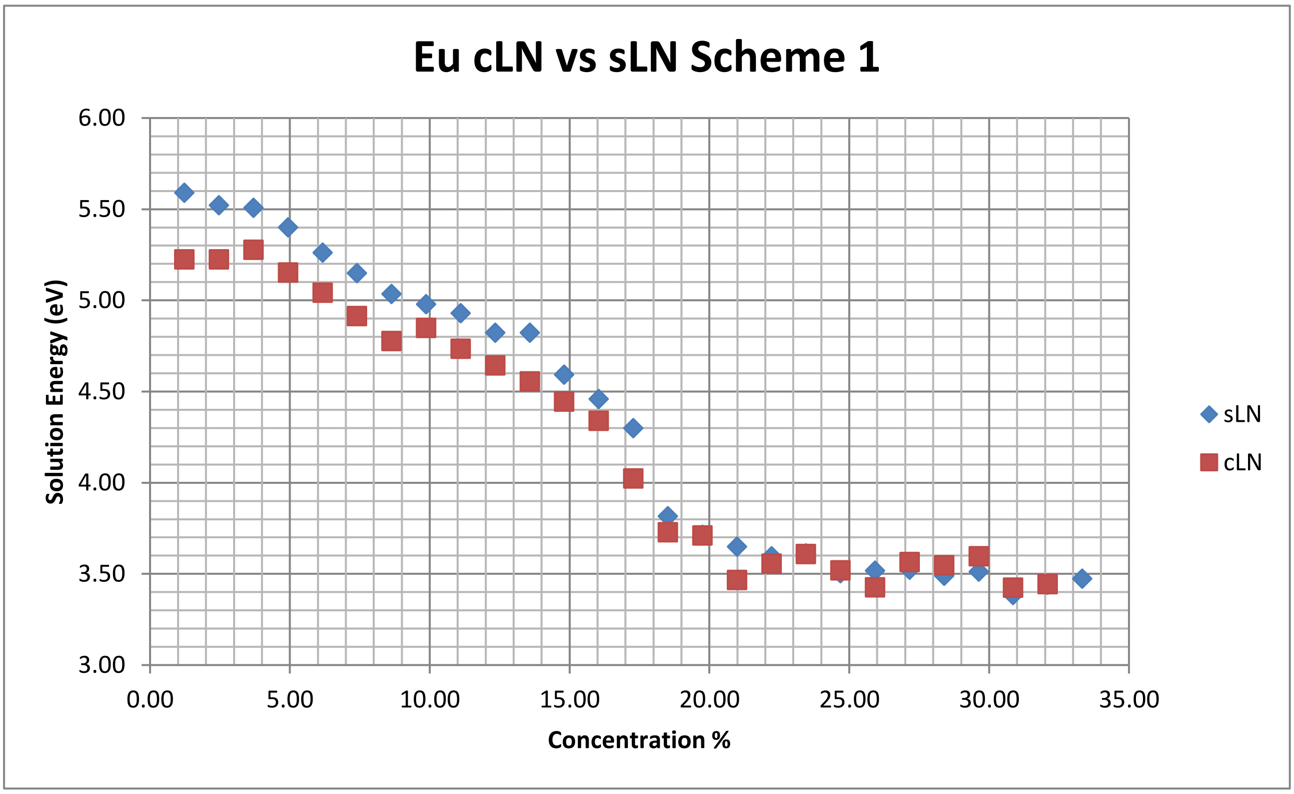

Graph 31 - The solution energies vs concentration for the concentration calculations from scheme 1 in the doping of Eu the congruent super cell and stoichiometric super cell

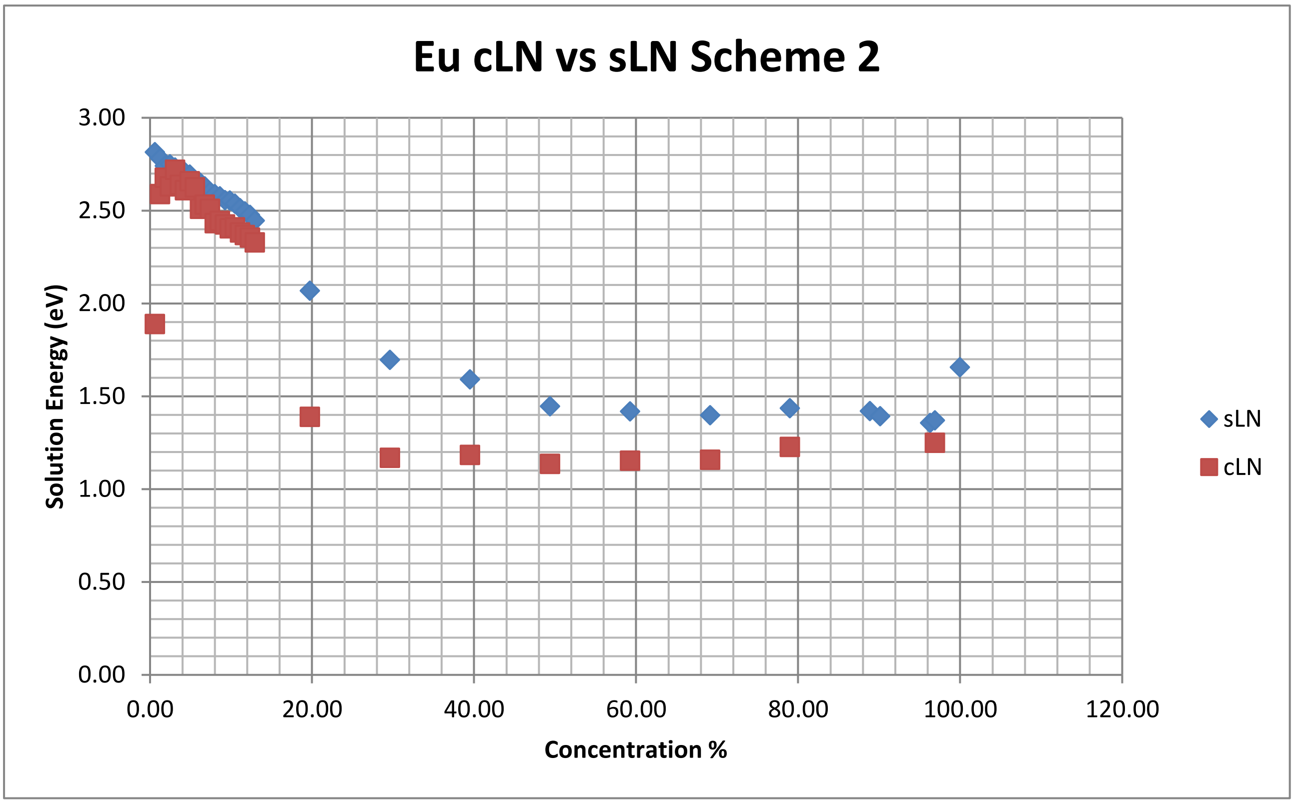

Graph 32 – The solution energies vs concentration for the concentration calculations from scheme 2 in the doping of Eu the congruent super cell and stoichiometric super cell

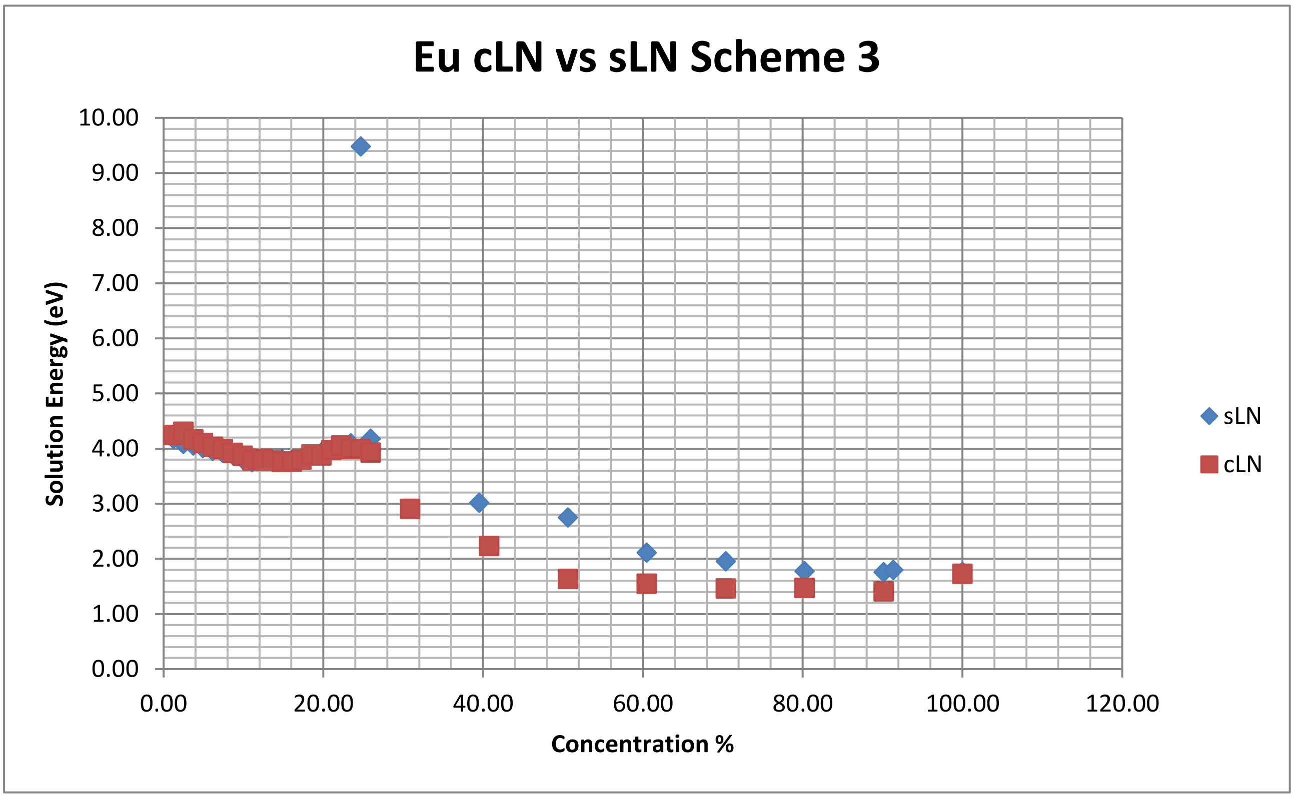

Graph 33 – The solution energies vs concentration for the concentration calculations from scheme 3 in the doping of Eu the congruent super cell and stoichiometric super cell

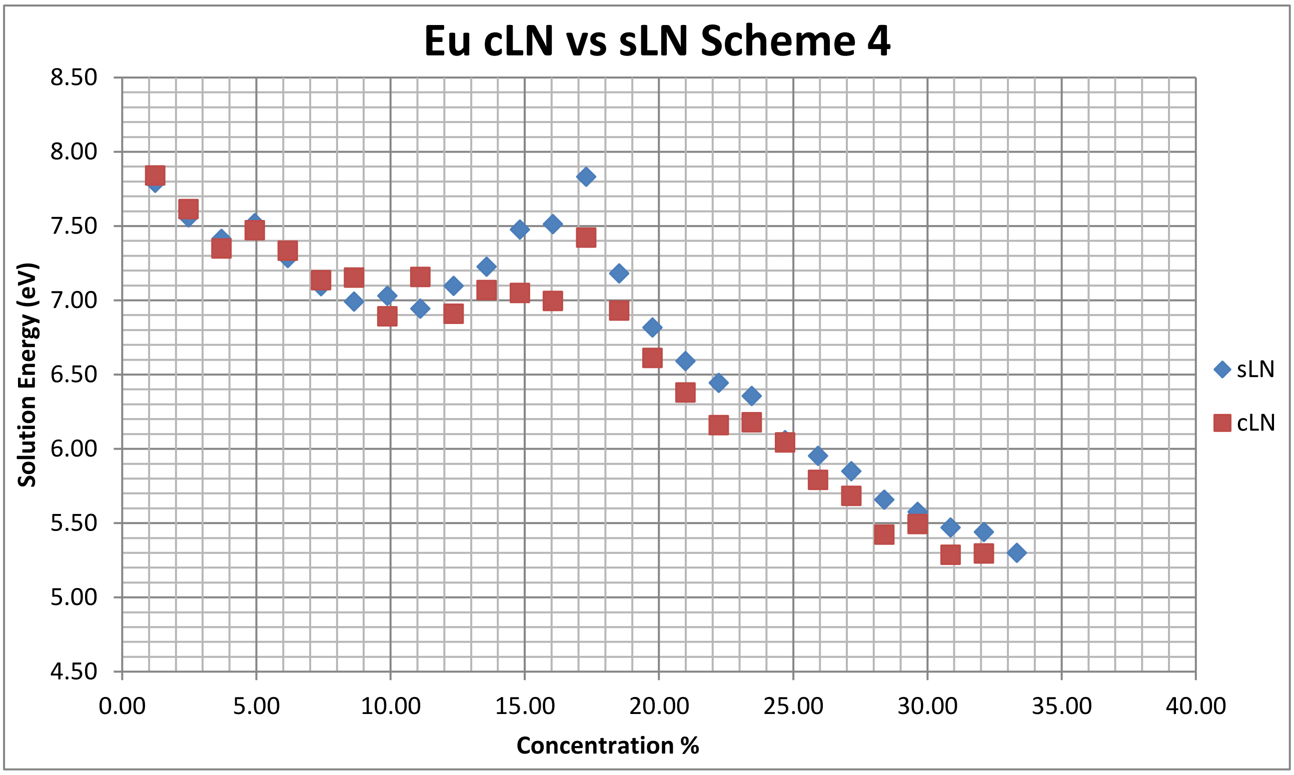

Graph 34 – The solution energies vs concentration for the concentration calculations from scheme 4 in the doping of Eu the congruent super cell and stoichiometric super cell

3.6 Summary

The Zn results shown in the Mott-Littleton calculations and the supercells support the findings in Araujo et al. (2007)[3]. Scheme 2, which was doping at both the Li and Nb site, had the lowest solution energy of all the schemes. This was even the case when the concentrations of the different dopants were altered and their solution energies calculated across each concentration. This suggested preference goes against the preference suggested in Bridges et al. (2016)[6]. In this paper, Bridges et al. (2016)[6] suggests there is minimum doping, around 2-3%, at the Nb site and that most of the doping occurs at the Li site. This is supported in the paper by EXAFS results garnered from Zn doping of $LiNbO_3$. However, Valerio et al. (2016) [5] suggests that through EXAFS simulations that there could indeed be doping at the Nb site. The paper uses data from defect calculations to simulate the EXAFS data and compares them with the results from Bridges et al.(2016) [6].

The results from the doping of the trivalent dopants also support Araujo et al. (2008)[1] as the Scheme preference matches the order suggested in the paper. Scheme 2 had the lowest solution energy for all three dopants and also remained so when concentration was investigated. Scheme 2 was followed by 3, 1 and finally 4. This was different than the preferred scheme of the divalent dopants as shown in Araujo et al. (2007)[3], where the preference was for scheme 2 followed schemes 1, 3 and 4.

Chapter 4 – LiNbO$_3$: Paraelectric Phase

4.1 Background

The paraelectric phase of lithium niobate is discussed here. The structure of LiNbO$_3$ differs in the paraelectric phase compared to the ferroelectric. In the ferroelectric phase, the “Li ions are displaced from the centres” of the triangles formed by O ions and the Nb ions [68]. The Nb ions are also “displaced from the centres of the octahedra” [68]. In the paraelectric phase, however, the Li ions are located at the centre of the triangles, with the Nb ions being located at the centres of the octahedra [68].

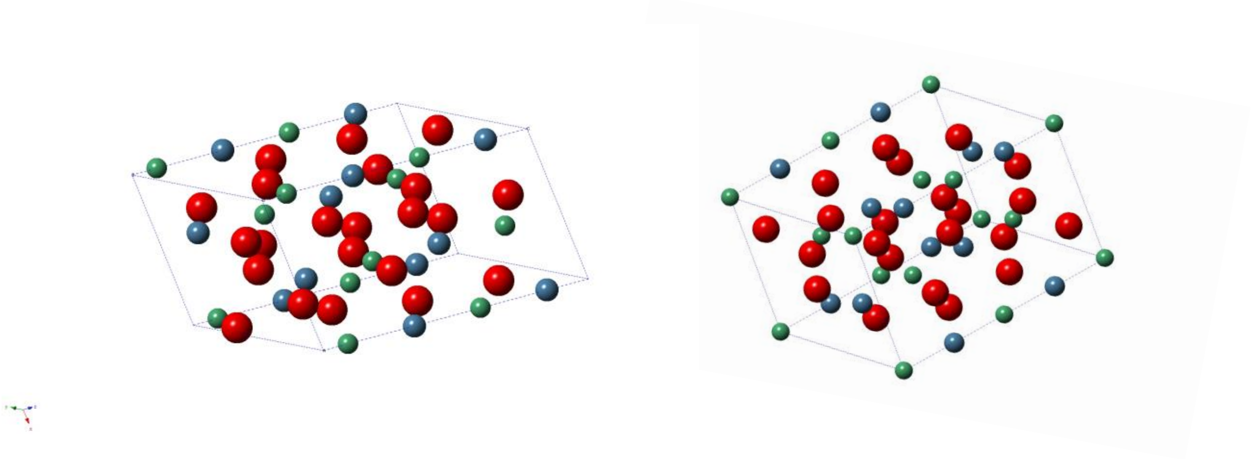

Image 4 – Left is the Mott-Littleton structure and on the right is the paraelectric structure. Li = Blue, Nb = Green and O = Red

The Curie temperature, T$_c$, is the temperature at which the ferroelectric phase transitions into the paraelectric phase [68]. Point defects effect the value of T$_c$, with the concentration of the defects being “primarily determined by the extent of doping or by the Li/Nb ratio”, particularly the quantity of Nb$_{Li}$ [68]. Divalent and trivalent dopants were found to increase the value of T$_c$, but tetravalent dopants decreased T$_c$ [68]. Divalent and trivalent dopants increase the amount of Nb$_{Li}$, which is the reason for the increase in the value of T$_c$ [30].

The phase transition from ferroelectric to paraelectric was modelled by Sanna and Schmidt (2012) [69]. This investigation used molecular dynamics (MD) simulations “to model the transition” and “understand the mechanisms of the transitions itself” [69]. VASP was used to implement the all-electron projector-augmented wave (PAW) method, with a Monkhorst-Pack (MP) 6x6x6 mesh used to “carry out the integration in the Brillouin zone for the simulation of the crystal structure” [69]. A supercell, consisting of a 2x2x2 repetition of the unit cell and 2x2x2 MP k-point mesh, was also used to perform the molecular dynamics calculations [69]. The results of Sana and Schmidt (2012) [69] suggested that the “paraelectric phase must be thought of as a random distribution of Li ions above and below the oxygen planes (with a nonzero value of ΔLi for most Li ions) and with an average zero net polarization, rather than in the commonly accepted configuration” [69].

Jackson and Valerio (2005) [4] developed a new interatomic potential for the ferroelectric and paraelectric phases of $LiNbO_3$ [4]. The new potential was created as new data had become available since the original potential was published, so a new potential was required that reproduced the findings from the data, with the main motivation behind creating this new potential being “able to model the full range of intrinsic and extrinsic defects that control most of the important properties of this material” [4].

The results gathered from the Mott-Littleton calculations of the paraelectric phase of $LiNbO_3$ will now be discussed in this chapter. The results will be compared to the previous Mott-Littleton calculations done on stoichiometric $LiNbO_3$, to analyse any changes in the preference of the doping schemes and if any changes occur to the solution energies of the dopants themselves.

4.2 Results

The first results gathered were the intrinsic defects, consisting of vacancies and interstitials; Table 17 below shows these results compared to those gathered from the sLN Mott-Littleton calculations.

Defect	Paraelectric Energy (eV)	sLN Energy (eV)
Li Vacancy	9.68	9.69
Nb Vacancy	123.87	123.93
O Vacancy	20.38	20.38
Li Interstitial	-7.72	-7.73
Nb Interstitial	-105.40	-106.60
O interstitial	-11.98	-12.88

Table 17 – Paraelectric and stoichiometric energies (eV) for the basic defects

The results are extremely similar to the other Mott-Littleton results. This suggests the paraelectric phase has no effect on the energy of the basic defects.

Multiple dopant calculations were then done using the same divalent and trivalent dopants as used in the previous Mott-Littleton structure. Tables 18 and 19 below show the results from the paraelectric phase and the results from the stoichiometric form of $LiNbO_3$.

	Paraelectric				Stoichiometric			
M	**Scheme 1**	**Scheme 2**	**Scheme 3**	**Scheme 4**	**Scheme 1**	**Scheme 2**	**Scheme 3**	**Scheme 4**
Zn	2.27	1.70	8.44	11.26	2.52	1.73	11.49	15.53
Mg	2.36	1.77	8.45	11.27	2.62	1.81	11.50	15.54
Mn	2.35	1.77	8.48	11.30	2.60	1.81	11.56	15.60
Fe	2.29	1.71	8.44	11.26	2.54	1.75	11.50	15.54
Co	2.28	1.70	8.43	11.25	2.44	1.67	11.49	15.53
Ni	2.49	1.86	8.46	11.28	2.75	1.91	11.52	15.56
Sr	3.80	3.16	9.72	12.54	4.06	3.21	12.78	16.82
Cd	2.70	2.09	8.74	11.56	2.96	2.25	12.23	16.27
Ba	6.28	5.42	11.31	14.13	6.53	5.46	14.37	18.41
Pb	1.53	0.93	7.60	10.42	1.76	0.95	10.66	14.70
Zn	2.27	1.70	8.44	11.26	2.52	1.73	11.49	15.53
Mg	2.36	1.77	8.45	11.27	2.62	1.81	11.50	15.54
Mn	2.35	1.77	8.48	11.30	2.60	1.81	11.56	15.60

Table 18 – Paraelectric and stoichiometric solution energies (eV) for the divalent dopants

	Paraelectric				Stoichiometric			
M	**Scheme 1**	**Scheme 2**	**Scheme 3**	**Scheme 4**	**Scheme 1**	**Scheme 2**	**Scheme 3**	**Scheme 4**
Ce	5.81	3.10	6.03	11.67	6.19	3.05	8.00	16.08
Pr	5.73	2.97	5.86	11.50	6.11	2.93	7.83	15.91
Nd	5.26	2.48	5.35	11.00	5.64	2.44	7.32	15.41
Sm	5.96	3.21	6.10	11.75	6.33	3.16	8.07	16.16
Eu	5.86	3.12	6.03	11.68	6.24	3.08	8.00	16.09
Gd	5.77	3.05	5.98	11.62	6.15	3.01	7.95	16.03
Tb	5.80	3.05	5.94	11.59	6.18	3.00	7.91	16.00
Dy	5.49	2.78	5.72	11.36	5.87	2.74	7.69	15.77
Ho	5.60	2.90	5.84	11.49	5.97	2.85	7.80	15.89
Er	5.53	2.83	5.77	11.42	5.91	2.79	7.74	15.83
Tm	5.48	2.78	5.73	11.38	5.86	2.74	7.70	15.79
Yb	5.47	2.78	5.73	11.37	5.85	2.73	7.70	15.78
Lu	5.43	2.74	5.70	11.34	5.82	2.70	7.67	15.75

Table 19 – Paraelectric and stoichiometric solution energies (eV) for the trivalent dopants

Again, these results are similar to one another. The order of preferences for the paraelectric phase is again scheme 2, being the most preferred, followed by scheme 1, 3 and finally 4.

Divalent

Graphs 35-38 below shows the solution energies of the divalent dopant scheme 1 in the paraelectric phase compared to that of the stoichiometric form and those gathered from Araujo et al (2007) [3], with Table 20 showing the ionic radii of each divalent dopant.

Dopant	Ionic Radii (ρm)
Zn	0.74
Mg	0.72
Mn	0.67
Fe	0.61
Co	0.65
Ni	0.69
Sr	1.18
Cd	0.95
Ba	1.35
Pb	1.19

Table 20 – Ionic radii for the divalent dopants from *Shannon(1976)* [67]

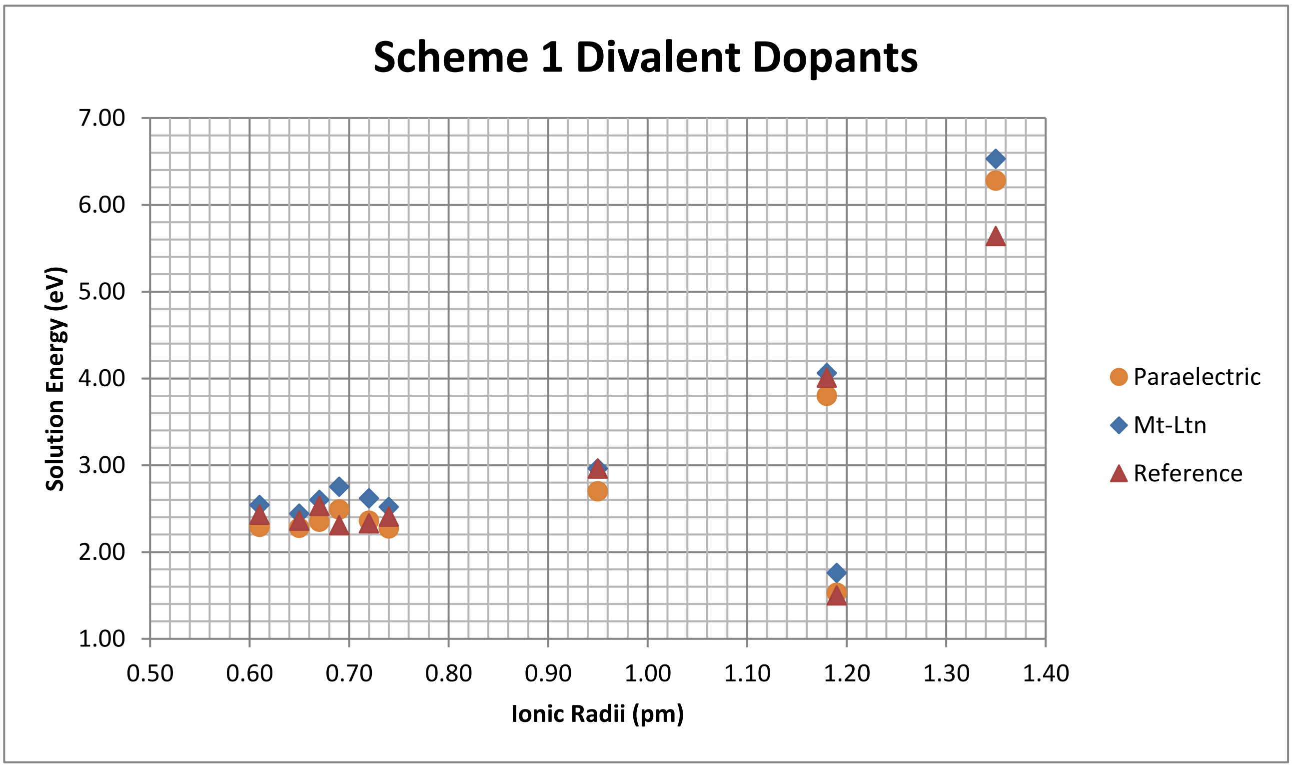

Graph 35 – Comparison of scheme 1 divalent dopants in the paraelectric phase, the stoichiometric form and values from Araujo et al (2007)[3]

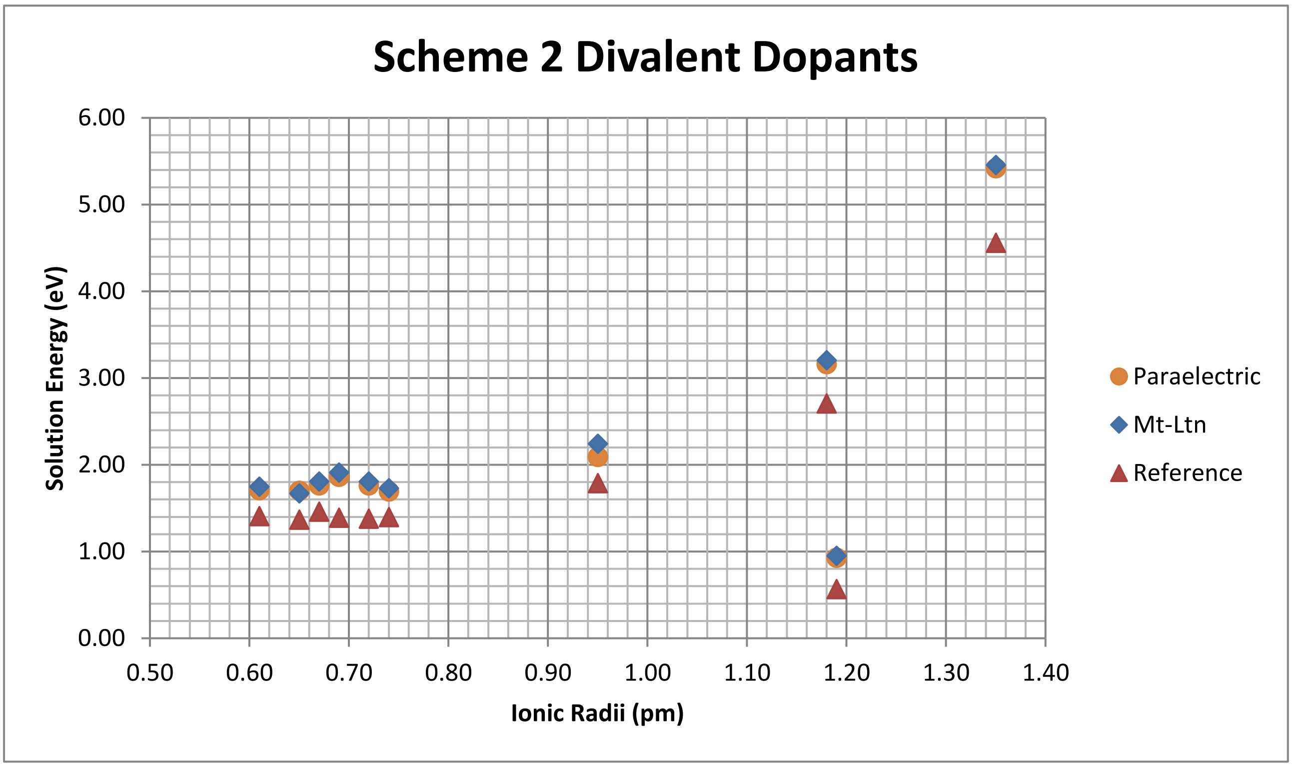

Graph 36 – Comparison of scheme 2 divalent dopants in the paraelectric phase, the stoichiometric form and values from Araujo et al (2007)[3]

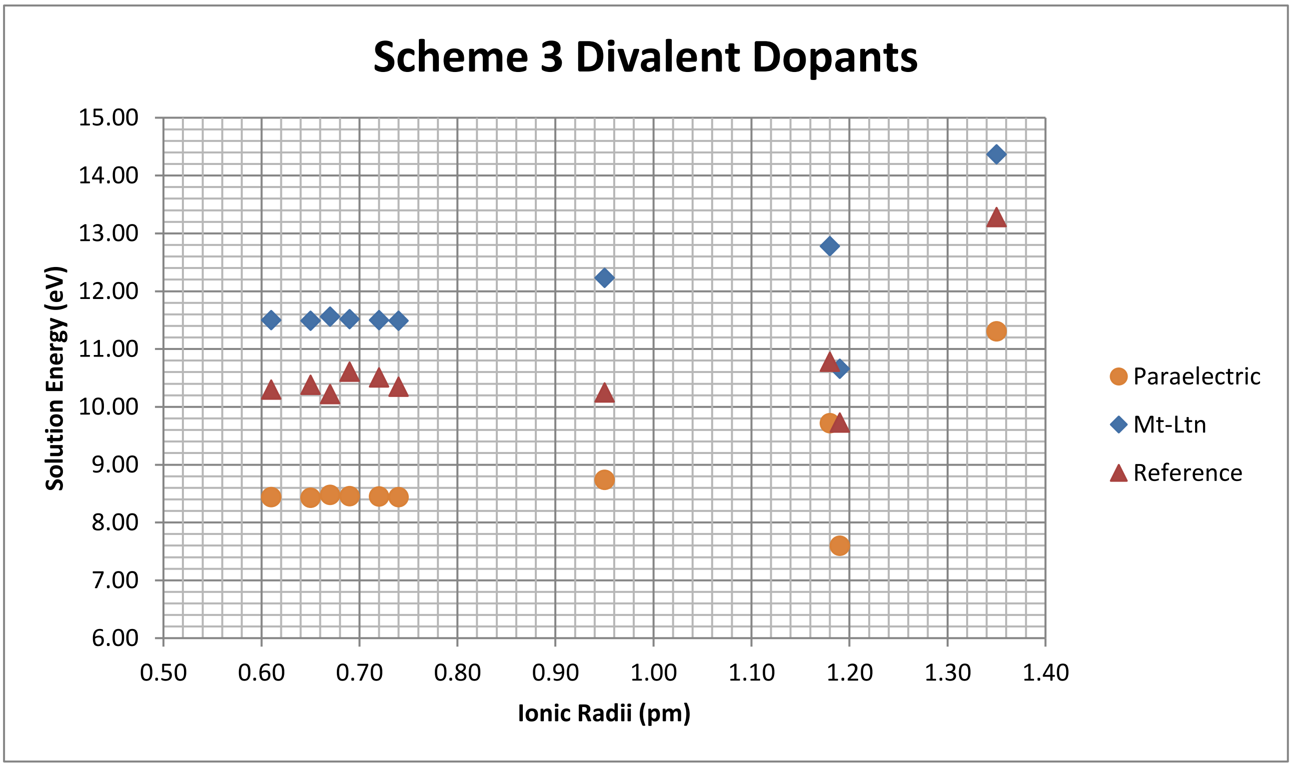

Graph 37 – Comparison of scheme 3 divalent dopants in the paraelectric phase, the stoichiometric form and values from Araujo et al (2007)[3]

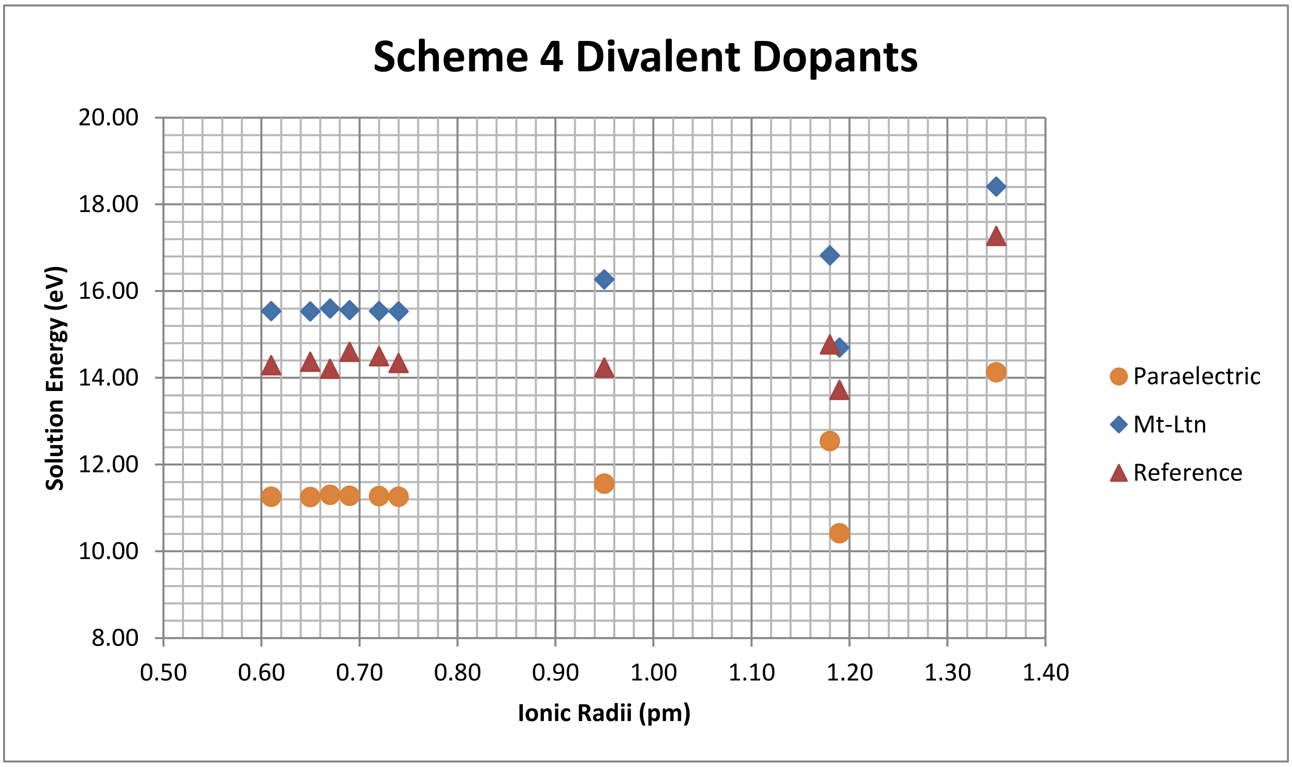

Graph 38 – Comparison of scheme 4 divalent dopants in the paraelectric phase, the stoichiometric form and values from Araujo et al (2007)[3]

The values for the paraelectric appear similar to that of the stoichiometric values. However, the only difference is that the paraelectric results appear to have slightly lower solution energy across all the dopants. This would be significant if this resulted in the solution energy being lower the solution energy of the dopants respective solution energy for scheme 2. Solution energy increases with ionic radii, except for Pb where it is lower than possibly predicted.

The paraelectric results are generally lower than the reference data gathered from Araujo et al. (2007), apart from in Scheme 1, which has slightly higher solution energies. The dopant with the lowest solution energy is Pb in both the reference and paraelectric data.

Trivalent

Below in Graphs 39-42, the solution energies for trivalent dopants in the paraelectric phase are compared to those of the stoichiometric form and those gathered from Araujo et al (2007) [3]. Table 21 shows the ionic radii of the trivalent dopants.

Dopant	Ionic Radii (pm)
Ce	1.01
Pr	0.99
Nd	0.98
Sm	0.96
Eu	0.95
Gd	0.94
Tb	0.92
Dy	0.91
Ho	0.90
Er	0.89
Tm	0.88
Yb	0.87
Lu	0.86

Table 21 – Ionic radii for the trivalent dopants from Shannon(1976) [67]

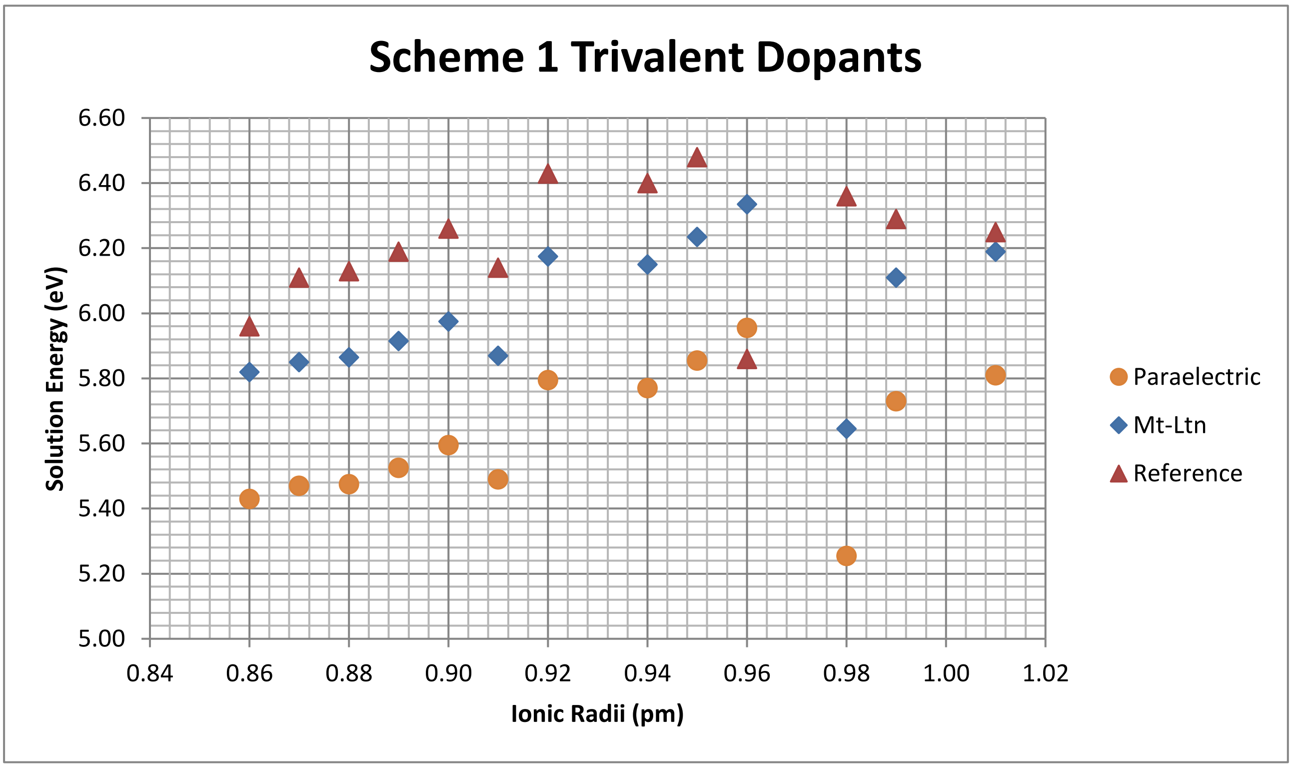

Graph 39 – Comparison of scheme 1 trivalent dopants in the paraelectric phase, stoichiometric form and values from Araujo et al (2007)[3]

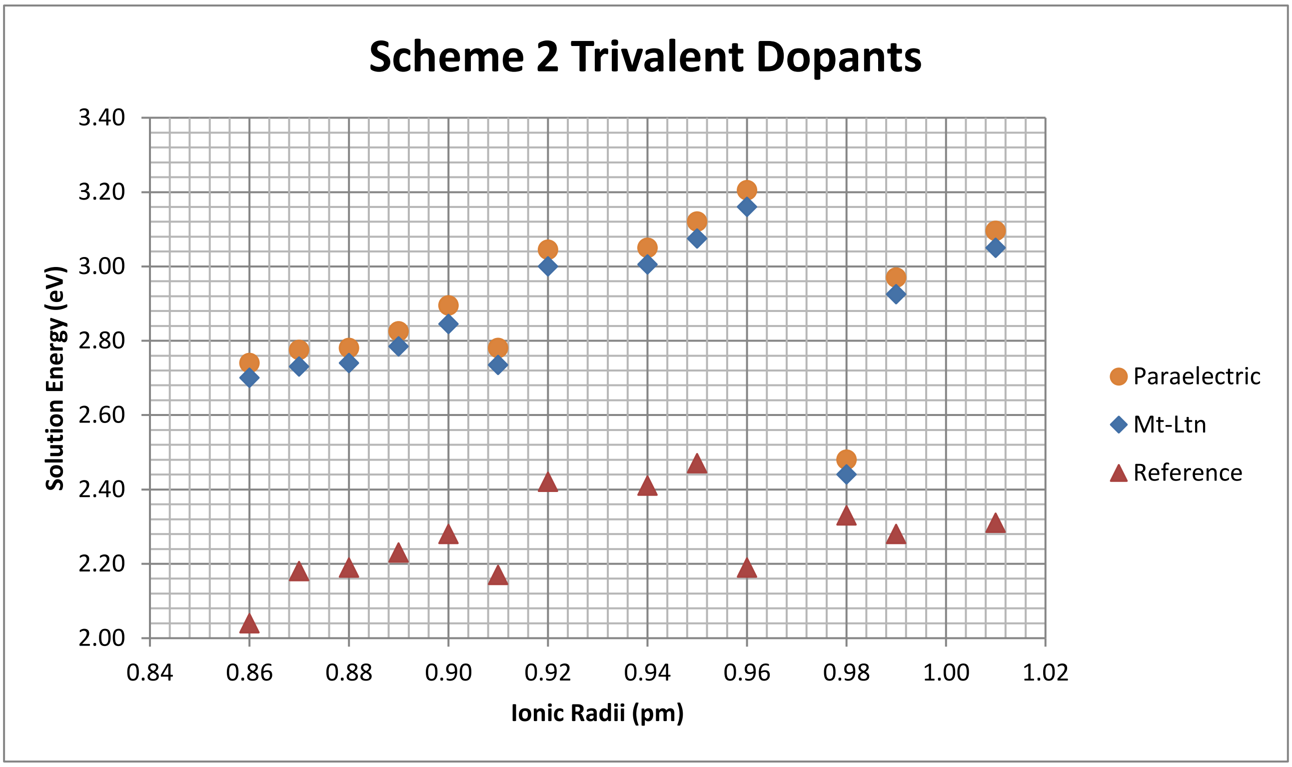

Graph 40 – Comparison of scheme 2 trivalent dopants in the paraelectric phase, stoichiometric form and values from Araujo et al (2007)[3]

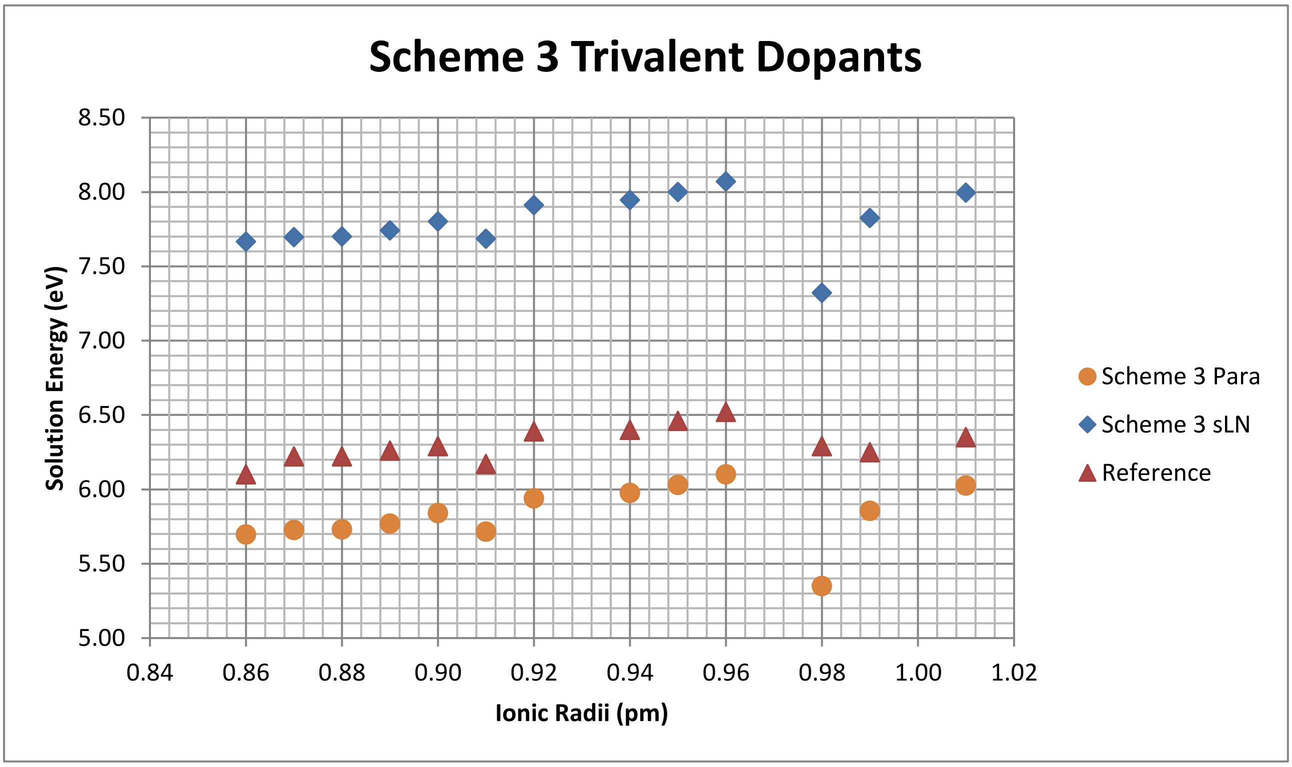

Graph 41 – Comparison of scheme 3 trivalent dopants in the paraelectric phase, stoichiometric form and values from Araujo et al (2007)[3]

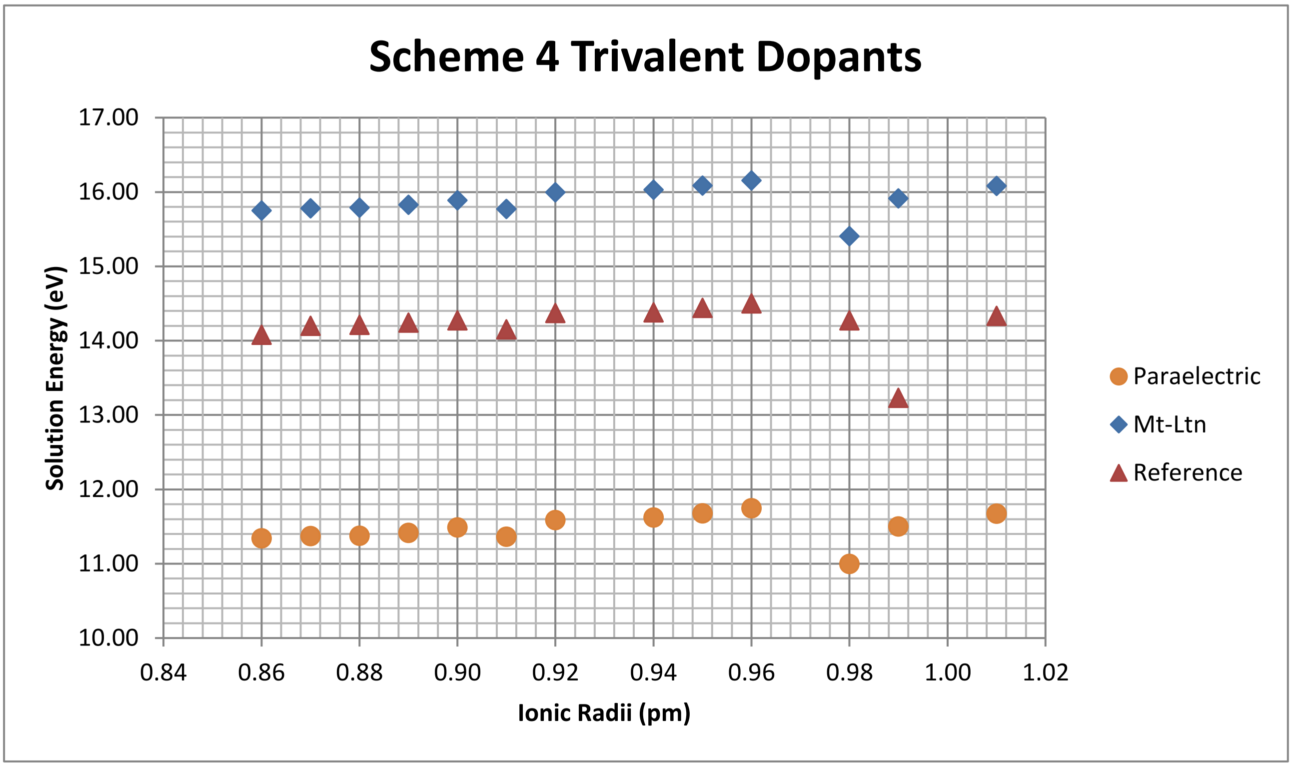

Graph 42 – Comparison of scheme 4 trivalent dopants in the paraelectric phase, stoichiometric form and values from Araujo et al (2007)[3]

The results again show that across all the dopants, scheme 2 has the lowest solution energy of the schemes. The paraelectric results do not differ massively from the stoichiometric values in scheme 2. However, in schemes 1, 3 and 4, the values for the paraelectric values are noticeably lower. The solution energies for schemes 1 and 3 in the paraelectric phase are also closer together than in the stoichiometric form. However, the solution energies for scheme 3 never become low enough to change the preference of the schemes. Generally, solution energy increases as ionic radii increases, however Dy and Nd are both lower than the trend predicts.

The paraelectric results are lower than those gathered from Araujo et al. (2007) in schemes 1, 3 and 4, however in scheme 2 they are significantly larger than the solution energies in Araujo et al. (2007). Sm in both the paraelectric and stoichiometric data sets has a higher solution energy than the reference value in scheme 2. In the scheme 1 also, Sm from the reference results appears much lower than predicted, as the Sm solution energy in scheme 1 from the paraelectric phase and stoichiometric form increases from its previous result. Nd also appears to break the pattern, as in the paraelectric and stoichiometric data it is lower than the reference value suggests it should be.

Chapter 5 - Conclusions

This paper confirms doping is done at the Nb site as well as the Li site, just like is shown in previous computational investigations. The investigation of doping in $LiNbO_3$ has been done a scale not done before, with two supercell calculations being done as well as a paraelectric phase. The aims of this investigation have been met, with the concentration of the dopants being shown to have no effect on the scheme preference.

For future investigations, further modelling should be done on a bigger supercell, focusing on low concentrations, specifically in the range 0-1%. This is because this showed the greatest difference between cLN and sLN when the different compared dopant concentrations from each Scheme were compared. The inclusion of dopants with a variety of more ion sizes could also be researched; to obtain a wider view of the effect ion size has on solution energies and site preference. Also, the location of the defects in the congruent phase could be analysed using CrystalMaker to ascertain any commonalities in the dopant schemes, with some obtaining anomalous results when compared to other results.

References

[1] Araujo R., Valerio M., Jackson R. ,Computer modelling of trivalent metal dopants in lithium niobate. ,*J. Phys. Condens. Matter*. ,2008, **20**, 1-3.

[2] Araujo. R., Valerio M., Jackson R., Computer simulation of metal co-doping in lithium niobate, *Proc. R. Soc. A.*, 2014, **470**, 1–9

[3] Araujo. R., Lengyel. K., Jackson. R., Kovacs. L., Valerio. M., A computational study of intrinsic and extrinsic defects in $LiNbO_3$, *J Physics-Condensed Matter*, 2007, **19**, 1-10

[4] Jackson. R., Valerio. M., A new interatomic potential for the ferroelectric and paraelectric phases of $LiNbO_3$, *J. Phys. Condens. Matter.*, 2005, **17**, 837–843

[5] Jackson. R., Valerio. M., Bridges. F., EXAFS simulations in Zn-doped $LiNbO_3$ based on defect calculations, *IOP Conf. Series: Materials Science and Engineering*, 2017, **169**, 1-5

[6] Bridges. F., Mackeen. C., Kovàcs. L., No difference in local structure about a Zn dopant for congruent and stoichiometric $LiNbO_3$, *Phys. Rev. B.*, 2016, **94**, 1-5

[7] Bridges. F., Castillo-Torres J., Car. B., Medling. S., Kozina. M., EXAFS evidence for a primary Zn_{Li} dopant in $LiNbO_3$, *Phys. Rev. B.*, 2012, **85**, 1-12

[8] Jensen. F, *Introduction to Computational Chemistry*, Second Edition, Chichester: Wiley, 2007

[9] Gale. J., Rohl. A., The General Utility Lattice Program (GULP), *Mol Simul.*, 2003, **29**(5):291–341

[10] Henson. N., Cheetham. A., Gale. J., Theoretical Calculations on Silica Frameworks and Their Correlation with Experiment, *Chem. Mater.*, 1994, **6**, 1647–1650

[11] Gale. J., Wilson. K., Sellgren. A., GULP: A computer program for the symmetry-adapted simulation of solids, *J. Chem. Soc., Faraday Trans.*, 1997, **93**(4), 629–637

[12] Bush. T., Catlow. C., Battle. P., Evolutionary Programming Tecniques for predicting Inorganic Crystal Structures, *J. Mater. Chem.*, 1995, **5**(8), 1269–1272

[13] Cope. E., Dove. M., Pair distribution functions calculated from interatomic potential models using the General Utility Lattice Program, *J. Appl. Cryst.*, 2007, **40**, 589–594

[14] Gale. J., Raiteri. P., van Duin. A., A reactive force field for aqueous-calcium carbonate systems, *Phys. Chem. Chem. Phys.*, 2011, **13**, 16666–16679

[15] Gale. J., Rohl. A., An efficient technique for the prediction of solvent-dependent morphology: the COSMIC method, *Mol. Simul.*, 2007, **33**(15), 1237–1246.

[16] Güler. E., Güler. M., Elastic and mechanical properties of hexagonal diamond under pressure, *Appl. Phys. A.*, 2015, **119**, 721-726

[17] McSloy. A., Kelly. P., Slater. P., Panchmatia. P., A computational study of doped olivine structured Cd_2GeO_4: local defect trapping of interstitial oxide ions, *Phys. Chem. Chem. Phys*., 2016, **18**, 26284–26290.

[18] Ewald P., The calculation of optical and electrostatic grid potential, *Ann. Phys*., 1921, **64**, 253.

[19] Jackson. R., Catlow. C., Computer Simulation Studies of Zeolite Structure, *Mol. Simul*., 1988, **1**, 207–224

[20] Banerjee. A., Adams. N., Simons. J., Shepard. R., Search for stationary points on surfaces, *J. Phys. Chem.*, 1985, **89**, 52–7

[21] Mott N., Littleton. M., Conduction in Polar Crystals I Electrolytic Conduction in Solid Salts, *Trans. Faraday Soc*., 1938, **34**, 485–499

[22] Grau-Crespo. R., Al-Baitai. A., Saadoune. I., De Leeuw. N., Vacancy ordering and electronic structure of γ-Fe_2O_3 (maghemite): a theoretical investigation, *J. Phys. Condens. Matter*., 2010, **22**, 1–7

[23] Wang. G., Chen. H., Wu. G., Kuang. A., Yuan. H., Hybrid Density Functional Study on Mono- and Codoped $NaNbO_3$ for Visible-Light Photocatalysis, *Chem. Phys. Chem*., 2016, **17**, 489–499

[24] Jalem. R., Rushton. M., Manalastas. W., Nakayama. M., Kasuga. T., Kilner. J., Grimes. R., Effects of gallium doping in garnet-type $Li_7La_3Zr_2O_{12}$ solid electrolytes, *Chem. Mater*., 2015, **27**, 2821–2831

[25] Volnianska. O., Boguslawski. P., GGA + U study of native point defects in $ZnRh_2O_4$, *J. Phys. D. Appl. Phys.*, 2014, **47**, 1–10

[26] Gryaznov. D., Blokhin. E., Sorokine. A., Kotomin. E., Evarestov. R., Bussmann-Holder. A., Maier. J., A comparative Ab initio thermodynamic study of oxygen vacancies in ZnO and $SrTiO_3$: Emphasis on phonon contribution, *J. Phys. Chem. C.*, 2013, **117**, 13776–13784

[27] Wan. L., Beckman. S., Substitutional C on B sites in $AlLiB_{14}$, *J. Phys. Condens. Matter*., 2013, **25**, 1–5

[28] Broderick N. ,November 2002: Lithium Niobate [Internet]. Nature. 2002 [cited 2016 Oct 26]. p. 1. Available from: http://www.nature.com/materials/news/features/021107/portal/m021031-6.html

[29] Kong. Y., Liu. S., Zhao. Y., Liu. H., Chen. S., Xu. J., Highly optical damage resistant crystal: Zirconium-oxide-doped lithium niobate, *Appl. Phys. Lett*., 2007, **91**, 1-3

[30] Koyama. C., Nozawa. J., Maeda. K., Fujiwara. K., Uda. S, Investigation of defect structure of impurity-doped lithium niobate by combining thermodynamic constraints with lattice constant variations, *J. Appl. Phys*., 2015, **117**, 1-7

[31] Lengyel. K., Kovács. L., Mandula. G., Rupp. R., Kinetics of OH- ions in nearly stoichiometric $LiNbO_3$ crystals, *Ferroelectrics*, 2001, **257**, 255–262

[32] Cantelar. E., Sanz-Garcia. J., Cusso. F., Growth of $LiNbO_3$ co-doped with Er^{3+}/Yb^{3+}, *J. Cryst. Growth*, 1999, **205**, 196–201

[33] Stroganova. E., Nalbantov. N., Galutsky. V., Yakovenko. N., A study of the quantum efficiency of multichannel relaxation in $LiNbO_3$:Yb, Er crystals, *Opt. Spectrosc.*, 2016, **121**(6), 856–861

[34] Zhang. P., Chen. Z., Hang. Y., Li. Z., Yin. H., Zhu. S., Fu. S., Li. A., Enhanced 2.7 μm mid-infrared emissions of Er^{3+} via Pr^{3+} deactivation and Yb^{3+} sensitization in $LiNbO_3$ crystal, *Opt. Express*, 2016, **24**(22), 25202–25210

[35] Demirkhanyan. H., Investigation of spectroscopic properties of $LiNbO_3$: Ho^{3+} crystals, *J. Phys. Conf. Ser.*, 2016, **672**, 1-4

[36] Dai. L., Tan. C., Yan. Z., Xu. Y., Influence of [Li]/[Nb] ratios (0.85, 0.94, 1.05, 1.20 and 1.38) on dopant occupancy and light-induced scattering of Hf:Yb:Ho:$LiNbO_3$, *J. Alloys. Compd.*, 2016, **683**, 108–13

[37] Dai. L., Jiao. S., Yan. Z., Dai. P., Lui. G., Xu. Y., Influence of magnesium concentration on the optical properties of ytterbium and holmium co-doped lithium niobate crystal, *Mod. Phys. Lett. B*., 2016, **30**(1), 1-8

[38] Dai. L., Zhou. Z., Xu. C., Xu. Y., Li. D., Chen. C., The effect of In^{3+} doping on the optical characteristics of Ho:$LiNbO_3$ crystals, *J. Mol. Struct*., 2013, **1047**, 262–266

[39] Du. W., Zhang. P., Zhang. Z., Ren. S., Wong. W., Yu. D., Pun. E., Zhang. D., Electro-optic coefficients r_{13} and r_{33} of singly Er^{3+}-doped and In^{3+}/Er^{3+}-codoped $LiNbO_3$ crystals, *J. Phys. Chem. Solids*, 2017, **100**, 101–106

[40] Dalton Research Group, *Intro to Electro-Optics* [Presentation], University of Washington, March 2005

[41] Moretti. P., Canut. B., Ramos. S., Brenier. R., Thevenard. P., Poker. D., Da Cunha. J., Amaral. L., Vasquez. A., Characterization of europium implanted $LiNbO_3$, *J. Mater. Res*., 1993, **8**(10), 2679–2685

[42] Pankratov. V., Grigorjeva. L., Millers. D., Corradi. G., Polgàr. K., Luminescence of ferroelectric crystals: $LiNbO_3$ and $KNbO_3$, *Ferroelectrics*, 2000, **239**, 241–250

[43] Sun. L., Guo. F., Lv. Q., Li. H., Cai. W., Xu. Y., Zhao. L., Defect structure and photorefractive properties of In:Eu:Fe:$LiNbO_3$ Crystals with various Li/Nb ratios, *J. Cryst. Growth*, 2007, **307**, 421–426

[44] Qian. Y., Zhang. H., Wang. R., Wu. Q., Energy conversion in Er/Eu:$LiNbO_3$ for enhanced near-infrared and ultra-violet light harvesting, *Mater. Lett*., 2015, **160**, 555–557

[45] Takahashi. M., Iyoda. K., Maeda. Y., Miyauchi. T., Ohkido. S., Wakita. K., Kajitani. N., Kurachi. M., Hotta. K., Preparation and characterization of Eu: Ti codoped $LiNbO_3$ films prepared by the sol-gel method, *J. Appl. Phys.*, 2009, **106**, 1-7

[46] Gebre. T., Batra. A., Guggilla. P., Aggarwal. M., Lal. R., Pyroelectric Properties of Pure and Doped Lithium Niobate Crystals for Infrared Sensors, *Ferroelectr. Lett*., 2004, **31**, 131–139

[47] Zhang. T., Wang. X., Geng. T., Tong. C., Kang. C., Enhanced photorefractive properties in Hf, Ce and Cu co-doped $LiNbO_3$ crystals for holographic application, *J. Alloys. Compd.*, 2015, **629**, 255–259

[48] Liu. X., Nonvolatile hologram storage properties of tri-doped Zn : Ce : Cu : $LiNbO_3$ crystals, *Optik*, 2014, **125**, 4903–4905

[49] Sun. T., Dai. L., Xu. C., Qian. Z., Li. D., Lin. J., Wang. R., Xu. Y., Enhancement of nonvolatile holographic storage properties in In:Ce:Mn:$LiNbO_3$ crystal by [Li]/[Nb] ratios, *J. Mol. Struct.*, 2013, **1053**, 1–4

[50] Zhou. W., Biao. W., Wei. Y., Ling. F., Ma. D., Yiran. N., Photorefractive properties of Double-doped Hf:Ce:$LiNbO_3$ Crystals, *Microw. Opt. Technol. Lett.*, 2008, **50**(6), 1693–1695

[51] Yang. C., Zhao. Y., Wang. R., Li. M., Studies of photorefractive crystals of double-doped Ce,Fe : $LiNbO_3$, *Opt. Commun*., 2000, **175**, 247–252

[52] Xu. Z., Xu. Y., Growth and optical properties of Mg:Ce:Fe:$LiNbO_3$ crystals, *Mater. Lett.*, 2007, **61**, 3243–3246

[53] Ling. F., Wang. B., Xiang. C., Tao. G., Dong. T., Yuan. W., Sun. N., Effect of UV light on multiplexing holograms in near-stoichiometric $LiNbO_3$:Ce:Fe. ,*Opt. Commun*., 2004, **241**, 293–298

[54] Wang. R., Wang. B., Liu. Y., Shi. L., Double-frequency properties of In:$LiNbO_3$ crystals, *Cryst. Res. Technol*., 2005, **40**, 684–687

[55] Sun. L., Guo. F., Lv Q., Liu L li., Li H tao., Cai W., Zhao. L., Xu. Y., OH-absorption properties of the optical damage region in codoped In/Mg:$LiNbO_3$ crystals with various Li/Nb ratios, *Optik,* 2009, **120**, 514–518

[56] Biao. W., Wang. R., Nie. Y., Xu. Y., Investigation on photorefractive properties of In:Mn:Fe:$LiNbO_3$, *Opt. Mater.*, 2003, **23**, 273–276

[57] Zhen. X., Zhang. X., Zhao. L., Xu. Y., Growth and optical properties of In:Nd:$LiNbO_3$ crystals, *Solid State Commun.*, 2003, **126**(4), 203–206

[58] Zhen. X., Li. Q., Xu. Y., Structure and optical damage resistance in In:Mn:Fe:$LiNbO_3$ crystals, *Mod. Phys. Lett. B*, 2004, **18**(16), 841–846

[59] Xu. C., Leng. X., Xu. L., Wen. A., Xu. Y., Enhanced nonvolatile holographic properties in Zn, Ru and Fe co-doped $LiNbO_3$ crystals, *Opt. Commun.*, 2012, **285**, 3868–3871

[60] Zhen. X., Li. Q., Li. H., Liu. Z., Xu. Y., Zhao. L., Spectroscopic characterizations and optical damage resistance of Zn:Yb:Er:$LiNbO_3$ crystals, *J. Lumin*., 2005, **114**, 288–92

[61] Zhen. X., Li. H., Sun. Z., Ye. S., Zhao. L., Xu. Y., Holographic properties of double-doped Zn:Fe:$LiNbO_3$ crystals, *Mater. Lett.*, 2004, **58**(6), 1000–1002

[62] Zhen. X., Li. H., Zhao. L., Xu. Y., Structure and optical damage resistance of Zn:Er:$LiNbO_3$ waveguides, *Mater. Sci. Eng. B.*, 2003, **103**, 135–139

[63] Yu. X., Rong. X., Leng. X., Lifetime of thermally fixed holograms and gratings in Zn:Fe:$LiNbO_3$ crystals., *Optik*, 2015, **126**, 784–787

[64] Meng. Q., Luo. S., Sun. X., Zhou. Z., Forced oscillator model of dynamic spatial charge field in the reduced Zn:Fe:$LiNbO_3$ crystal, *Optik*, 2014, **125**, 4799–4802

[65] Zhen. X., Li. Q., Xu. Y., Structure and optical damage resistance of Zn:Mn:Fe:$LiNbO_3$ crystals., *Optik*, 2005, **116**, 149–152

[66] Zhen. X., Wang. R., Li. M., Zhao. L., Xu. Y. ,Optical damage resistance in Zn:Nd:$LiNbO_3$ laser crystals, *Mater. Chem. Phys*., 2003, **80**, 11–14

[67] Shannon R., Revised effective ionic radii and systematic studies of interatomic distances in halides and chalcogenides, *Acta. Crystallogr. Sect. A*, 1976, **32**(5), 751–767

[68] Koyama. C., Nozawa. J., Fujiwara. K., Uda. S., Effect of point defects on Curie temperature of lithium niobate, *J. Am. Ceram. Soc*., 2017, **100**(3), 1118–1124

[69] Sanna. S., Schmidt. W., Ferroelectric Phase Transition in $LiNbO_3$:Insights From Molecular Dynamics, 2012, **59**(9), 1925–1928

[70] Catlow. R., Solids:Computer Modeling, *Encycl. Inorg. Chem*., 2006, 1–17